Title

On the thermodynamic efficiency of a multiferroic thermomagnetic generator: From bulk to atomic scale

Author

Sandoval, Samuel M.

Publication Date

2014

University of California
Los Angeles

On the thermodynamic efficiency of a multiferroic thermomagnetic generator: From bulk to atomic scale

A dissertation submitted in partial satisfaction
of the requirements for the degree
Doctor of Philosophy in Mechanical Engineering

by

Samuel Mancilla Sandoval

2014

Abstract of the Dissertation

On the thermodynamic efficiency of a multiferroic thermomagnetic generator: From bulk to atomic scale

by

Samuel Mancilla Sandoval
Doctor of Philosophy in Mechanical Engineering
University of California, Los Angeles, 2014
Professor Gregory P. Carman, Chair

A unique multiferroic type of thermomagnetic generator is being investigated in order to establish its thermodynamic efficiency at different size scales. This device generates electricity when a magnetic material interacts with a thermal gradient by means of a spring-magnet mechanism. This unique technology is compared to other thermal-electric energy harvesting technologies to show that these devices have a similar goal of achieving a maximum theoretical efficiency of around 50% relative to Carnot. The first approach towards achieving improved performance relies on the analytical modeling, and experimental verification, of several subsystems stemming from the original design, which include the optimization of the magnetic force component, the optimization of the heat transfer process and the efficiency of the energy conversion process. The method to improve the magnetic force component is not recommended and neither is the method to improve the heat transfer process. Nevertheless, the energy conversion subsystem is successfully modeled and verified; thereby suggesting that an electromagnetic induction coil may be better suited for the energy conversion process over a ferroelectric transduction mechanism at bulk scale. A cascade design is also investigated as a method to improve device efficiency; though analysis reveals a design flaw, which leads to other methods for improving efficiency.

Two models of thermomagnetic generator thermodynamic efficiency are developed, which are based on distinct approaches taken by Solomon and Brillouin in order to compare this unique system to a Carnot engine. The model based on a modified form of Solomon's approach results in a relative efficiency of 0.5%, which compares well with an estimate of efficiency based on provided data from the original design. This representative model of efficiency was then applied to a survey of pure elements for comparison, which confirms gadolinium as the best material for use as a working body with a relative efficiency of around 20% . The model based on Brillouin's approach represents a more rigorous thermodynamic analysis, which qualitatively agrees with the results based on Solomon's approach, though it predicts larger values of efficiency for most of the materials in the survey. The conservative model based on Solomon's approach is then applied to a hypothetical system that uses a single-domain magnetic material as a working body. This effort is pursued since single-domain nanostructures exhibit a remanent magnetization, which is shown to increase magnetic energy density. The resulting analysis predicts efficiencies on the order of 30% relative to Carnot for this nanoscale system, though the effects of size are not considered in this model.

A model is developed to correlate the effects of size on thermodynamic efficiency for this device. Considering a nanoscaled nickel structure as a working body, this model combines three existing models to predict relative efficiency values that are comparable to the bulk scale, although this system may operate closer to room-temperature. This result is unexpected since the absolute efficiency is shown to increase as a function of decreasing size, though this discrepancy is explained as a consequence of Curie point suppression. The combined model is also applied to a hypothetical composite made of separated layers of nickel with distinct thicknesses. This composite material is predicted to spread the ferromagnetic transition across a much larger temperature range as compared to bulk nickel, such that this material may be better suited for different applications; for example, as a sensor or as a thermal switch. Moreover, this combined model is also shown to be a lower-bound estimate of thermodynamic efficiency, since the actual performance depends on material characterizations that have yet to be determined.

The magnetization of ferromagnetic nanostructures as a function of both applied field, and temperature represents a current engineering challenge. This may be due to current manufacturing techniques that produce defects, and may also be due to resolution limitations of commercially available magnetometers. These challenges also affect a proposed hypothesis regarding the existence of a distribution of transition temperatures within a single nanostructure. This hypothesis aims to resolve whether the diffuse transition behavior of ferromagnetic nanostructures is due to volume-averaged magnetometer measurement techniques, and/or due to surface effects from defects resulting from imperfect manufacturing techniques. These issues would need to be resolved before considering a nanoscale design, which may potentially be useful as a secondary energy recycling device in thermally-assisted magnetic recording applications. Nevertheless, a proof-of-concept experimental setup is offered that may be useful for future designs at the smallest relevant scales.

The dissertation of Samuel Mancilla Sandoval is approved.

Chistopher S. Lynch

Adrienne S. Lavine

Bruce S. Dunn

Gregory P. Carman, Committee Chair

University of California, Los Angeles
2014

Dedico esta tesis a mis maravillosos padres Marcia y Narciso,
mi bella esposa Dayna y nuestra querida Foxy,
mis increíbles hermanos Sandra, Monica y Ernesto,
y a todos mis amigos.

Table of Contents

List of Figures

List of Tables

ACKNOWLEDGMENTS

I am grateful to my adviser Professor Greg Carman for persevering with me throughout this formative experience. I also thank Professors Adrienne Lavine, Chris Lynch and Bruce Dunn for their support, insight and feedback as members of my dissertation committee.

I acknowledge Ray Hsu, Kyle Wetzlar, Gavin Chang, Youngjae Chun, Ashly Ainley, Jon Salfity, David Herman, Josh Hosking, and the Active Materials Laboratory as well as Katie Bulgrin, Gilhwan Cha, and Professors Sungtaek Ju and Abdon Sepulveda for their influence and contributions to this dissertation. I also acknowledge the researchers whose efforts form the basis of key concepts in this dissertation, they are: M. Ujihara, D. Solomon, L. Brillouin, C. Sun and C. Kittel.

I especially thank Scott Keller for his insights, perspective, enlightening advice and encouragement during some crucial moments. I also especially thank Miguel Lozano for his perspective, humor, and support during other crucial moments.

I appreciate Rick Ainsworth, Sherry Hermozi, Audrey O'Neal and everyone from the Center for Excellence in Engineering and Diversity Office for their support and encouragement throughout my campus experience. I also appreciate Angie Castillo, Abel Lebon and the entire administrative staff in the Mechanical and Aerospace Engineering Department for their friendliness, support and efforts made on my behalf.

I owe a debt of gratitude to the Sandoval family for the many sacrifices they made on my behalf. This dissertation could not have been made possible without their love, support and encouragement at every step of the way. Finally, I thank all of my friends, including Andy Guerrero, Wally Dueñas, Javi Castro and Eric Melero for their support and encouragement throughout this experience.

Vita

2001	Sylmar High School – Math, Science, & Technology Magnet, Sylmar, California.
2007	B.S. (Mechanical Engineering), University of California, Los Angeles, California.
2007–Present	Graduate Research Assistant, Mechanical and Aerospace Engineering Department, University of California, Los Angeles, California.
2007–Present	Instructor and Lecturer, Center for Excellence in Engineering and Diversity, University of California, Los Angeles, California.
2009–2012	Teaching Assistant, Mechanical and Aerospace Department, University of California, Los Angeles, California.
2013	M.S. (Mechanical Engineering), University of California, Los Angeles, California.

Publications and Presentations

Sandoval, S. M. & Carman, G. P. “Thermomagnetic energy conversion efficiency near the transition point for nickel atomic layers.” *58th Annual Conference on Magnetism and Magnetic Materials*, Denver, Colorado, USA (2014)

Hsu, C.J., Sandoval, S. M., Wetzlar, K. P. & Carman, G. P. “Thermomagnetic conversion efficiencies for ferromagnetic materials.” *Journal of Applied Physics*

110(12), 123923, (2011).

Hsu, C.J., Sandoval, S. M., Wetzlar, K. P. & Carman, G. P. "Energy conversion efficiency analysis using thermomagnetic properties of ferromagnetic materials." *56th Annual Conference on Magnetism and Magnetic Materials*, Scottsdale, Arizona, USA (2011)

Sandoval, S. M., Hsu, C.J., & Carman, G. P. "An Efficiency Analysis of a Novel Thermal Energy Harvesting Device." *SPIE Smart Structures/NDE 2010*, San Diego, California, USA (2010)

Cha, G., Bulgrin, K., Sandoval, S. M., Chang, G., Schulenberg, C., Ju, S. & Carman, G. P. "Thermoelectric energy harvesting by thermal-magnetic switching of ferromagnetic materials." *SPIE Smart Structures/NDE 2009*, San Diego, California, USA (2009)

Ainley, A., Salfity, J., Herman, D., Hosking, J., Sandoval, S. M., & Carman, G. P. "Gadolinium thermal energy harvester." *Engineering 87*, Henri Samueli School of Engineering and Applied Sciences, University of California, Los Angeles, California, USA (2008)

CHAPTER 1

Introduction

The objective of this investigation is to develop a fundamental understanding of thermodynamic efficiency for a unique thermal energy harvesting device across multiple scales. The unique multiferroic device of interest may be classified as a micro-electro-mechanical system (MEMS), which is capable of converting thermal energy into electrical energy. This device was invented in 2007 by Ujihara *et.al.*, and was called a thermal energy harvesting device (TEHD) that makes use of ferromagnetic materials [UCL07]. In this investigation, we model this device as a type of thermomagnetic generator (TMG) [SHC10, HSW11b, HSW11a] [ASH08, SSC14, CBS09, SC14], and hereafter refer to it as a multiferroic thermomagnetic generator (MTMG), which is shown in Figure 1.1.

This MTMG is designed to operate around room temperatures in order to convert waste-heat, *i.e.* from the environment or as a byproduct of heat-intensive industrial processes, into usable electrical energy. Such a design could potentially power a network of sensors for a variety of applications involving a thermal potential, including the following examples: structural health monitoring, petroleum transportation, and the detection of a hazardous environment. In general, any thermal energy harvesting device involving waste-heat recovery will be limited to very small absolute efficiencies, *i.e.* less than 10% [Lee12] [LGM12] [NVB10] [VKG12a] [VKG12b] [FST11]. Furthermore, these applications would constrain the size of the power supply to approximately the size of the sensor itself, which is ever decreasing towards the atomic scale. We aim to maximize

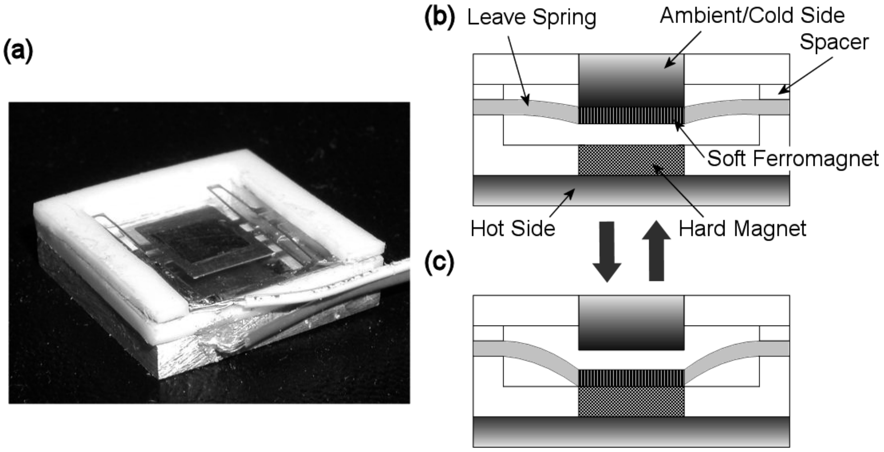

Figure 1.1: Multiferroic thermomagnetic generator (MTMG) with restoring spring mechanism (Images borrowed from Ujihara et al., 2007 [UCL07]); (a) Actual device, (b) cross-section during cooling, (c) cross-section during heating.

thermal energy conversion efficiency in order to recover as much electrical energy from both the limited thermal energy source and the limited scale. We hypothesize that nanoscale magnetic phenomena may dramatically increase the efficiency of a MTMG, which represents a clean energy technology. Moreover, the atomic-scale investigation of efficiency for this device may be considered as analogous to a fundamental biological concept present in nature, *e.g.* the human body makes efficient use of its resources by using distributed nano-scale processes [ACL06] [Car11].

In the human body, the basic source of energy comes from an adenosine-triphosphate (ATP) molecule, which is synthesized by an ATP enzyme [DSF06] [DZB04] [JHF01] [KK09] [LSL05] [NBA08] [OW99] [PR99] [SNW02] [SLW99] [WO98] [YMH01], and schematically shown in Figure 1.2 (left). This biological example of interest, which serves as a strictly qualitative comparison in this investigation, occurs when a human cell breaks down food molecules such that the resulting ions spread unevenly throughout the cell boundary. This proton gradient is analogous to a temperature gradient in a MTMG, and represents the input energy that drives the conversion into useful energy. The force generated by the proton gradient drives ions into the base of the ATP enzyme, which causes the head of the ATP structure to rotate, and thereby rearrange an adenosine-diphospahte (ADP) molecule into an ATP molecule [KK09] [LSL05] [NBA08] [SNW02] [SLW99]. This cyclic displacement of protons is analogous to the linear displacement of the ferromagnetic working body in a MTMG due to a magnetic instability, *i.e* a 2^{nd} order phase transition between ferromagnetic and paramagnetic phases, caused by oscillatory interaction with a thermal gradient. One MTMG cycle will then produce a useful flow of electrical charge carriers, which is qualitatively similar to the production of a useful energy packet by an ATP enzyme. Furthermore, the production of ATP has been observed to operate close to 100% efficiency [KYN00] [NBA08] [YMH01]. Thus, we aspire to qualitatively replicate the outstanding efficiency of an ATP enzyme for a MTMG at a similar scale.

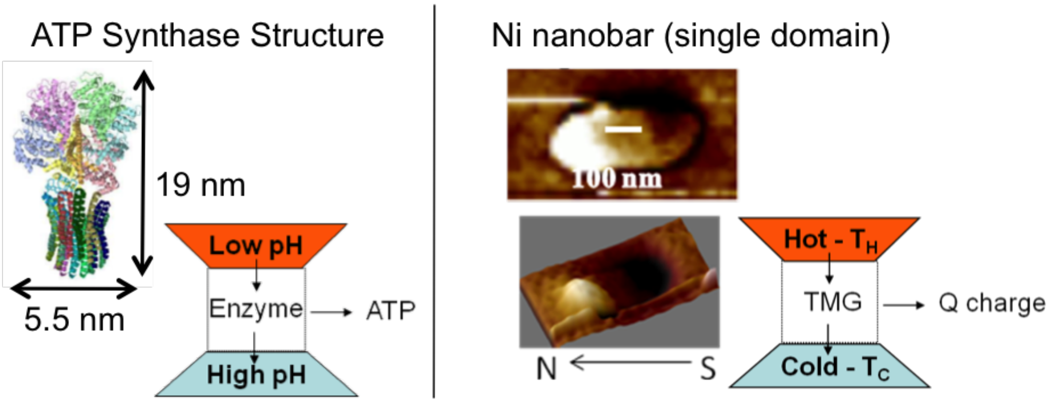

Figure 1.2: Illustration of a ATP synthase (Image borrowed from Stock et al., 1999 [SLW99]) to harvest energy (left) compared with our fundamental study element (Images borrowed from T. Chung et al., 2009 [CKC09]) Ni nanobar (i.e. 150nm x 30 nm x 50nm) as a potential working body in thermomagnetic generator system (right); note that the size scale is similar, and that both involve a transfer mechanism

The thermodynamic efficiency of the original MTMG design was not reported, and was subsequently established by Sandoval *et.al* in 2010 [SHC10, HSW11b, HSW11a]. This analysis revealed that the efficiency of the original MTMG was small, *i.e.* on the order of 0.01%, since it was designed for maximum power performance, *i.e* on the order of 1 mW/cm^2. Nonetheless, previous analytical work suggests that TMG conversion efficiency may be as much as 55% relative to a Carnot engine operating under the same temperature gradient [BI48] [Ell59]. We hypothesize that a nanoscaled version of this MTMG (nanoMTMG) may achieve efficiencies closer to this upper bound when compared to its bulk counterpart. This hypothesis is based on recent research into Ni single domains (SD) [BWH11] [BCH13] [CKC09] [WBH11], schematically shown in Figure 1.2 (right), where magnetization is confined by geometric boundaries at the nanoscale. The confined magnetization of a SD represents a larger energy density when compared to its multi-domain bulk counterpart, which indicates a larger absolute efficiency.

We aim to account for size-effects at these small scales in order to predict the efficiency of a nanoMTMG relative to the original MTMG design. To this end, in Chapter 2 we review some of the existing thermal energy harvesting devices with an emphasis on thermomagnetic generators; specifically, we focus on the MTMG device for which we will continually revisit throughout this investigation. In Chapter 3 we cover some experimental methods aimed at improving the power performance of this MTMG, including contactless generation via electromagnetic induction. In Chapter 4 we review the existing theoretical framework of TMG efficiency and uniquely apply them to a MTMG to establish efficiency for various pure elements acting as a working body at the bulk scale. Subsequently, in Chapter 5 , we consider various ways to establish the efficiency of this MTMG both at the atomic and nano scales; including both magnetic analysis, as well as thermal analysis. These analyses yield different predictions for efficiency, based on different assumptions, and have yet to be tested. In general, however, they agree that the absolute efficiency will benefit from size-effects at the scale of molecules. Finally, other considerations are reported for future research work aimed at making use of this unique MTMG technology in Chapter 6 , before offering concluding remarks in Chapter 7 .

CHAPTER 2

Thermal-Electric Energy Harvesting Review

2.1 Introduction

In this chapter, we review a selection of thermal-electric energy harvesting devices (TEHD), schematically illustrated as a general thermal-engine in Figure 2.1, with relevant background. We start by reviewing Seebeck effect based thermoelectric devices since they represent the standard in thermal-electric energy harvesting devices. We also review other lesser-known TEHDs that are currently active areas of research, which are thermomagnetic generators (TMG) and pyroelectric generators (PEG).

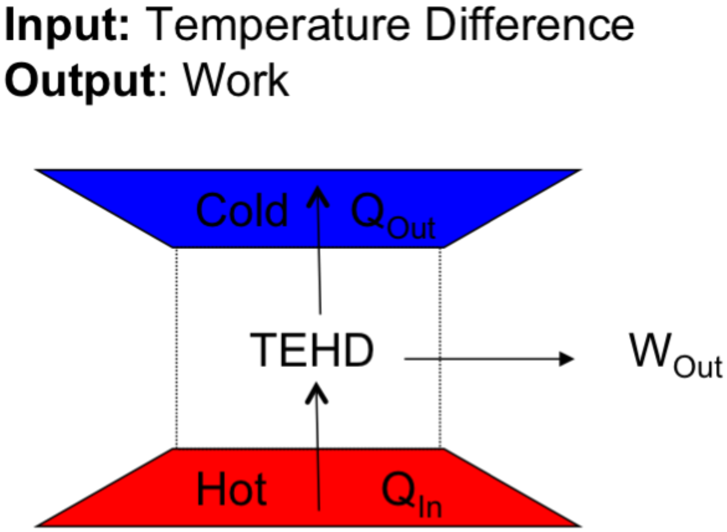

Figure 2.1: Schematic for generic thermal-electric energy harvesting device.

2.2 Thermoelectrics based on the Seebeck effect

The field of Seebeck effect based thermoelectric devices has received considerable attention over the last few decades [AR10] [AOG12] [CBS09] [CDD03] [ELA10] [FDF11] [Gan06] [HBK13] [HTS00] [HTW02] [HWT05] [Her06] [HWC13] [Ju08] [KTH11] [LCZ10] [LW11] [Lut02] [Pet10] [SM09] [SGA09] [SCJ06] [VSC01] [WHC12] [XYL12] [YC04], though the field began as a discovery made nearly two centuries ago. In the 1820's, Dr. Thomas J. Seebeck discovered that a pair of dissimilar metals held at different temperatures produces a voltage [SO95], *i.e.* the transport of an electric charge due to a thermal gradient. This phenomenon is called the Seebeck effect and is the fundamental principle behind Seebeck thermoelectric generators.

The degree to which a material can separate charge due to the influence of an applied thermal gradient is known as the Seebeck coefficient (α). The classic performance parameter used for this type of TEHD is the figure of merit (FOM), ZT, and the relative efficiency, η_{rel}, may be defined as given in equation (2.1) [SCJ06]:

$$\begin{aligned} ZT &= \tfrac{\alpha^2 T}{\rho k} \\ \eta_{rel} &= \left(\tfrac{T_{hot}-T_{cold}}{T_{hot}}\right) \cdot \left(\tfrac{\sqrt{ZT+1}-1}{\sqrt{ZT+1}+T_{cold}/T_{hot}}\right) \end{aligned} \tag{2.1}$$

Where ρ, k and T are the electrical resistivity, thermal conductivity and mean temperature, respectively. We observe that η_{rel} is directly related to ZT, *i.e.* the FOM [AOG12] [Gor91] [Tel47]. It seems that the thermoelectric communities focus on reporting the FOM, rather than on η_{rel}. Either definition may be applied and the relation in equation (2.1) is plotted in Figure 2.2 for cross-reference between either measures.

In 1922, the first application for a Seebeck device was to power a radio receiver by placing a bimetallic strip inside a fire lamp [Tel47]. In general, metals have a large thermal conductivity and a small Seebeck coefficient, producing a small

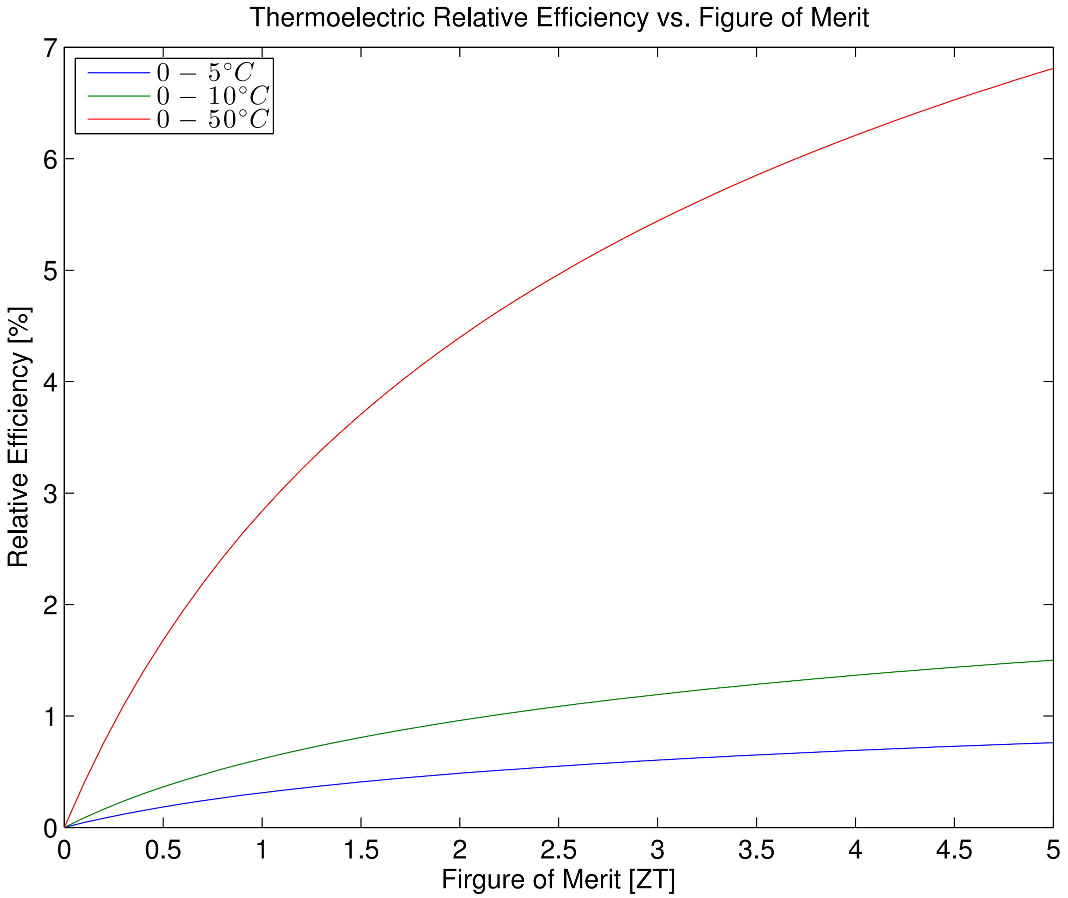

Figure 2.2: Thermoelectric device relative efficiency as a function of figure of merit for various operating temperatures.

figure of merit, *i.e.* $ZT \ll 1$, which is a very small relative efficiency [Tel47]. This marginal power output halted the pursuit of thermoelectric energy harvesting for several decades. In the 1950's [Iof57], new semiconductor materials were discovered, *e.g.* bismuth-telluride alloys (BiTe) [CDD03], which possess a relatively low thermal conductivity that produces a figure of merit close to $ZT = 1$. Although the figure of merit represented a substantial improvement over metal-based thermoelectric generators, a figure of merit of $ZT = 4$ ($\eta_{rel} \approx 40\%$) is required to compete with other energy harvesting approaches (*e.g.* magneto-mechanical generators) [ODD07] [BBR97].

Recent research in developing new super-lattice thermoelectric materials predict improved efficiency [CDD03] [HTS00] [HTW02] [HWT05]. A super-lattice structure is essentially an alternating stack of dissimilar materials that enhance one or more material properties. A thermoelectric super-lattice structure incorporates a layer of non-thermoelectric material, which has a tendency to scatter phonons (*i.e.* low thermal conductivity), while still permitting electric charge transport (*i.e.* low electrical resistivity). Analytical predictions for these super-lattice structures suggest a FOM of $ZT > 4$; however, measured values suggest a FOM that is just over one, which as yet is hardly an improvement over non-super-lattice materials. In fact, studies on phonon conduction in super-lattice structures suggested that the super-lattices may not enhance the thermoelectric process, but may limit their performance [CZ01] [Gan06] [Ju05] [PS04] [ZC01].

The performance of a Seebeck thermoelectric generators seem to be currently limited by bulk material properties. A state-of-the-art Seebeck thermoelectric generator can perform at a relative efficiency of 10% of Carnot, while operating at a temperature difference of $\Delta T = 50°K$. A plot of idealized absolute efficiency versus temperature for a state-of-the-art Seebeck material is shown in Figure 2.3, where the ambient temperature is $300K$. As can be seen from the Figure 2.3, the typical absolute efficiencies for Seebeck devices that operate around room temperature are on the order of $1 - 2\%$. Thermoelectric devices require large temperature gradients to achieve these efficiencies and are thus unsuitable in applications with relatively small gradients. As a result, current thermoelectric generators are not widely used in harvesting ambient thermal energy, although this has been attempted for use as waste-heat recovery for automobiles [ELA10] [KTH11]. Current thermoelectric generators are mostly used in specialized applications, such as in deep-space satellites and in optoelectronic applications.

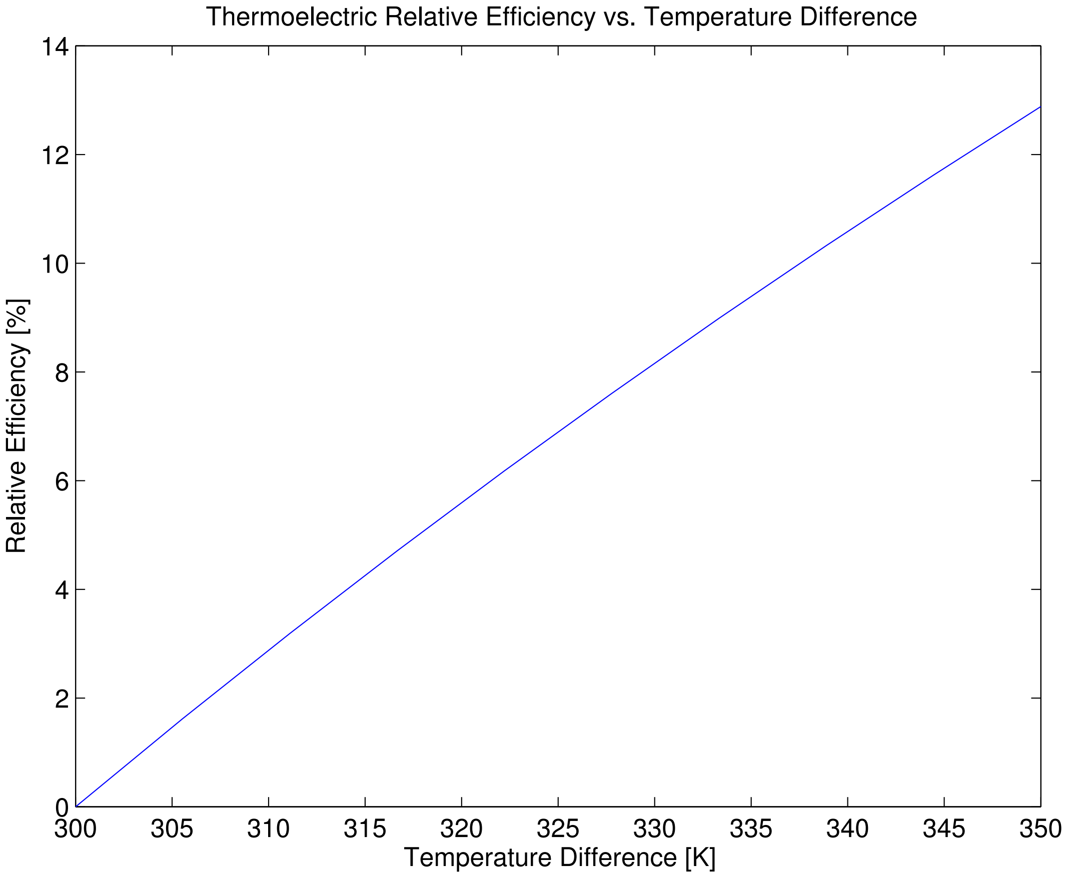

Figure 2.3: Plot of ideal efficiency for a Seebeck effect based thermoelectric device, as a function of operating temperature difference, with cold-side temperature at $T_{cold} = 300K$ and $Z = 1$.

2.3 Thermomagnetic Generators

The extraction of electrical energy from a system that can convert thermal energy into magnetic energy may be called a thermomagnetic generator (TMG) [BI48] [Ell59] [KM84a] [KM84b] [Ros67] [Sol88] [Sol91] [Sta59]. The idea behind a TMG involves a thermally oscillating switch inside a magnetic circuit. The switch is a ferromagnetic material that exhibits a second-order phase transformation, *i.e.* from ferromagnetic to paramagnetic phase, as well as vice versa, about its Curie temperature. The change in induction within an attached magnetic circuit may then generate current in a pick-up coil [Max81]. Before we review the existing literature on this subject however, we clarify some of the terminology used in this investigation.

We start by clarifying our use of the term “multiferroics” to describe a class of devices. The term multiferroics refers to certain active materials, whose physical description may be derived from the term “ferro,” such as ferromagnetism, ferroelectricity, or ferroelasticity [CCB07] [Vop12] [Vop13]. Here, we consider a multiferroic device as a system that incorporates two or more of these “ferroic” type phenomena, such as the ferromagnetic and the ferroelectric phenomena observed in a MTMG type of device (see Section 2.3.3). However, if we consider the same case system and instead change its energy harvesting mechanism to electromagnetic induction, should we then reconsider using the term multiferroic? In this last instance, the new system can be modeled as a combination of thermomagnetic and electromagnetic phenomena. This multiphysics problem involves two applications of a single “ferroic” type of phenomena (*i.e.* ferromagnetism). As such, here we do not describe this type of TMG as a multiferroic device, even though the materials involved may exhibit multiferroic properties under different loading conditions for a different application.

We now turn our attention to the term “thermomagnetic,” which up to this point in the investigation has not been well defined either. We elaborate on this term by first considering the black-box interpretation, shown in Figure 2.1 in section 2.1. Here, we take a system containing only the working body of a fully operational TMG and consider this as our black-box for further interpretation. The “thermal” aspect may be interpreted as the input and the output heat arrows going into and out of the black-box, respectively. This heat causes a change in the “magnetic” aspect of the working body, *i.e.* within the black-box, which then causes the production of electrical energy output via electromagnetic induction. This indirect method of thermal-electric energy harvesting is here referred to as a "thermomagnetic" generator, all of which involve a type magnetic phase transition. Therefore, we first review the relevant physics of a thermally induced 2^{nd}-order ferromagnetic phase transition before reviewing TMGs.

2.3.1 Ferromagnetic Phase Transition

A ferromagnetic material may exhibit a considerably different response to an applied magnetic field at temperatures above and below a critical temperature, known as the Curie point, or the Curie temperature. Above the Curie temperature, the ferromagnetic material behaves like a paramagnet; conversely, ferromagnetic behavior is observed below the Curie point [ACN72] [CG11] [Sta87] [CC78]. This transition occurs without latent heat and is therefore classified as a second-order transformation. A general model that describes all types of magnetism, including the second-order magnetic phase transition, does not currently exist [KGH67]. Nevertheless, the first attempted solutions to the phase transition problem were the phenomenological models of Ising and Landau [CG11] [KM86]. These models may only qualitatively describe experimental observations, *e.g.* the divergence of the heat capacity at the Curie point and do not compare well with experimental measurements across all relevant temperatures in a second-order phase transition [KGH67]. One quantitative model of magnetism stems from an assumption that, in general, thermodynamic properties scale according to a power-law in the vicinity of a second-order phase transformation [KGH67] [Sta87]. This power-law model however, also fails to satisfactorily compare with experimental data across all relevant temperatures. We adopt, and here review, the Langevin-Weiss-Heisenberg model of ferromagnetism, even though it too has similar limitations [CC78] [CG11] [Jil98] [Oh99].

In 1907, Dr. Pierre Weiss hypothesized a molecular field theory of magnetism [Wei07], also called mean-field theory (MFT). This theory describes how a local magnetic force within a material is responsible for the large fields found in ferromagnets with a zero applied-field. This theory is a result of the Curie-Weiss law of paramagnetism [CC78] [CG11], which describes the mass susceptibility, χ_m, as function of temperature and is given in equation (2.2).

$$\chi_m = \frac{C}{(T - \theta)} \tag{2.2}$$

Where C represents the Curie constant and θ the temperature at which the susceptibility diverges; both of these constants are explicitly defined in equations (2.3)-(2.4).

$$C = \frac{\mu_H \sigma_0 (J + 1)}{3 k_B J} \tag{2.3}$$

$$\theta = \frac{\mu_H \gamma \rho \sigma_0 (J + 1)}{3 k_B J} \tag{2.4}$$

Where μ_H represents the maximum atomic moment, σ_o the mass specific spontaneous magnetization at absolute zero temperature (*i.e.* $\sigma_o = M_o/\rho$), J the net atomic angular momentum, k_B the Boltzmann constant, γ the molecular field coefficient and ρ the density of the material. As can be seen from equation (2.3), the Curie constant is defined by material properties; on the other hand, the temperature defined by equation (2.4) must be determined by experimental measurement [Boz93] [CC78]. In ferromagnets for example, this temperature is theoretically identical to the Curie temperature. Furthermore, this temperature then yields information about the molecular field H_M, as shown in equation (2.5).

$$H_M = \gamma \rho \sigma \tag{2.5}$$

In the absence of an applied field, the mass specific spontaneous magnetization σ is only a function of temperature. At absolute zero temperature, the specific magnetization is a maximum (i.e. $\sigma = \sigma_o$); however, at the Curie point the magnetization vanishes (*i.e.* $\sigma = 0$). In between these extreme cases, the behavior of the spontaneous specific magnetization is described using Brillouin's function, given in equation (2.6).

$$\frac{\sigma}{\sigma_0} = \frac{\sigma}{ngJ\mu_B} = \frac{2J+1}{2J}\coth\left(\frac{2J+1}{2J}a^{'}\right) - \frac{1}{2J}\coth\left(\frac{a^{'}}{2J}\right) = B\left(J, a^{'}\right) \quad (2.6)$$

Such that n is the number of atoms per unit volume, $a^{'} = \mu_H H/k_B T$ and $\mu_H = gJ\mu_B$ where g is the Landé factor and μ_B is a Bohr magneton. The Landé factor is a convenient way of distinguishing whether the atomic contribution to magnetism is due to orbital motion, or pure spin, or some combination of both. The Bohr magneton is a fundamental unit that is used to describe the magnetic moment of a hydrogen atom. The Brillouin function describes the general reduced magnetization behavior, as a function of reduced temperature, for a ferromagnetic atom [Boz93] [Dar67] and is shown as a plot in Figure 2.4. This description is not valid if a magnetic field is applied and a few more steps are required to determine the "adjusted" magnetization. To begin this problem, note that the molecular field is assumed to apply at all temperatures and fields. At the Curie point, with zero applied field, the Brillouin function is zero because its argument $a^{'} = 0$. Thus, the slope of the Brillouin function about this point can be computed using a Taylor series expansion, *i.e.* assuming a small value for $a^{'}$, the result of which is shown in equation (2.7).

$$B(J, a') = a'\frac{(J+1)}{3J} \quad (2.7)$$

After some rearranging, this equation reduces to equation (2.8).

$$\frac{\sigma}{\sigma_0} = \left(\frac{kT}{\mu_H \gamma \rho \sigma_0}\right) a' \quad (2.8)$$

Which represents the molecular field line at any temperature and applied field [CG11]; however, this equation is only valid in the ferromagnetic region if it intersects with the curve of equation (2.6).

If a field is applied, *i.e.* the total field equals the sum of the applied field and the molecular field, the same steps from equations (2.7)-(2.8) apply and they yield

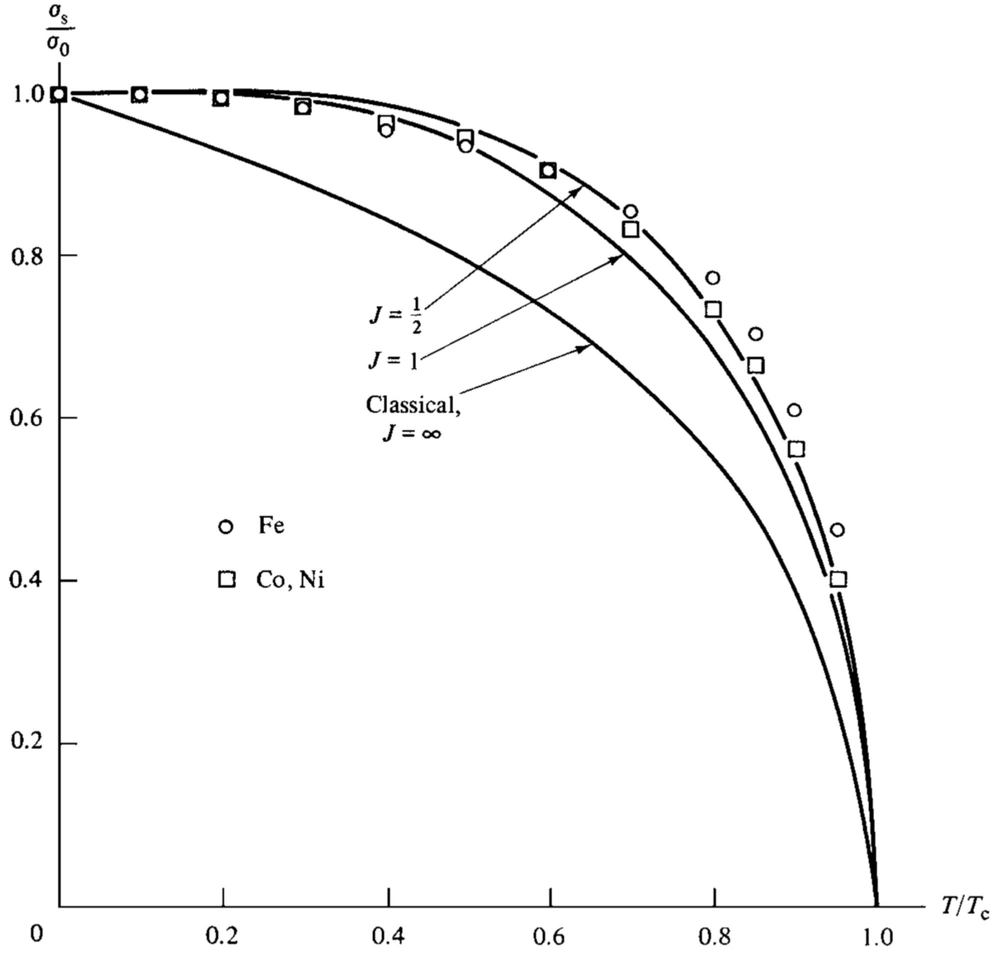

Figure 2.4: Reduced saturation magnetization of iron, nickel and cobalt, as a function of reduced temperature, for various values of net atomic angular momentum (Image borrowed from Cullity *et.al.* 2011 [CG11]).

the result given in equation (2.9).

$$\frac{\sigma}{\sigma_0} = \left(\frac{kT}{\mu_H \gamma \rho \sigma_0}\right) a' - \frac{H}{\gamma \rho \sigma_0} \tag{2.9}$$

Thus, the method of finding the magnetization if the applied field is nonzero is graphical and illustrated in Figure 2.5. The lines 2 and 4 represent molecular field lines (*i.e.* from equation (2.8)) for a ferromagnet below and above its Curie temperature T_c, respectively, with a zero applied field. The intersection of these lines with curve 1 (*i.e.* the Brillouin function) represents the predicted value of reduced magnetization; which for point P is about 90% of its maximum, while zero for line 4 since it is paramagnetic. On the other hand, if a nonzero field is applied, then the lines shift according to the second term in equation (2.9), while retaining their respective slope when compared to the zero-field case. The new intersection points have the following interpretation: point $P^{'}$ is only slightly increased due to its near saturated state, while point B represents a large increase to about 40% of its maximum since its mass susceptibility is relatively large. This process allows the computation of M-H-T curves for a given material based on an average molecular field.

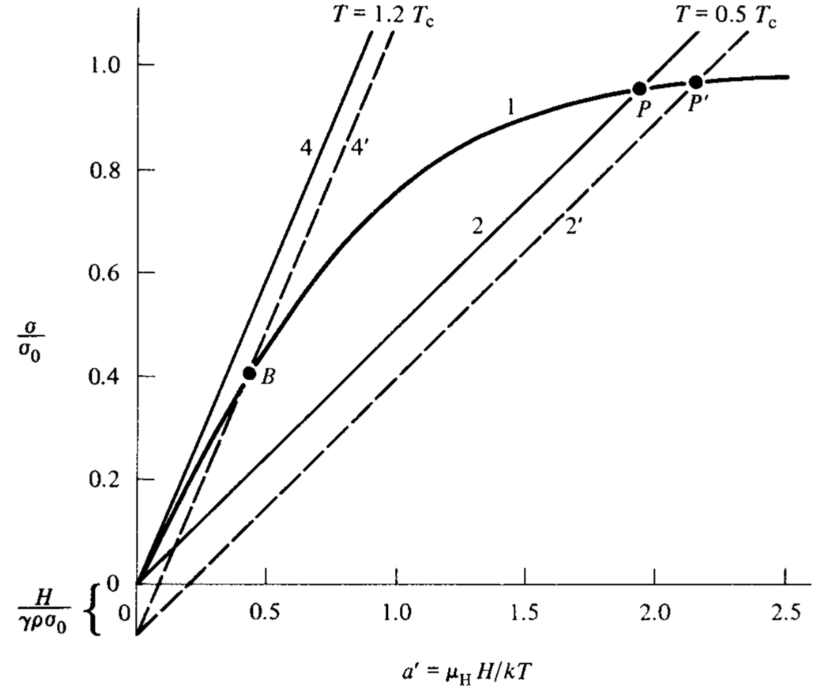

Figure 2.5: Graphical technique for computing reduced magnetization for the case of non-zero applied field (Image borrowed from Cullity *et.al.* 2011 [CG11]); curve 1 represents the case of $J = 1/2$.

The current interpretation of Weiss' molecular field stems from Heisenberg's concept of exchange-interaction energy between neighboring spins, which was introduced in 1928 [Hei28] and defined in equation (2.10).

$$E_{ex} = -2J_{ex}S_iS_j \tag{2.10}$$

Where J_{ex} represents the exchange interaction energy and S_i the spin angular momentum at site i. In other words, this exchange energy is hypothesized to account for Weiss' molecular field. If we assume a pure element contains spins with the same angular momentum S, between z neighbors, then the exchange energy can be computed at site i as given in (2.11).

$$E_{ex} = z\left(-2J_{ex}S^2\right) \tag{2.11}$$

This energy may be assumed to be equivalent to the energy of a spin under an applied field, *i.e.* the molecular field H_M, which is defined in (2.12).

$$E_{pot} = -\mu_H H_m \tag{2.12}$$

Where μ_H represents the atomic magnetic moment of each spin. Equation (2.11) may then be set equal to equation (2.12), in order to produce a relation for the molecular field, which is given in equation (2.13).

$$H_M = \frac{z\left(-2J_{ex}S^2\right)}{\mu_H} \tag{2.13}$$

This result may then be substituted into equation (2.4), while assuming $J = S$ (*i.e.* the condition of pure spin contribution to the atomic moment), to produce a relation given in equation (2.14), which reveals the proportionality between the exchange energy and the Curie temperature of a ferromagnetic material.

$$J_{ex} = \frac{3k\theta}{2zS(S+1)} \tag{2.14}$$

Although the complete equation of state can be calculated, this theory doesn't compare well with experiments in the vicinity of the Curie point [CG11]. For instance, one drawback of this molecular field theory in the bulk state is illustrated in Figure 2.6. In this case, the transition between ferromagnetic, θ_f, and paramagnetic, θ_p, behavior is diffuse, although MFT predicts a sharp drop to zero magnetization. This discrepancy, or "fuzziness," is attributed to spin clusters [CG11]. Examples of spin clusters include domains, domain walls, or any locally coherent interaction among adjacent spins. We may further hypothesize that if these spin clusters are reduced or eliminated, then the drop in magnetization should reach zero at the same point that the paramagnetic behavior is initiated, *i.e.* $\theta_f = \theta_p$. In other words, MFT represents an average local spin description of magnetism and as such, the interaction among spins deters this behavior. Nevertheless, this MFT model does agree well with experimental observations for many magnetic materials at high temperatures and low applied fields [CG11].

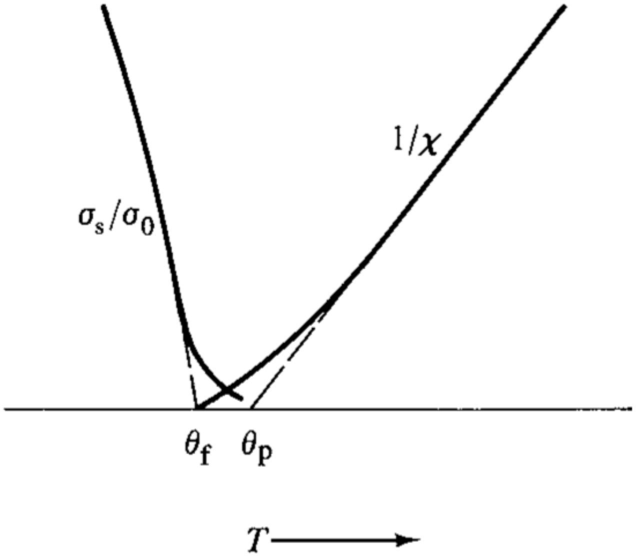

Figure 2.6: Bulk behavior of a ferromagnetic material in the vicinity of its Curie point (Image borrowed from Cullity *et.al.* 2011 [CG11]).

2.3.2 Energy Harvesting based on Electromagnetic Induction

Nikola Tesla postulated the first type of thermomagnetic generator with his 1889 patent [Tes89] of a “Thermo Magnetic Motor,” also known as a Curie motor, or Curie wheel. This system was then given a rigorous thermodynamic treatment by Brillouin *et.al.* in 1949 and yielded a theoretical upper-bound value for relative efficiency of 55% of Carnot for any material [BI48]. At this time, the rare-earth element Gadolinium (Gd) was not thought of as a suitable material for this application due to its rarity. However, the advent of manufacturing techniques capable of isolating Gd opened the opportunity for further investigation into thermomagnetic generation [Ell59], since this material possesses a room-temperature Curie point.

In 1959, Elliott investigated the role of material properties on the performance of a TMG [Ell59]. This work was largely based on the fundamental study by Brillouin; however, the goal of this study was to predict an upper-bound value for power density and absolute efficiency based on material properties. With Gd as the switch and Alnico XII as the permanent magnet, Elliot predicted a maximum power density of 3 Watts per pound of magnetic material at an absolute efficiency of 0.57%, *i.e.* 55% of Carnot efficiency. For comparison, thermoelectric power densities in 1959 were 50 Watts per pound. This study discouraged any more research on TMG for another quarter-century due to the impractical implementation of a high Curie temperature material as a switch, *e.g.* iron, nickel, or cobalt. However, it should be noted that modern hard ferromagnetic materials, *e.g.* NdFeB, have energy densities which are an order of magnitude larger than Alnico XII.

The next significant advancement in TMG theory came in 1984, when Kirol *et. al.* proposed a regenerative cycle [KM84a] [KM84b]. A regenerative cycle reuses the rejected heat from one thermomagnetic generator cycle in order to reduce the amount of heat input for the next cycle and thereby increase total efficiency. This revised fundamental study idealized the regenerative cycle and used numerical analysis techniques in order to predict a maximum relative efficiency of 75% relative to an equivalent Carnot engine. These predictions inspired at least one researcher to design, fabricate and test the first TMG.

In 1991, Solomon designed a thermomagnetic generator with a regenerative cycle [Sol88] [Sol91]. The basic idea of this setup was to oscillate the thermomagnetic switch, both thermally and magnetically, under very large applied-fields. In the place of a permanent magnet, a superconducting solenoid coil was used to produce an arbitrarily large oscillating magnetic field within the switch. If the energy consumed by the solenoid coil is neglected, the system performed with a relative efficiency of 44%. On the other hand, when taking into account the energy required to operate the solenoid, as well as the energy required to maintain superconducting temperatures, the energy output from the system is insufficient to compensate for the input power, *i.e.* a negative-power output. This result did not discourage other researchers from developing innovative ideas that incorporate fundamentals aspects of a TMG, such as realizing Tesla's vision of a Curie motor [ACF13] [ACF14] [Tra10] [Tra11] [FVT13].

2.3.3 Energy Harvesting based on Multiferroics

More recently, a multiferroic approach to thermomagnetic generation (MTMG) was demonstrated in 2007 by Ujihara *et.al* [UCL07]. This type of TMG uses a resetting and dynamic mechanism in order to produce power; which was an idea dating back to the first issued patent on thermomagnetic generation [Tes89] and other similar investigations [ACF13] [ACF14] [CCC14] [FBS14] [FVT13] [HSW11b] [HSW11a] [SHC10] [ASH08] [SC14]. We justify the name MTMG for this device in Chapter 4, which thoroughly considers thermodynamic efficiency.

In this design, a spring-force mechanism shuttles a soft ferromagnetic switch, *i.e.* gadolinium (Gd), between a hot and a cold reservoir. Additionally, the magnetostatic force of attraction between the switch in its ferromagnetic-state, *i.e.* its cold-state, and a hot-side hard ferromagnet causes a spring displacement. A ferroelectric material is incorporated onto the spring mechanism for mechanical transduction in both phases of shuttling. During the next phase of operation, the thermal contact between Gd and the ferromagnet causes a phase transition within the working body, such that the magnetostatic force of attraction is reduced enough to allow a restorative spring displacement. These two phases make up one complete cycle. This design initiated a research and development trend in multiferroic thermal energy harvesting [ASH08] [CCC14] [CST13] [CTC12] [DWZ14] [He12] [JP13] [LBF13] [WBF13] [WSX11]; some of which included working bodies that exhibit a first-order phase transformation, though these materials will not be considered in this investigation.

A lower-bound estimate of power density output for this MTMG, while operating in a vacuum, is $3.61mW/cm^2$ at a frequency of $27Hz$ through an operating temperature range of $273-323K$. The device dimensions measure (2x2cm)x6mm, while the working body dimensions measure 6x6x2mm. A thermodynamic efficiency analysis was not reported in the seminal paper; however, we treat this problem in Chapter 4 and here we report the relative efficiency of the working body as approximately 0.20%. This represents an order of magnitude smaller relative efficiency when compared to Seebeck effect based thermoelectric devices; however, this design was not optimized for efficiency. We may hypothesize an optimized version of this design to yield as much as $100mW/cm^2$, corresponding to a maximum relative efficiency of 5.38%, under the same assumptions. Moreover, this device is limited by the mechanical transduction efficiency of the ferroelectric material, which remains outside of the scope of this investigation.

2.4 Pyroelectric Generators

The final type of TEHD device considered in this chapter is known as a pyroelectric generator (PEG). As the name may imply, a thermal gradient causes a working body to change states; thereby allowing the production of electricity [FFP10] [GSP09] [HLB11] [KNP11] [KPS09] [LGM12] [LJL13] [LPH13] [MXL11] [MP13] [NVB10] [NNP10] [PT14] [RHK11] [SLG08] [SGA09] [Xie09]. This type of device exhibits both similarities and differences between the previous generators so far mentioned.

First, the input thermal energy into a pyroelectric generator causes a phase change, *i.e.* just as in a thermomagnetic generator. However, PEG materials have ferroelectric properties [KNP11] [KPS09] [LGM12] [LJL13] [NNP10]. As such, this phase change is a first-order phase transformation; which means a structural change occurs within the working body and implies a cost latent heat of transformation energy [LGM12] [LJL13] [SH99][VCV14]. We elaborate on this point by emphasizing that in one state, the pyroelectric material is in an ordered state (*i.e.* as in a ferromagnetic state for TMG), which is contrasted by a second state described as disordered (*i.e.* as in paramagnetism for a TMG). In a ferroelectric material, the arrangement of crystallographic dipoles along one direction may be used to define an ordered state, such that the material is considered disordered if this arrangement is disrupted by thermal agitation. Therefore, one PEG cycle experiences two opposing phase transformations, each with distinct latent heats of transformation due to hysteresis. We point out that the hysteresis of a second-order phase transformation is zero by definition.

Second, a PEG may operate as a direct converter of thermal to electric energy, *i.e.* like a Seebeck effect based thermoelectric generator. However, unlike a typical thermoelectric device, a PEG is not a solid-state device since it employs heat exchangers to maintain a thermal gradient, which is also true for most TMG.

The research and development of PEG devices has seen improvements in the last decade [GSL09] [MP13] [PT14] [RHK11] [SLG08] and they are predicted to attain a maximum relative efficiency of 50% [SGA09].

2.5 Summary

A literature survey on three distinct types of TEHDs were introduced, reviewed and finally compared against each other. First, a Seebeck-effect based thermoelectric generator technology was introduced as the most common and commercially successful of all TEHDs. The class of materials for this application exhibit low electrical resistivity and low thermal conductivity in order to directly generate a potential across a thermal gradient. Second, a thermomagnetic generator was introduced as a device that makes use of a second-order phase transition in ferromagnetic materials to indirectly generate a potential: (1) via electromagnetic induction and (2) via ferroelectric transduction. The Langevin-Weiss-Heisenberg model of second-order phase transition was reviewed before focusing on the primary device of interest throughout this investigation; namely, a multiferroic thermomagnetic generator. Lastly, a class of TEHD known as a pyroelectric generator, which makes use of the first-order phase transformation in ferroelectric materials, was introduced as a cycle capable of generating a potential via direct manipulation of ions lined along a prescribed axis. All three of these TEHDs accept thermal energy and produce useful electrical energy and they all appear to predict a maximum relative efficiency that is on the order of 50% of Carnot.

CHAPTER 3

Experimental Approach to Improve Performance

3.1 Introduction

In this chapter, we focus on experiments aimed at improving the output power performance of a unique MTMG [UCL07], *i.e.* an innovative thermal-electric energy harvesting system (see section 2.3.3 for more details), in order to produce electrical power densities greater than $10mW/cm^2$. We consider three main limitations to the power production of this device (*i.e.* currently $3mW/cm^2$), they are: (1) the impedance matching between the spring and magnetic force, (2) the thermal heat transfer limitation on operational frequency, as well as (3) the limiting ferroelectric transduction efficiency. We cover a limited number of experiments and/or simulations that aim to investigate and improve on these limitations. In particular, we cover experiments relating to: (1) optimization of magnetic design, (2) interfacial thermal heat transfer and (3) alternate designs that do not require ferroelectric transduction.

To improve the power output, we first consider the frequency response of the case-study MTMG. To increase the dynamic response, we focused on the thermal conduction at the contact locations, *i.e.* between the soft ferromagnetic material and a heat source. Based on fundamental calculations [CMY69] [Mik74] [MYM04], a conservative estimate of a 10x improvement may be achievable by modifying the thermal interface. This would produce power outputs on the order of $15-30mW/cm^2$, which represents at least one order of magnitude larger power density than what was originally reported. Secondly, to further increase the power production capabilities, an optimization of the magnetic energy component should be considered. We cover simulation models that reveal the sensitivity of the force output as a function of geometry. This is due to the fact that the original device waw fabricated without analytical considerations aimed at optimizing the force of attraction between the applied magnetic field and the device geometry. This optimization may then potentially produce power outputs approaching $100mW/cm^2$. Finally, we consider substituting the ferroelectric transduction component with an electromagnetic induction method in order to avoid potentially heavy energy conversion losses. We review the details of these potential improvements to the original MTMG design, before reporting details of the corresponding experiments.

3.2 Magnetic Energy

This section focuses on increasing the magnetic force component of a MTMG by simulation and experimental verification [CBS09]. The magnetic energy is a function of device geometry as well as the geometry of the ferromagnetic working body [Boz93] [CC78] [CG11]. We implemented $ANSYS^{®}$ [DGI87], *i.e.* a commercially available finite element method (FEM) software package, to model the magnetic field distribution in order to both predict and to optimize the magnetic force component of a redesigned MTMG. The FEM model was used to evaluate various magnetic geometries using an 8-node quadrilateral magnetic element, a 2-D infinite boundary element for the surrounding air and a Maxwell Surface Force solution.

We chose to analyze NdFeB as the hard ferromagnetic material since it currently has the largest energy density of the hard ferromagnetic class of materials [Oh99]. For the soft ferromagnetic material, we chose to analyze Gd since it represents the same material used in the original MTMG design. We specifically choose to vary the horizontal x-axis width and the vertical y-axis thickness of both the hard and soft magnets (see Figure 3.1 for the result of one test). In addition, the gap distance was varied between the materials. The resulting simulation predictions of force can be found in Table 3.1. This simulated data compares reasonably well with some of the data provided in [UCL07]; however, the plot shown in Figure 3.2 reveals a possible anomaly. The magnetic force is expected to increase with increasing Gd thickness and instead, we observe an unexpected drop in magnetization for the cases of 50 and 70 micron. This anomalous result is attributed to modeling error, although the cause of the error remains uncertain.

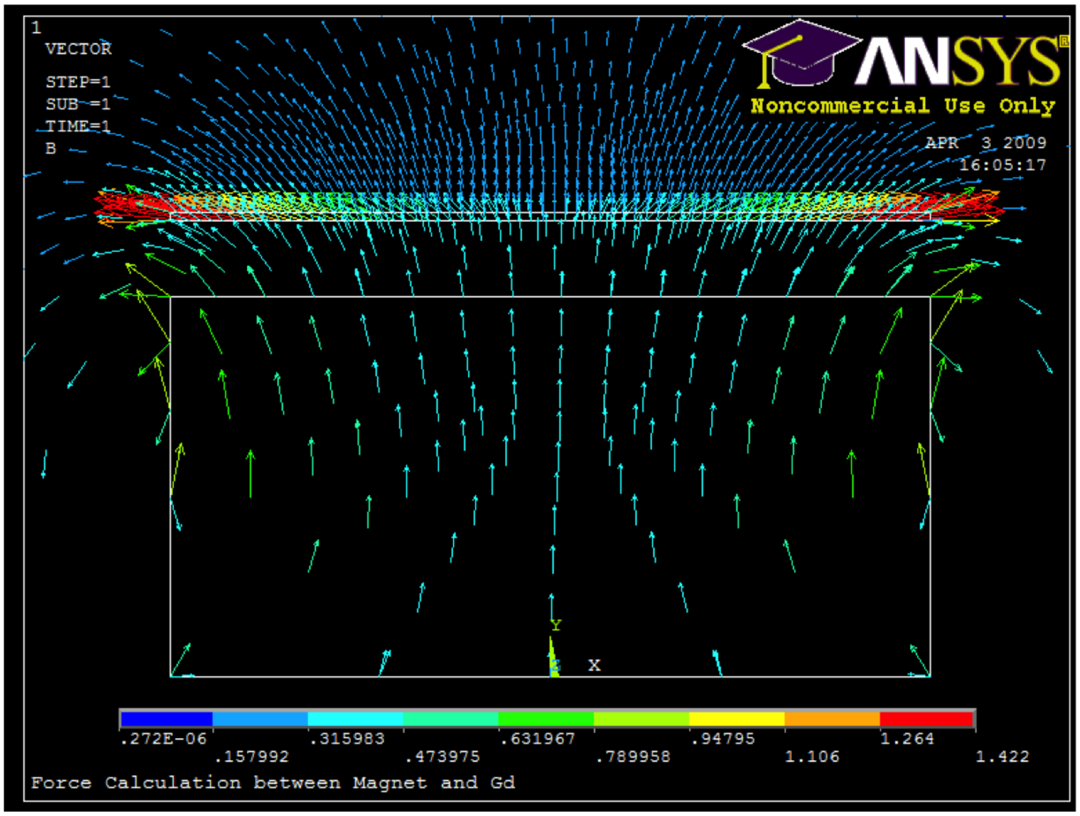

Figure 3.1: $ANSYS^{\circledR}$ modeling of the magnetic force of attraction between gadolinium (top rectangle) and NdFeB (bottom rectangle).

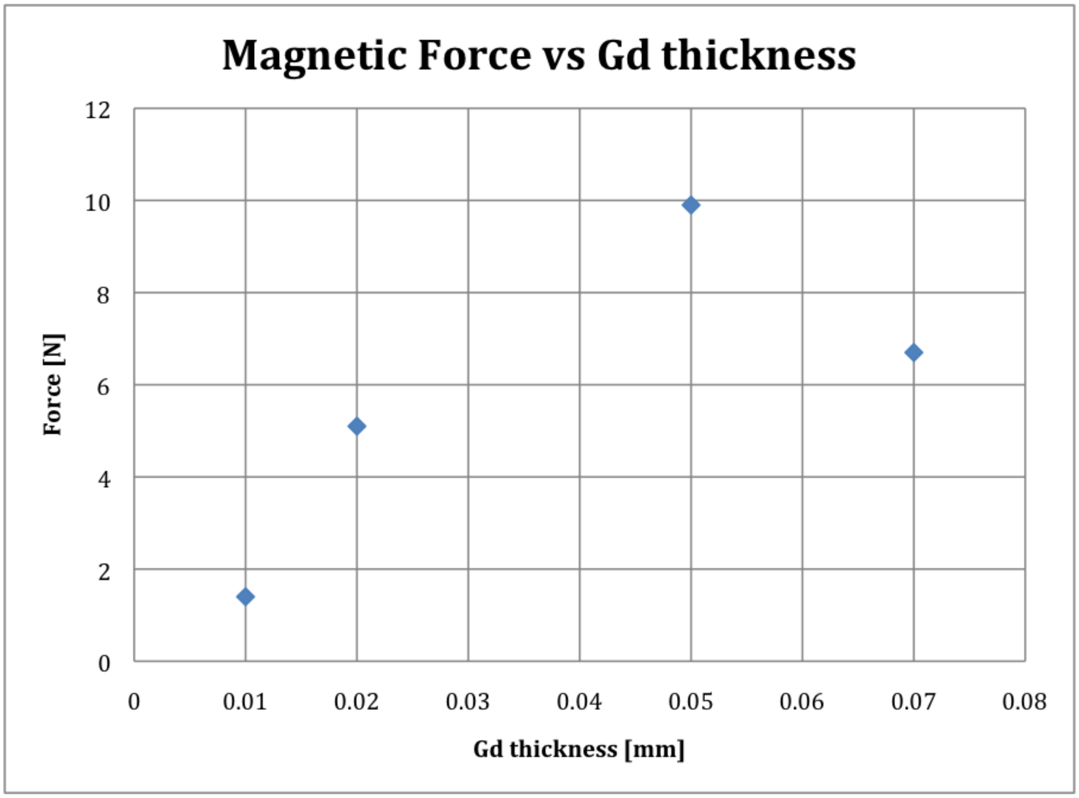

Figure 3.2: Simulation results revealing an anomaly between magnetic force and gadolinium thickness.

Test	NdFeB		Gd		Gap	Force
No	x [mm]	y [mm]	x [mm]	y [mm]	[mm]	[N]
1	1	1	1	0.02	0.1	5.1
2	0.5	1	1	0.02	0.1	4
3	1.5	1	1	0.02	0.1	2.2
4	1	0.75	1	0.02	0.1	2.6
5	1	0.5	1	0.02	0.1	1.1
6	1	0.25	1	0.02	0.1	0.5
7	1	1	0.5	0.02	0.1	1.4
8	1	1	0.25	0.02	0.1	0.9
9	1	1	1.5	0.02	0.1	4.7
10	1	1	1	0.05	0.1	9.9
11	1	1	1	0.01	0.1	1.4
12	1	1	1	0.07	0.1	6.7
13	1	1	1	0.02	0.2	2
14	1	1	1	0.02	0.5	0.3
15	1	1	1	0.02	0.05	12.2

Table 3.1: Simulation results for an optimization problem that considers the magnetic force between a soft ferromagnetic material in Gd and a hard ferromagnetic material in NdFeB.

3.3 Heat Transfer

In general, the power density of the original MTMG device is a linear function of frequency, which in this investigation is primarily limited by thermal cycling time. The thermal cycling time of the ferromagnetic element in this microscale device can be estimated using a lumped capacitance model as the product of the thermal capacitance and the thermal resistance, the so called RC time constant [BYC05] [CMY69] [Mik74] [MYM04]. The magnitude of thermal interface resistance is thus governed by the mechanical and thermal properties of the interface materials, their surface roughness and the applied force. To achieve faster thermal cycling times, we focus on the issue of interfacial thermal contact resistance due to surface roughness.

A primary source of the thermal contact resistance between two solid surfaces with finite roughness is incomplete contact. Heat conduction can only occur at places where the asperities of one surface physically touch the other. Therefore, the asperity deformations, under finite contact pressure, control the amount of heat transfer. Previous analysis in this field found an approximate value of this thermal contact resistance for the original MTMG as $1cm^2K/W$ [BJC09] [CBS09]. In the following experiments, we aimed at reducing the contact resistance of Gd by polishing its surface [CBS09].

We follow the procedure outlined in Figure 3.3 in order to quantify the effect of surface roughness on heat transfer. We begin by considering two different types of samples for comparison. In the case of Sample A, Gd has dimensions of 6x6x0.62mm and requires a minimum 0.2 micron peak-to-peak surface roughness on both of the 6x6mm sides. On the other hand, Sample B consists of a Gd substrate (with the same planar dimensions as sample A), with two sputtered layers of Gold (Au) on its top and bottom surface and is constrained to the same surface roughness tolerance as for Sample A. Other constraints and considerations for this process include: (1) samples should have very little or no curvature at all, (2) no particular thickness after polishing and/or gold sputtering was required, (3) the 6x6mm sides should be as parallel as possible after polishing and/or sputtering and (4) Gd tends to react strongly with water and with air.

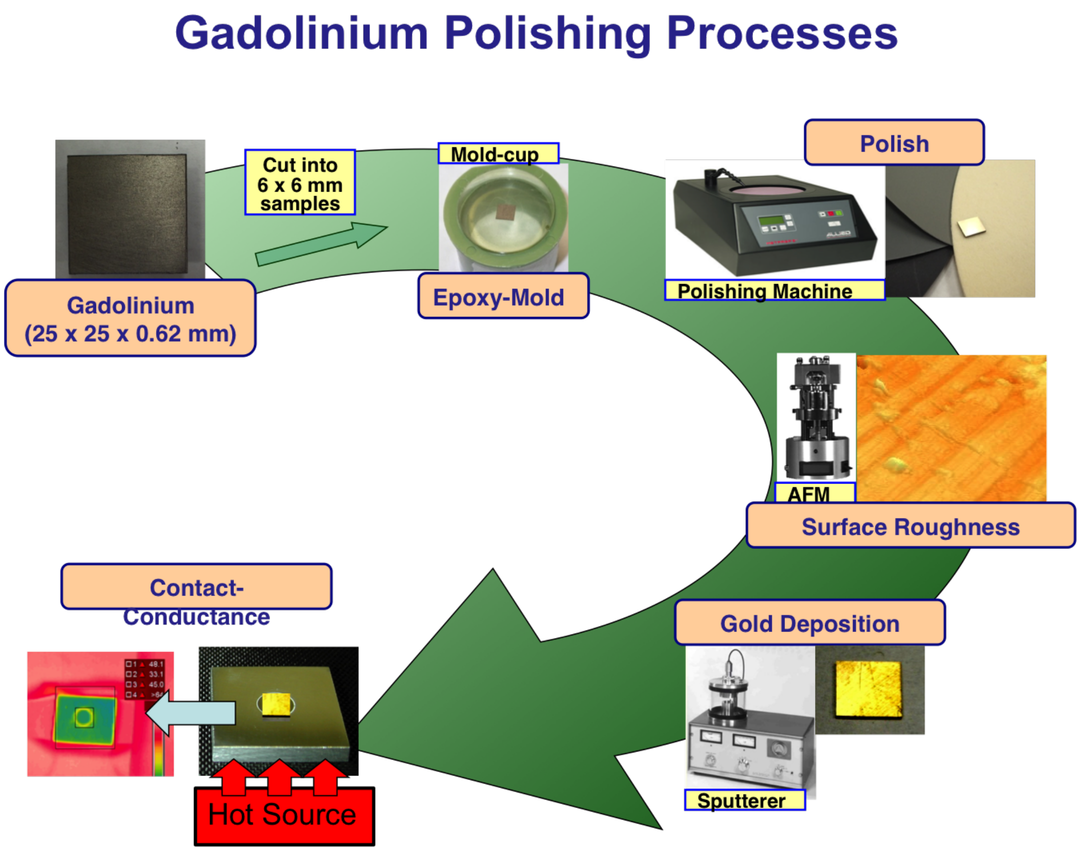

Figure 3.3: Polishing process to determine gadolinium thermal performance based on surface roughness.

The polishing process begins by mounting a sample of as-received (AR) Gd onto a mold-cup, where a 5:1, epoxy:hardener, mixture was added and allowed to cure overnight at room-temperature. After the sample is pulled away from its mold-cup, a 600-grit rough grind ensues until a uniform track pattern emerges, which was observed using a x100 magnification optical microscope as shown in Figure 3.4. Many samples were polished to various degrees and their surface roughnesses were characterized by an atomic-force microscope (AFM). A typical image of the surface produced by the AFM is shown in Figure 3.5, with the resulting characterizations of all samples given in Table 3.2. The surface characteristics of these samples were also measured using a Wyko optical profiler, with the results given in Table 3.3. We note that both methods of surface characterization are from different samples and each reveal an order of magnitude improvement on surface-roughness for the diamond polish when compared to the as-received (AR) samples. Nevertheless, the smallest surface roughness produced by this polishing process was 365 nm, which is almost two times larger than the goal of 200 nm.

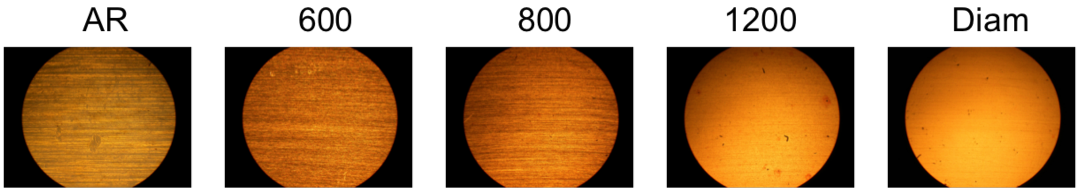

Figure 3.4: Optical image of as-received gadolinium surface and after polishing using various grit sizes.

Polish Type	Thickness [micron]	Roughness p-p [nm]
As-Received	628	1788
600-Grit	535	989
800-Grit	549	1038
1200-Grit	356	948
Diamond	525	716

Table 3.2: Resulting Gd surface roughness, given as peak-to-peak distance using atomic-force microscopy.

We note here that Gd surface processing in this manner is not recommended

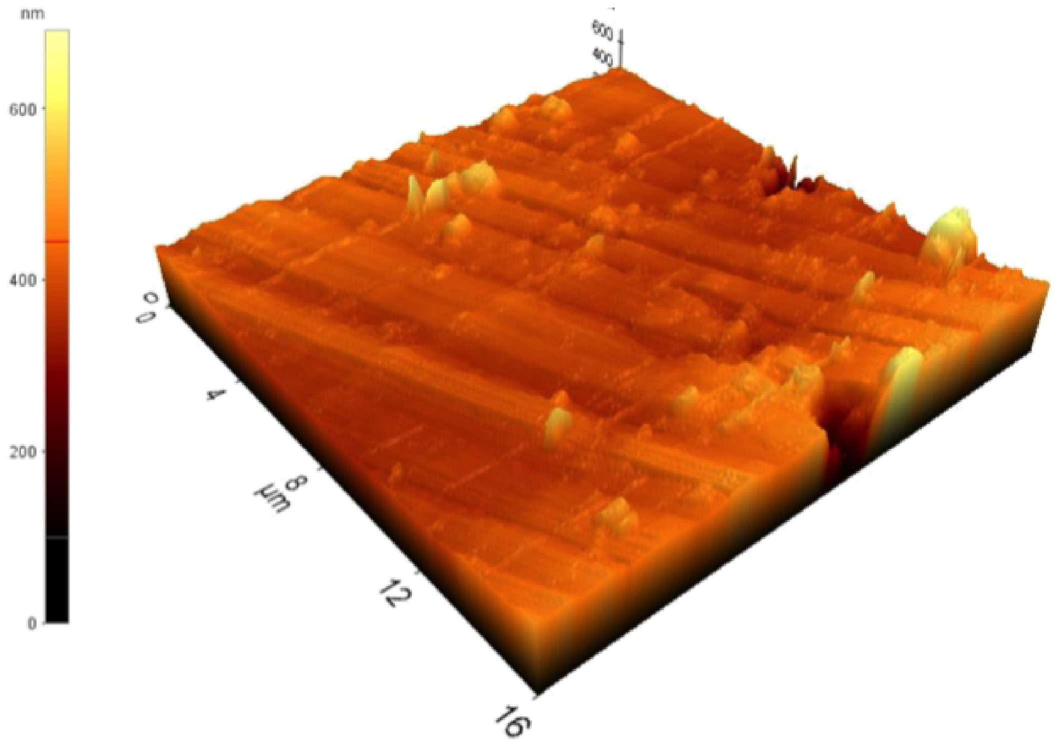

Figure 3.5: Atomic force microscope image of gadolinium surface after a 1200 Grit polishing process.

Specification	Thickness [micron]	Surface Roughness p-p [micron]
1200 Grit	356	0.900
$D - 3\mu$	525	0.365

Table 3.3: Surface roughness measurements on a Wyko optical profiler for a 1200-Grit and a 3μ diamond polish sample.

for two important reasons. First, heavy oxidation was observed at all points in the process and could not be avoided; its effect could not be quantified in this study, though this issue must be addressed and resolved for an optimally tuned MTMG. Second, and most important, since both sides of the Gd sample required polishing for testing, we observed different tilt angles among samples. In other words, the slight curvature at the bottom of each mold-cup, which is purposely designed to help set the sample in the correct position, became a hindrance after the second run for the opposing surface. The resulting tilt was so severe that thermal contact conductance testing could not be completed on these samples. Therefore, a different approach to polishing Gd is suggested.

3.4 Harvest by Electromagnetic Induction

In this section, we explore alternate means of energy conversion for MTMG technology. In particular, we investigate an electromagnetic induction coil as an alternative to ferroelectric transduction [ASH08] [CBS09]. One advantage of this approach is the potential for direct energy transfer via a magnetic circuit, *i.e.* no mechanical interface, which is one reason why early TMG devices adopted this approach in their analyses [BI48] [Ell59] [Ros67] [Sol88] [Sta59] (see section 2.3.2 for more information). In other words, at least some of the kinetic energy in the original MTMG spring mechanism design must remain unconverted due to a lack of perfect efficiency from the ferroelectric transducer [AS07] [CST13] [RCW06] [SIP04].

In the electromagnetic induction approach, a permanent magnet and a movable thermal-magnetic switch, which is wrapped inside a solenoid, can be designed to form a magnetic circuit. The repetitive thermal cycling, due to periodic contact between Gd and a hot-side permanent magnet, would then cause a magnetic flux oscillation in the magnetic circuit, which then induces an electromotive force within the solenoid [Max81]. We focus on modeling this idea before proving the concept in two different ways.

3.4.1 Analytical Modeling

The schematics on the left of Figure 3.6 show the open and closed states of a magnetic circuit. These circuits were modeled using $ANSYS^{®}$ 2-D planar elements, so that the induction could be predicted within the magnetic circuit. The picture on the top right shows the meshing elements used for this model. This model predicts a change in induction between the open and closed circuits of about 0.4 Tesla, which can then be used to predict the output power, here given as 157 mW.

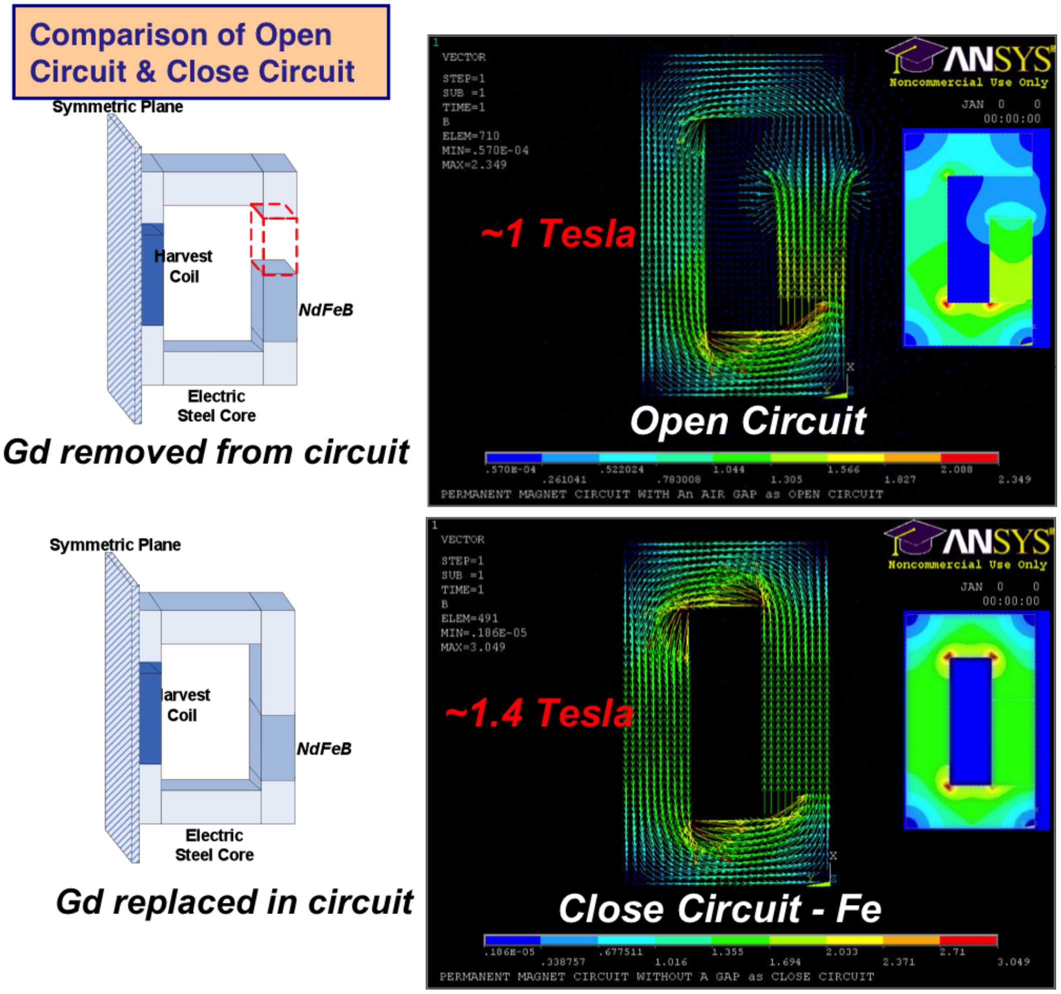

Figure 3.6: Schematic illustration of two-states (left), resulting $ANSYS^{®}$ simulation of induction across the material boundary (right), open-circuit state (top) and closed-circuit state (bottom).

We also attempted to prove the concept of a contactless TMG in a different way, now as a stand-alone system [ASH08] with no artificial switching, *i.e.* other than the artificial thermal gradient necessary for operation. In particular, we model the magnetic circuit based on the design shown in Figure 3.7, with the resulting simulation given in Figure 3.8. We observe the potential of this design to be able to harvest energy from both the spring, *e.g.* via ferroelectric transduction, as well as electromagnetic induction; though here we only consider the latter. This concept design is analyzed in section 3.4.2.

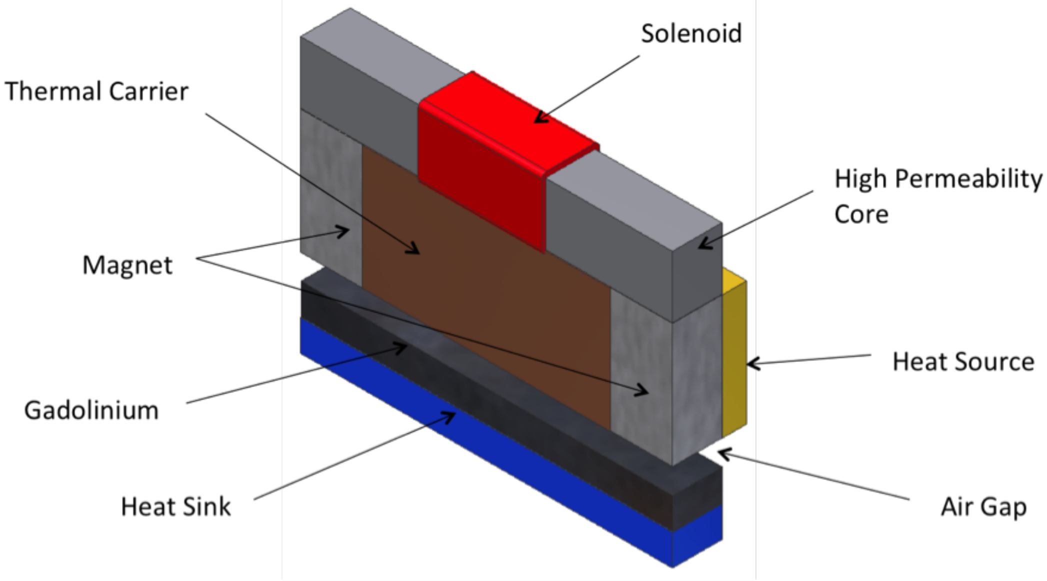

Figure 3.7: Design of a mechanically induced thermomagnetic generator [ASH08], using the electromagnetic induction method to harvest energy.

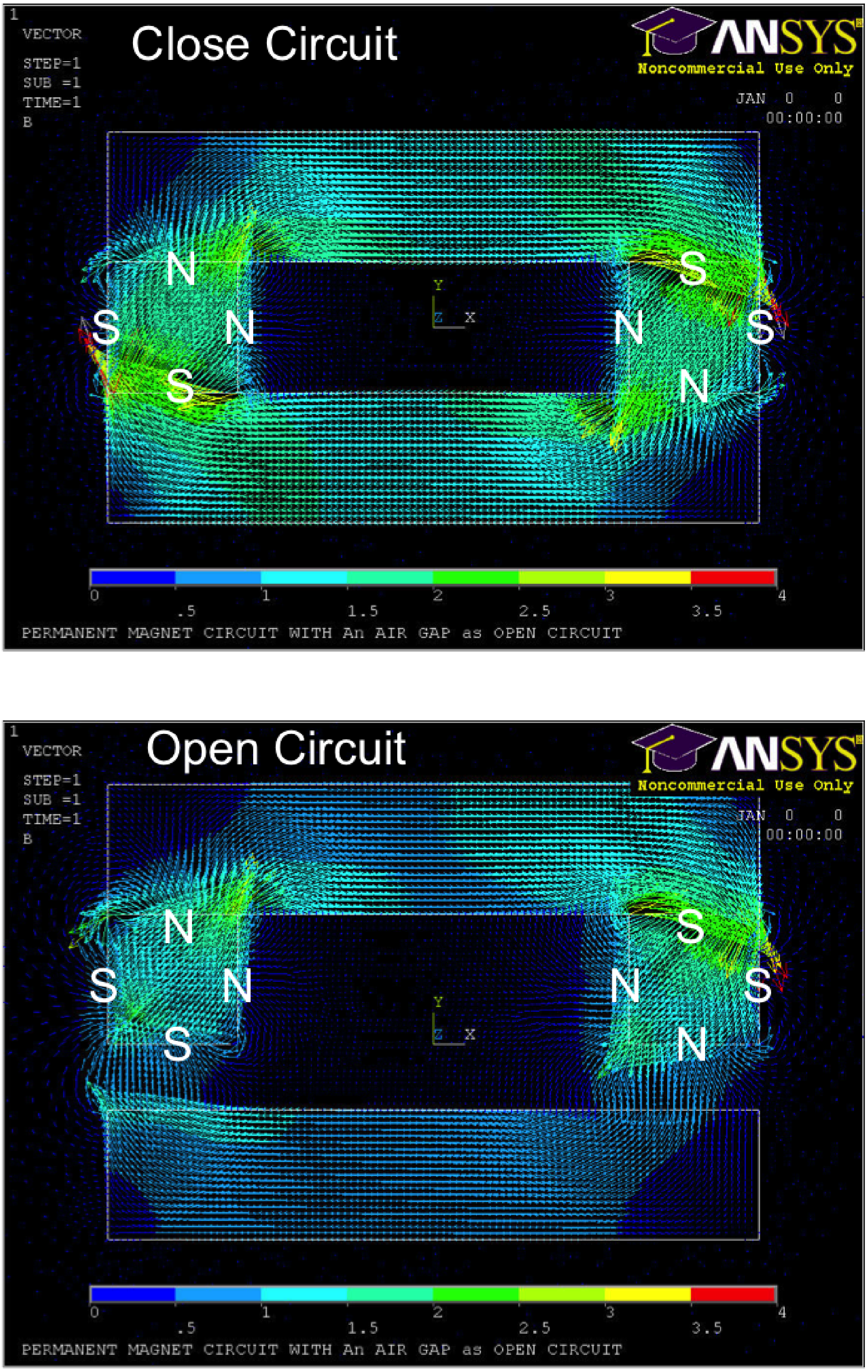

Figure 3.8: Simulation results for a stand-alone system representing a multiferroic thermomagnetic generator, based on schematics in Figure 3.7.

3.4.2 Experimental Test Setup & Results

An aluminum flywheel is used to mimic the thermal cycling of the ferromagnetic switch in order to prove the concept of a contactless MTMG, illustrated in Figure 3.6. As the flywheel turns, the working body will open and close the magnetic circuit as shown in Figure 3.9, *i.e.* mimicking a change from a ferromagnetic state to non-ferromagnetic state for a total of six times per flywheel revolution. Three different switch materials were used in this study, namely: (1) iron, (2) nickel and (3) silicon steel. Iron produced the largest power density output of 20 mW/cm^2 at a frequency of 160 Hz, as shown in Figure fig:ContactlessTMGresults. One key assumption in this test setup is that the frequency of operation is for a near-ideal thermal contact between the switch and permanent magnet; thereby allowing experiments to run as high as 160 Hz operational frequency. Moreover, the electromagnetic coil operates as expected and may be a suitable option for a TMG.

We also consider a stand-alone design for a unique proof-of-concept. The experimental setup of this device is shown in Figure 3.11, with the results shown in Figure 3.12. From this plot of data, we calculate the RMS power as $P_{avg} = 9.3\text{x}10^{-12}W$, for a load of $R = 10\Omega$ and a frequency of about 0.2 Hz. This small output could not power any relevant sensor, though the data clearly indicates regular signal spikes, which we interpret as the system response to changes in induction over a period of about 10 seconds. Furthermore, the demonstration of this stand-alone device indicates that multiple harvesting modes could potentially be implemented together to improve system output; and thereby also increase system efficiency. We also note that this was not an optimized design. Furthermore, possible design improvements include: (1) the use of stronger magnetic materials, with a room temperature Curie point, to improve performance, (2) reduce the number of interfaces, (3) operate in a vacuum environment and (4) improve the solenoid windings.

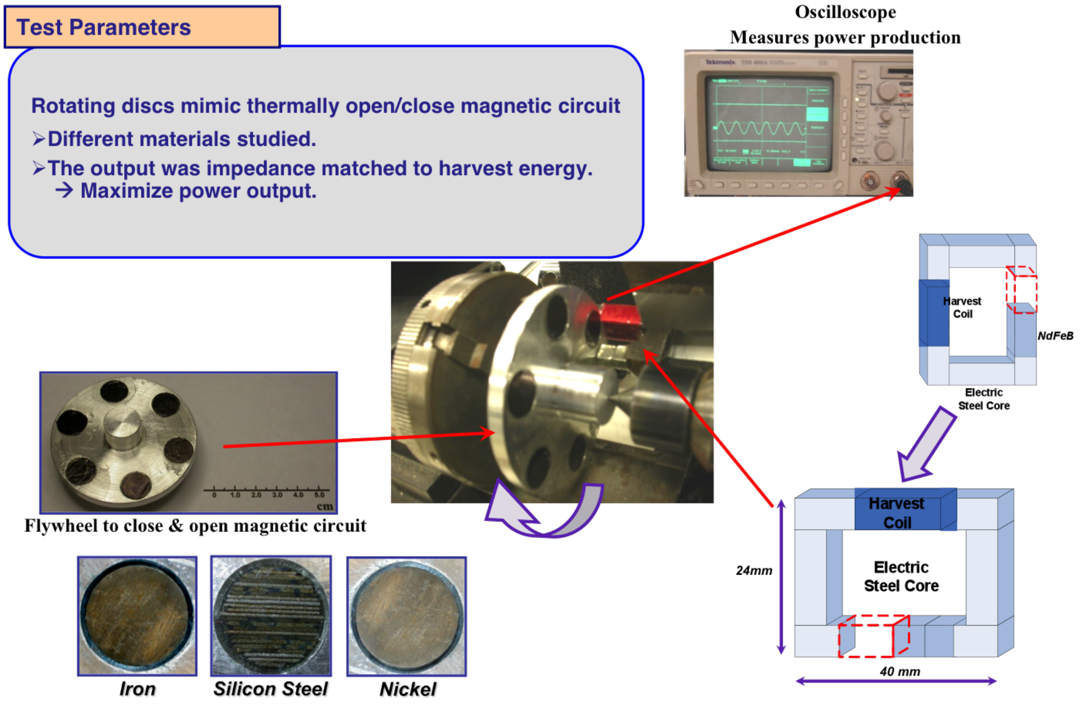

Test Parameters

Rotating discs mimic thermally open/close magnetic circuit

- ➢**Different materials studied.**
- ➢**The output was impedance matched to harvest energy.**
  → **Maximize power output.**

Figure 3.9: Experimental setup for proof-of-concept of electromagnetic induction harvesting for a TMG [CBS09].

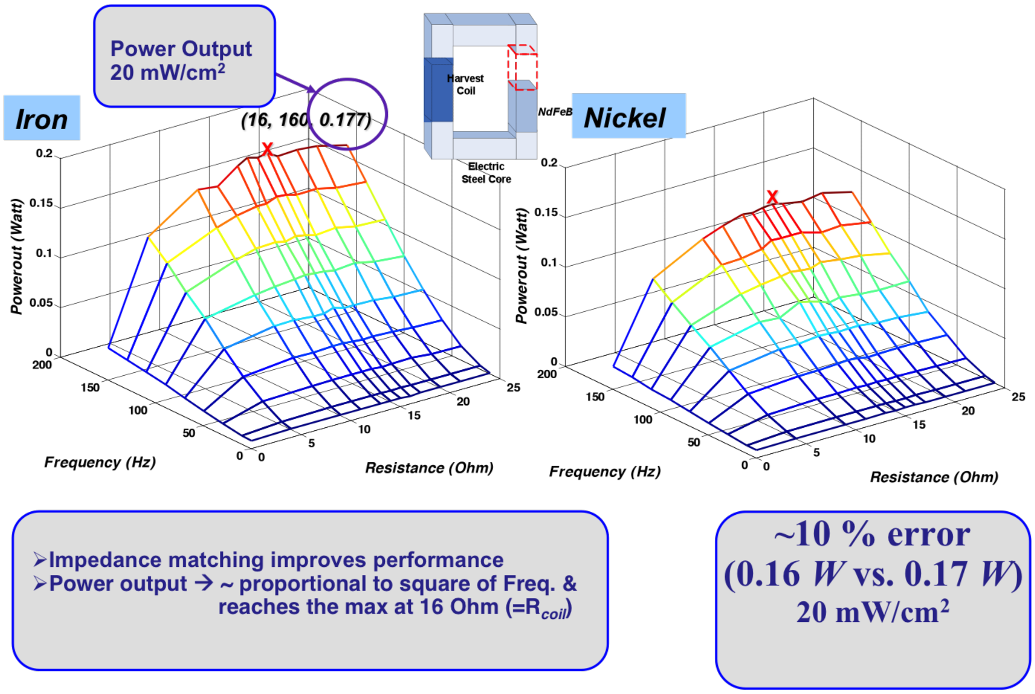

Power Output
20 mW/cm^2

- Impedance matching improves performance
- Power output → ~ proportional to square of Freq. & reaches the max at 16 Ohm (=R_{coil})

~10 % error
(0.16 *W* vs. 0.17 *W*)
20 mW/cm^2

Figure 3.10: Experimental results for proof-of-concept of electromagnetic induction harvesting for a TMG [CBS09].

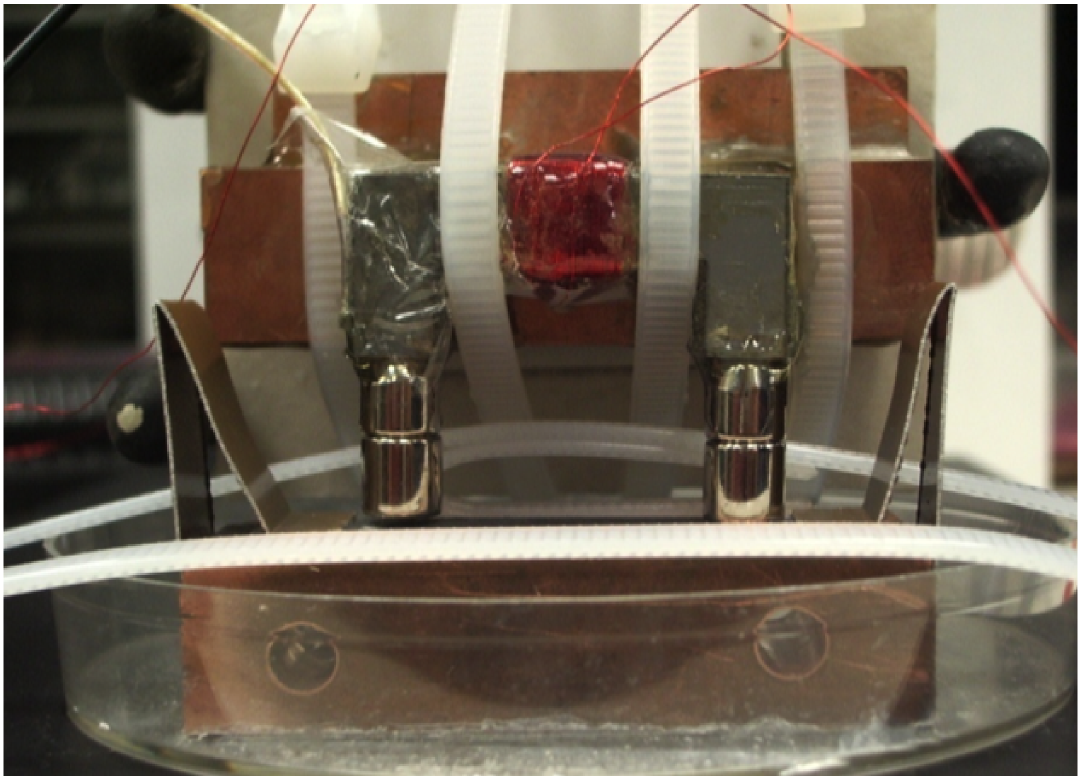

Figure 3.11: Experimental setup for a stand-alone TMG that uses an electromagnetic inductor for electrical energy harvesting, compare with Figure 3.7 and Figure 3.8.

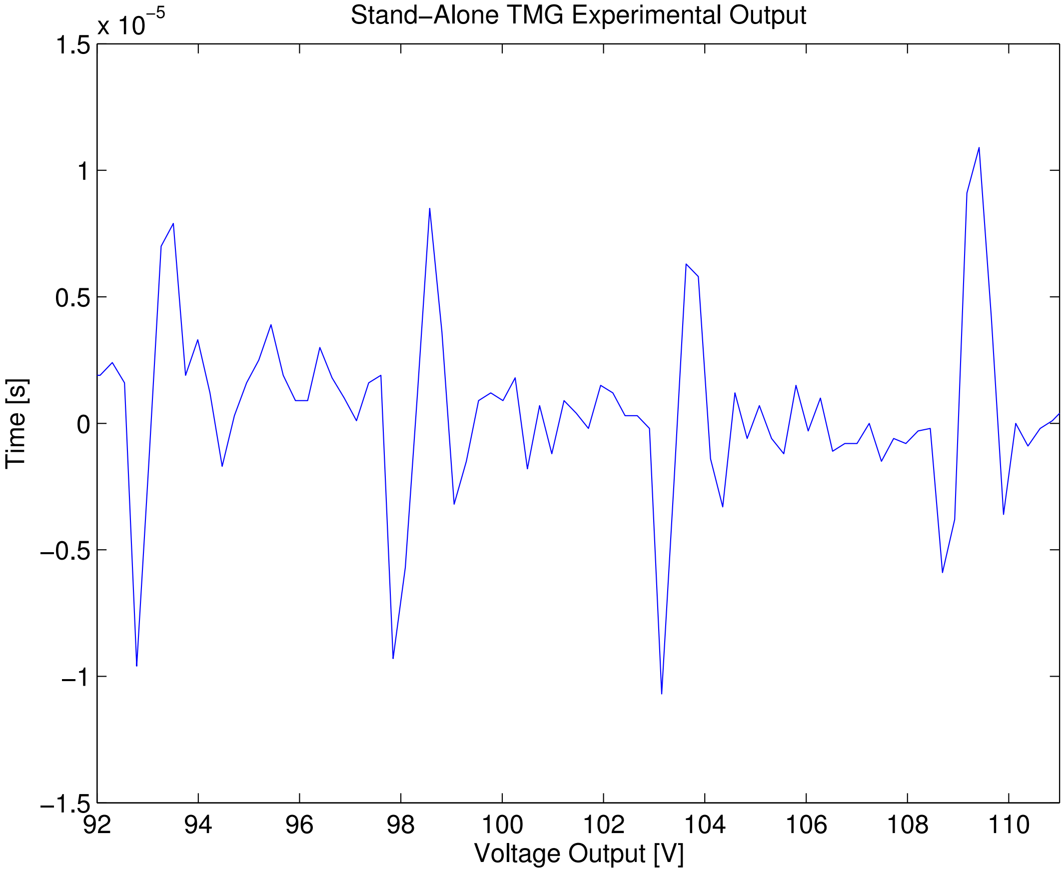

Figure 3.12: Experimental results for a stand-alone TMG that uses an electromagnetic inductor for electrical energy harvesting.

3.4.3 Other Considerations

We investigate models that have yet to be demonstrated in laboratory setting in order to encourage further research aimed at proving the concept, or aimed at a complete redesign. Therefore, we consider a bistable TMG with electromagnetic inductor, which may dramatically improve performance. We also investigate a cascaded TMG design, which may improve efficiency by means of a regenerative method.

It is widely known that reversing the direction of the induction vector will increase the current output of an attached coil, *e.g.* as in an electromagnetic induction motor, due to the large magnetic flux change. This idea is captured by the design shown in Figure 3.13, where two circuits operate 180° out of phase, such that when one circuit is open the other is closed and vice versa [CBS09]. Such a system, can be considered as a bistable TMG, since only one working element is ever magnetically stable during the hypothetical operation. This idea was confirmed by $ANSYS^{®}$ modeling, though no proof-of-concept has been demonstrated to date. Nonetheless, this design holds potential for TMG harvesting by electromagnetic induction and spring mechanism.

We also simulated a cascaded version of the MTMG design, as shown in the top of Figure 3.14, and present the simulation results of magnetic force (shown in the bottom of the same figure). We note that a hard ferromagnet like NdFeB cannot be used at each node in this cascade design and must remain at the bottom hot-side. In other words, a hard ferromagnet at each node in this design would compete with adjacent working bodies and thereby reduce performance. This simulation further suggests that the further Gd is from the bottom the smaller the force of attraction and thereby, a smaller output by extension. Therefore, we do not recommend the cascaded design illustrated in Figure 3.14.

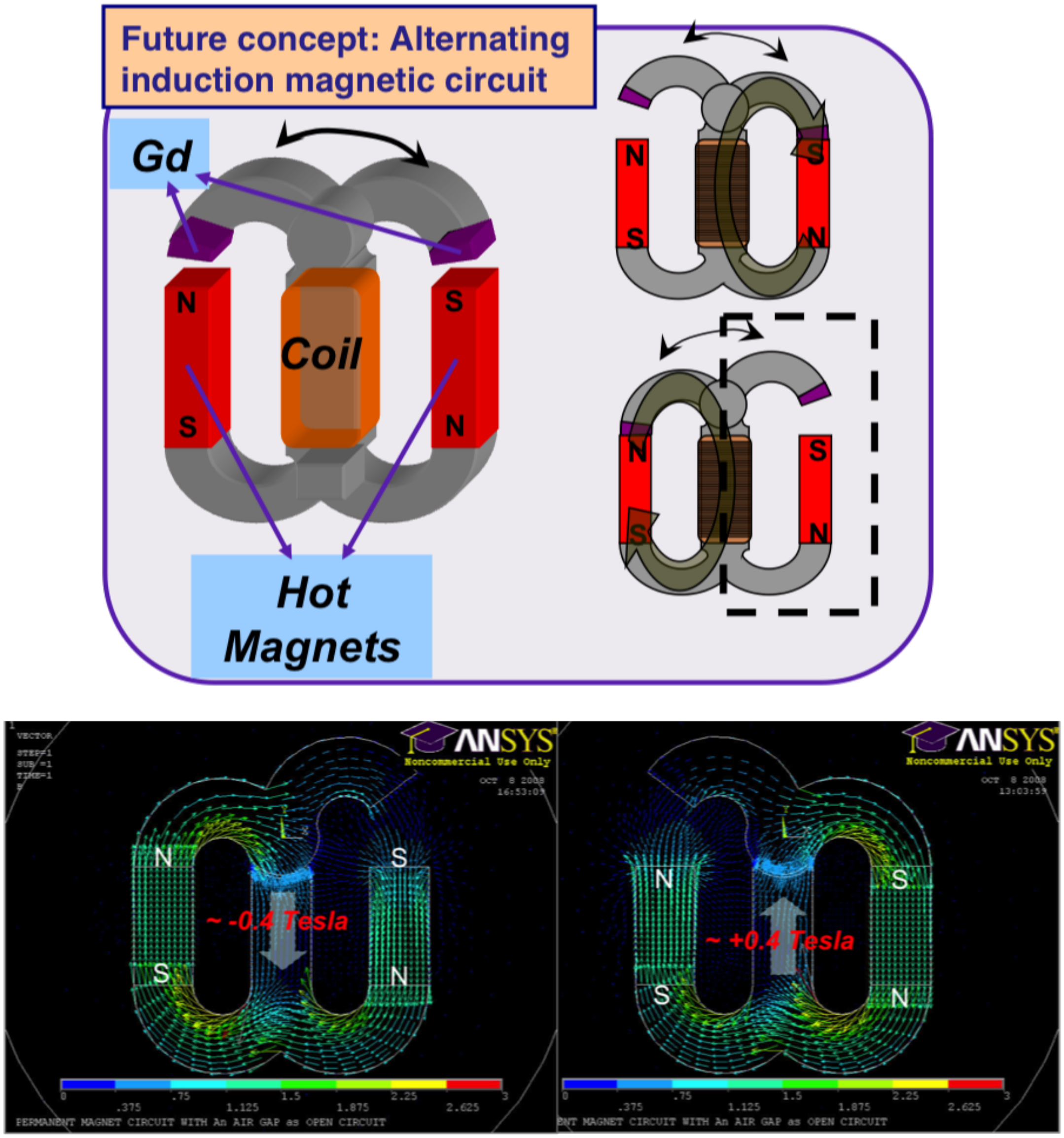

Figure 3.13: Concept of a bi-stable TMG with electromagnetic induction coil [CBS09].

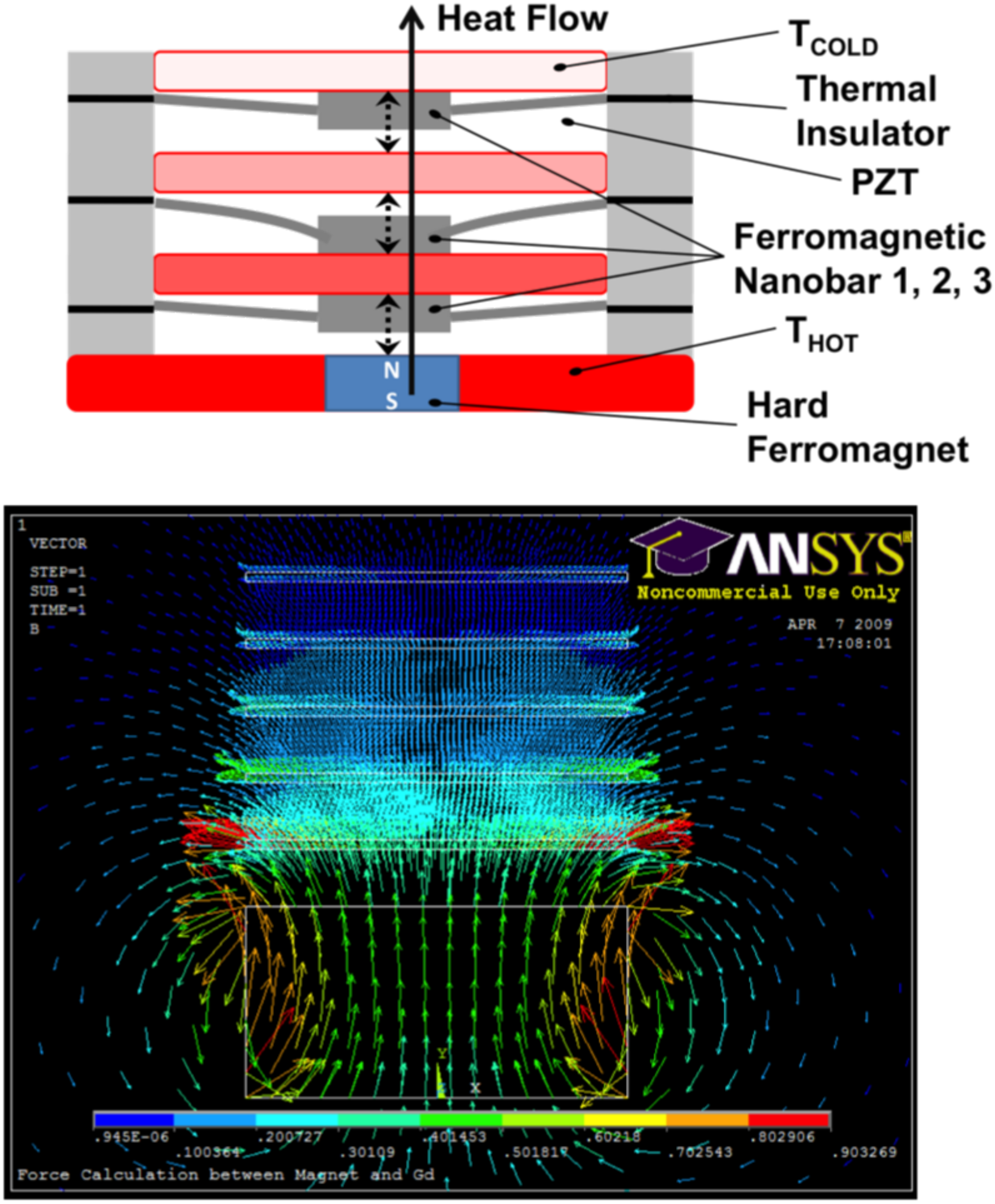

Figure 3.14: Schematic of the cascaded TMG design (top), with simulation results (bottom) [CBS09].

3.5 Summary

Three performance enhancements of a MTMG were considered, including: (1) increasing magnetic force, (2) increasing heat transfer and (3) increasing energy conversion efficiency. First, a $2D$ optimization study was carried out aimed at understanding how the geometry of magnetic materials and their relative spacing affected the magnetic force between them. Some of the test results conflicted with observed phenomena and as such, the analysis was discarded. Second, the surface of Gd samples were physical processed to produce a smooth surface for maximum thermal contact. Although the polishing process produced samples confirming a smoother surface, the heat transfer analysis could not be carried out to due to defects resulting from the mechanical processing. Lastly, the energy conversion process was changed from a ferroelectric transducer to an electromagnetic inductor for increased efficiency. This concept was proven by a combination of simulation and experimental verification, which indicates that an electromagnetic induction coil may be a better design option. The concept of a combination ferroelectric transducer and electromagnetic induction coil was also proven by analysis and experimental verification. In addition, a unique concept for increasing efficiency by means of a cascade design was also investigated; however, flaws in this design suggest that the device may not benefit as expected. The analytical definitions of thermodynamic efficiency for a MTMG design are be established in the next chapter.

CHAPTER 4

Thermodynamic Efficiency Analysis of a Multiferroic Thermomagnetic Generator

4.1 Introduction

We begin this chapter by referring to the idealized multiferroic thermomagnetic generator MTMG [UCL07]; though the focus here shifts towards establishing the thermodynamic efficiency of this device. We justify this focus by recalling the biological example of an ATP enzyme from Chapter 1 and represented as a black-box in Figure 1.2. In Chapter 1, we highlighted the exceptional efficiency of an ATP enzyme, which here serves as a lofty goal and also serves as an argument for the fundamental study of TMG efficiency at comparable scales, *i.e.* the nano scale or smaller. We also emphasize here that the ATP enzyme does not fit our criteria to be considered as a type of thermal-electric energy harvesting device; for example, an input temperature gradient is required in all TEHDs. As such, we may only qualitatively compare efficiencies of these competing energy generators [Aut07]. Nevertheless, we aim to establish MTMG efficiency values for the bulk state in this chapter, in order to predict the efficiency for scaled down versions of this MTMG technology in the next chapter.

We begin by considering the MTMG as an ideal thermodynamic power-cycle, as shown in Figure 1.2 (right), such that we may apply standard definitions for both absolute and relative efficiency regardless of any dynamics that may be occurring within the black-box [Bej88] [BI48] [CBK11] [SBS13]. In Chapter 2 we viewed the black-box dynamics from the perspective of ferromagnetism and with an emphasis on the second-order transition. We now focus on establishing the relative thermodynamic efficiency of this unique MTMG in order to investigate potential device improvements. We first review existing thermodynamics analyses from Solomon in 1988 and Brillouin in 1949 in order to define the relative efficiency of a general TMG. These analyses are then applied to an idealized MTMG cycle for further consideration. Finally, we consider improving the relative efficiency of a MTMG based on ferromagnetic material considerations.

4.2 Solomon Efficiency

We refer again to 1.2 (right) and comment here that no matter what may have occurred inside the black-box of a fully operational TEHD, the input heat must equate to the sum of both the output work and the output heat. This restatement of the first-law of thermodynamics must be satisfied throughout every process, as well as over the span of one operational cycle. Furthermore, the second-law of thermodynamics establishes an upper-bound efficiency limitation between any two operating temperatures, also known as the Carnot power-cycle limit, for which we subsequently use as a baseline for comparing relative efficiency values among distinct power-cycle systems [Bej88] [CBK11]. All of the chosen models for efficiency reviewed here implement both of these thermodynamic relations; however, they each make different assumptions and therefore, in general, do not predict the same efficiencies.

We follow the method of Solomon [Sol88] [Sol91] to formulate the thermodynamic efficiency of a MTMG. Here, we consider the following cycle of four processes, they are: 1) heat rejection at constant field, 2) work of the permanent magnet at constant temperature, 3) heat input at constant field and 4) work of the spring at constant temperature. This type of cycle is known as a Stirling cycle

[Bro77] [Pet10]. The thermal and magnetic energies are calculated for entire cycle, as well as for each process, such that the definitions of thermodynamic efficiency may then be applied.

The theoretical maximum work output of a thermomagnetic generator cycle is assumed to be the total change in magnetic energy [BI48] [Ell59] [Ros67] [Sta59] [Sol88]. When a material is placed in a magnetic field, an incremental amount work energy *from* the working body may be calculated using equation (4.1) [Boz93].

$$W = -\mu_o \int H dM \tag{4.1}$$

Where H is the applied field, M the magnetization and μ_o the permeability of free space. This incremental work is a result of the reorientation of the working body's magnetic dipoles, which tend to lie along the field direction [Boz93]. Likewise, when heat is transferred in and out of the system boundary, *i.e.* the physical boundary of the working body, any changes in magnetization at various applied fields may allow the system to produce work. The work output for a TMG cycle is then given in equation (4.2) as the sum of all the work contributions resulting from each process [Sol88] [Sol91].

$$W_{cycle} = -\mu_o \oint H dM \tag{4.2}$$

If the cycle is described on a plot of magnetization as a function of applied-field, then the W_{cycle} is mathematically equivalent to the bounded area [Sol88] [Sol91], as shown in Figure 4.1.

The most obvious way to increase the bounded area and thereby increase the work output, is to increase the applied field. This was was accomplished using a superconducting electromagnetic coil, which had to be kept cool using a cryogenic refrigerator. The net work produced by Solomon's design is negative, *i.e.* more work was consumed to keep the electromagnet cool then what was produced by the TMG system. Therefore, we conclude that a permanent magnet

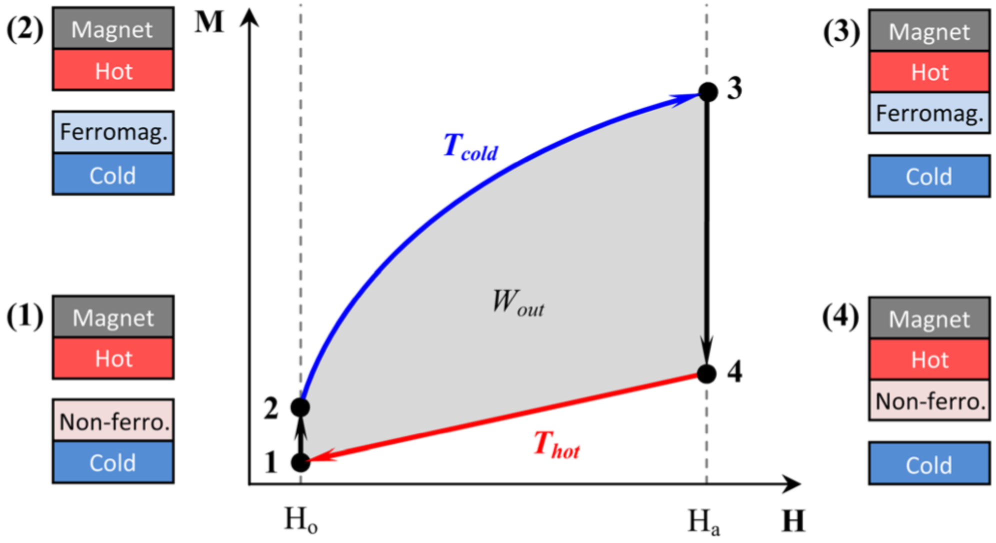

Figure 4.1: Multiferroic thermomagnetic generator cycle description on a plot of magnetization vs. applied field (Image borrowed from Hsu *et. al.* [HSW11a]).

(*i.e.* fixed applied field) is the best design alternative until room temperature superconducting materials become available. We next consider heat across the system boundary.

Thermal energy can be stored within a material if it undergoes a heat transfer process from state (1) to state (2) and may be calculated using the relation given in equation (4.3) [CBK11].

$$Q = \rho \int_{1}^{2} c\,(T, H)\, dT \tag{4.3}$$

Where ρ is the density, c the specific heat as a function of temperature and applied field. For a given temperature range, and zero applied field, an average specific heat capacity value may be calculated as given in equation (4.4) [CBK11].

$$\bar{c} = \frac{\int_{1}^{2} c\,(T, 0)}{T_1 - T_2} \tag{4.4}$$

Therefore, for a zero applied field, equation (4.3) can be reduced to equation (4.5).

$$Q = \rho \bar{c} \, (T_1 - T_2) \tag{4.5}$$

We now consider these heat and work relations for each process in a MTMG system.

A thermomagnetic cycle is idealized in Figure 4.1 as two isothermal processes and two constant-field processes, *i.e.* as a magnetic stirling cycle [Bro77]. The magnetic and thermal energies of each process are examined in the next subsections. The absolute efficiency for the overall cycle is subsequently formulated. This is followed by an alternate, and equivalent, form of the expression for absolute efficiency.

4.2.1 Process $1-2$: Heat rejection at constant field

The first process changes the state of Gd, *i.e.* the working ferromagnetic material, from state (1) to state (2) as shown in Figure 4.1. At state (1), Gd is paramagnetic with a temperature greater than or equal to its Curie point. The applied magnetic field is a minimum since there is a separation distance between Gd and the NdFeB permanent magnet. In general, the applied field is inversely proportional to the square of the gap distance. The gap distance is constant during this process and hence the field is also constant. However, the hot Gd material is, at this point in the cycle, in thermal contact with the cold-side reservoir, which cools the working body to below its Curie temperature. This cooling process transforms Gd from paramagnetic to a ferromagnetic phase, thereby increasing its magnetic order. The work done by the system, resulting from this process, may be calculated from equation (4.1) and given in equation (4.6).

$$W_{1-2} = -\mu_o \int H dM = -\mu_o H_o (M_1 - M_2) \tag{4.6}$$

This work term is similarly evaluated for each process. Also, the heat transfer during this process may be calculated by using equation (4.5) along with experimental data for the specific heat of Gd [GSS54] [JGG66].

4.2.2 Process $2-3$: Applied field at constant temperature

After the cooling process the working body is in a ferromagnetic state and is therefore magnetically attracted to the hot permanent magnet shown in Figure 4.1. The applied magnetic field starts small at state (2), *i.e.* at 100 A/m or less and ends as the maximum applied field at state (3). This maximum field, H_a, which is sufficient to overcome the spring force that holds Gd in place throughout this process, *delivers* work to the Gd system as given in equation (4.7) [CBK11].

$$W_{field} = \frac{1}{V} \int F\left(x, T\right) dx \tag{4.7}$$

Where V represents the volume and F the force as a function of both the spatial position, x, as well as the temperature of the system. In general, the magnetic force of attraction is due to the temperature dependence of magnetization within the hard ferromagnetic material. The integral in equation (4.7) can be evaluated if the magnetic force distribution is known as a function of temperature, such as from experimentally determined data shown in Figure 4.2. During this process, the flight from the cold-side to the hot-side is assumed to take place at constant temperature, $T_2 = T_3 = T_{cold}$; however, heat will be generated within Gd due to the magnetocaloric effect.

Heat may evolve from within a ferromagnetic material whenever it is placed inside a uniform magnetic field, a phenomenon known as the magnetocaloric effect. This phenomenon is best explained by examining the atomic magnetic moments. For example, when the magnetic moments of Gd are aligned due to the applied field, the magnetic entropy is decreased. However, the second-law of thermodynamics prohibits the net entropy change of any process to be negative; therefore, the working body gives up heat such that the net change in entropy is positive. The reverse process will also apply in Process $4-1$; however, we neglect both

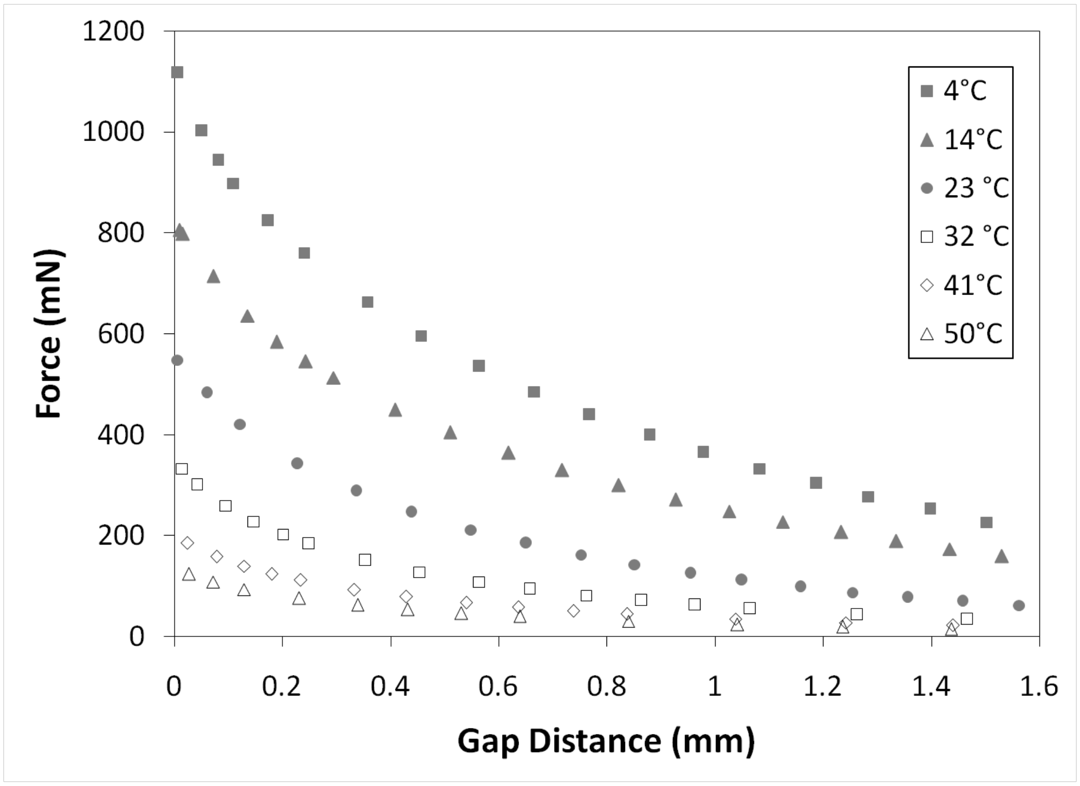

Figure 4.2: Magnetic force of attraction between Gd and NdFeB as a function of gap distance and temperature (Image borrowed from Ujihara *et. al.*[UCL07]).

of these heat terms for this analysis since the applied field isn't large enough to cause a significant change in material temperature [BB81]. In other words, we treat this process as adiabatic, such that we only evaluate work terms.

We note that Gd is not fully saturated throughout this process, such that the change in magnetization may be assumed to be linearly proportional to the applied field. This assumption allows the change in magnetic energy for this process to be approximated using equation (4.1) and in equation (4.8).

$$W \approx -\frac{1}{2}\mu_o(H_a - H_o)(M_2 - M_3) - \mu_o H_o(M_2 - M_3) \tag{4.8}$$

The sum of equation (4.7) and equation (4.8) represents an estimate of the total work for Process $2-3$ and the result is given as equation (4.9).

$$W_{2-3} \approx -\frac{1}{2}\mu_o(H_a - H_o)(M_2 - M_3) - \mu_o H_o(M_2 - M_3) - \frac{1}{V}\int F\left(x, T\right) dx \tag{4.9}$$

At state (3), the working body experiences a maximum magnetization since its temperature is still that of the cold-side and it experiences the largest applied field since the gap distance is zero.

4.2.3 Process $3-4$: Heat input at constant field

The working ferromagnetic body will immediately absorb heat once in thermal contact with the hot-side, such that a phase change occurs, *i.e.* from a ferromagnetic to a paramagnetic phase. However, we do not evaluate this heat term until the first-law of thermodynamics is applied to the overall cycle. Furthermore, we measured the magnetic field at the boundary of a NdFeB permanent magnet in order to estimate the value of H_a as on the order of 230 kA/m. This allows the calculation of magnetic work for this process as given in equation (4.10)

$$W_{3-4} \approx -\mu_o(H_a)(M_3 - M_4) \tag{4.10}$$

4.2.4 Process $4-1$: Spring restoration at constant temperature

After the heating process induces a paramagnetic state, the restorative spring force will displace the system towards its equilibrium position. Here we assume that this system is optimized to such an extent that the spring force is equivalent to the magnetic force, such that for the same gap distance, we can assume that the work contributions from the spring and magnet are equivalent in magnitude, though of opposite sign. In other words, the net displacement of the working body, over a complete cycle, is assumed to be zero since the spring force resets its position. This assumption may also be true for an impedance-matched system and is favorable in terms of device efficiency. We therefore compute the work of this process as given in equation (4.11)

$$W_{4-1} \approx -\frac{1}{2}\mu_o(H_a - H_o)(M_4 - M_1) - \mu_o H_o(M_4 - M_1) + W_{field} \tag{4.11}$$

We neglect the magnetocaloric heat term from this process, *i.e.* just as in Process $2-3$, thus assuming an adiabatic process.

4.2.5 Cycle Analysis

We now consider calculating both the net heat input and the net work output, for one MTMG cycle by summing terms from each of the previous processes. We start by applying equation (4.2) to calculate the net work in this cycle as the sum of the work terms from each process, *i.e.* the sum of equations (4.6), (4.9), (4.10) and (4.11), with the result given in equation (4.12).

$$W_{cycle} = W_{1-2} + W_{2-3} + W_{3-4} + W_{4-1} \approx \frac{1}{2} H_a \left(M_3 - M_4\right) \tag{4.12}$$

Note that this sum cancels out the work contributions from the spring and the magnet due to the impedance-matched assumption that they are designed as equal and opposite forces, acting over the same gap distance. Also, the net work term represents the bounded area of the cycle, shown in Figure 4.1. Thus, we recover the same definition of work as in the method of Solomon, though uniquely applied here to a MTMG. This represents the justification for analyzing the multiferroic system as a type of TMG, as well as for the name MTMG. We may now apply the first-law of thermodynamics to calculate the net heat input over a cycle and the result is given in equation (4.13).

$$Q_{in} = W_{cycle} + Q_{out} \approx \frac{1}{2} H_a \left(M_3 - M_4\right) + \rho \bar{c} \left(T_{hot} - T_{cold}\right) \tag{4.13}$$

Since we have defined the system as the physical boundary of the thermomagnetic switch, we may then define the absolute efficiency as the ratio of the net work produced in a cycle, to the net heat input into the system, as given in equation (4.14).

$$\eta_{abs} = \frac{W_{cycle}}{Q_{in}} \tag{4.14}$$

We may now apply equations (4.12) and (4.14) to (4.14), with the result given in equation (4.15).

$$\eta_{abs} = \frac{\frac{1}{2}H_a\left(M_3 - M_4\right)}{\frac{1}{2}H_a\left(M_3 - M_4\right) + \rho\bar{c}\left(T_{hot} - T_{cold}\right)} \tag{4.15}$$

We assume the heat input term is much larger than the work output term, such that we neglect the work term in the denominator (*e.g.* calculations show that this is a reasonable assumption for low grade heat sources [FST11]). Therefore, the absolute efficiency is approximated as shown in equation (4.16).

$$\eta_{abs} = \frac{\frac{1}{2}H_a\left(M_3 - M_4\right)}{\rho\bar{c}\left(T_{hot} - T_{cold}\right)} \tag{4.16}$$

The second-law of thermodynamics is here applied to define the upper-bound efficiency of any power-cycle, *i.e.* the Carnot engine efficiency, as given in equation (4.17).

$$\eta_{Carnot} = \frac{\Delta T}{T_{hot}} \tag{4.17}$$

Thus, the relative efficiency may then be defined as the ratio of equation (4.16) to equation (4.17), as given in equation (4.18).

$$\eta_{rel} = \frac{T_{hot}}{\Delta T}\frac{\frac{1}{2}H_a\left(M_3 - M_4\right)}{\rho\bar{c}\left(T_{hot} - T_{cold}\right)} \tag{4.18}$$

For example, assume Gd acts as the working body for a thermomagnetic generator that operates between $0 \leq T \leq 50°C$ and operates as an ideal Stirling cycle. For a maximum applied field strength of 230 kA/m, we find the work of the cycle as $W_{cycle} = 1.07\text{x}10^5 J/m^3$, the net heat input as $Q_{in} = 1.39\text{x}10^8 J/m^3$, the absolute efficiency as $\eta_{abs} = 0.08\%$ and the relative efficiency as $\eta_{rel} = 0.5\%$. We note that this measure represents an upper-bound for the considered system due to the assumption of an optimized and ideal system. We also calculated the efficiency of the actual system using this method and based on reported information about power and dimensions [UCL07], we estimate the relative efficiency value as 0.2%.

We note the order of magnitude agreement between these values using Solomon's approach for evaluating efficiency and conclude we have a representative model.

Therefore, we similarly calculated the efficiency of the same Gd system by varying the applied field and the operating temperature ranges, for comparison. Part of the results are given in Table 4.1 [HSW11a] [HSW11b] [SHC10]. The rest of the information about this method can be found in Figure 4.3. In general, we observe that the efficiency of a thermomagnetic generator will increase as the operating temperature is decreased and as the applied magnetic field increases, *i.e.* based on the plots shown in Figure 4.3. We also applied this method to a survey of pure elements [HSW11a] [HSW11b] [SHC10], with the results shown in Table 4.2.

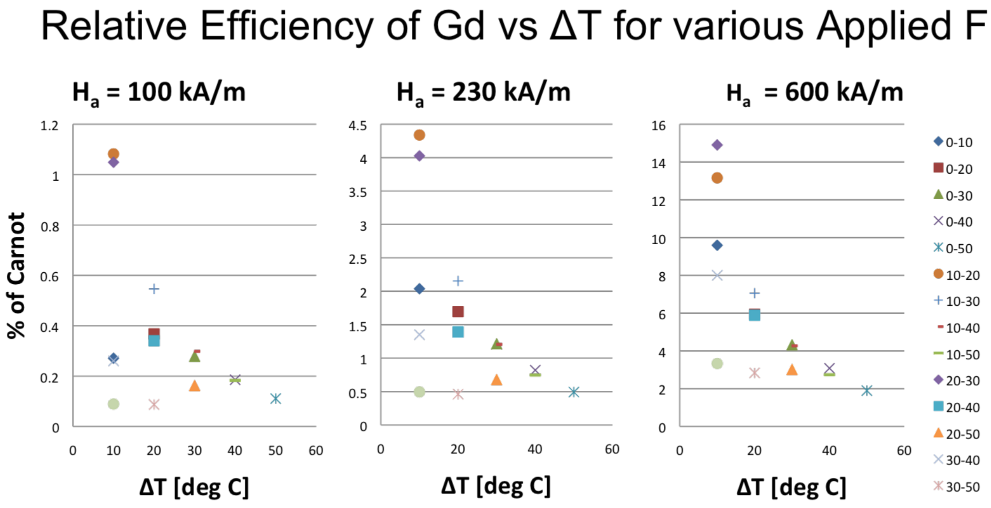

Figure 4.3: The effects of ΔT and H on relative efficiency for Gd as a working body in a multiferroic thermomagnetic energy harvesting device.

T_{cold} $[K]$	T_{hot} $[K]$	W_{out} $[J/m^3]$	Q_{in} $[J/m^3]$	η_{abs}	η_{Carnot}	η_{rel} $[\%]$
0	10	18999	2.64E+07	7.20E-04	0.03534	2.04
0	20	67567	5.84E+07	1.16E-03	0.06826	1.70
0	30	94653	7.88E+07	1.20E-03	0.09901	1.21
0	40	103090	9.83E+07	1.05E-03	0.12780	0.82
0	50	106410	1.39E+08	7.63E-04	0.15480	0.49
10	20	48568	3.28E+07	1.48E-03	0.03413	4.34
10	30	75654	5.32E+07	1.42E-03	0.06601	2.15
10	40	84090	7.27E+07	1.16E-03	0.09585	1.21
10	50	87414	9.44E+07	9.26E-04	0.12384	0.75
20	30	27086	2.04E+07	1.33E-03	0.03300	4.03
20	40	35522	3.99E+07	8.90E-04	0.06390	1.39
20	50	38846	6.16E+07	6.30E-04	0.09288	0.68
30	40	8436	1.95E+07	4.32E-04	0.03195	1.35
30	50	11760	4.12E+07	2.85E-04	0.06192	0.46
40	50	3324	2.17E+07	1.53E-04	0.03096	0.50

Table 4.1: Relevant input parameters and values used to calculate relative efficiency, which is then plotted in Figure 4.3.

Elements	T_c [K]	Magnetic phase transition	Crystal structures	M_{cold} [a] [emu/cm^3] (T_{cold} [K], H_a [Oe])	Max. [b] C_p [$J/mol \cdot K$]	η_{Carnot} [%]	η_{rel} [c] [%]	Ref.
Co	1394	F-P [d]	Poly	139 (1389, 3000 [e])	54.2	0.36	2	[MS51] [BP79]
Fe	1044	F-P	Poly	288 (1039, 3000 [e])	72.5	0.49	3.4	[CG71] [Sha74]
Ni	630	F-P	Poly	76 (630, 3000)	42.5	0.79	3.4	[CG71] [OY01]
Gd	288	F-P	Poly	375 (288, 3000)	52.4	1.71	11.4	[DTP98]
	294		Single	422 (294, 3000)	59	1.67	20.5	
Tb	221	F-A [f]	Poly	1176 (221, 3000)	148	2.21	17.5	[TLS58] [HLS63] [JSC84]
			Single	1180 (221, 3000)			18.1	
Dy	89	F-A	Poly	1028 (89, 3000)	70.8	5.32	7.5	[ELS54] [JCS85] [Woh80]
			Single	2540 (89, 3000)			23.5	
Ho	20	F-A	Poly	1594 (15, 3000)	16.5	25	16.2	[RLS58] [SLS62] [SC89]
			Single	2816 (15, 3000)			57	
Er	20	F-A	Poly	678 (20, 3000)	20.8	20	3.5 [g]	[Coq77][GF88] [GLS61][ELS55][SGS04]
			Single	2430 (20, 3000)			65.1 [h]	

Table 4.2: Multiferroic thermomagnetic generator efficiency model, calculated for a survey of elements acting as a working element [HSW11a].

[a] For single crystal, only the magnetizations along the easy axis were considered.

[b] $C_p(T)$ anomaly appeared in the vicinity of T_c.

[c] $H_a = 3kOe$ and $\Delta T = 5K$ are assumed for all the calculations. Optimistic isothermal magnetization data were chosen from interpolation.

[d] Ferromagnetic to paramagnetic transition at T_c.

[e] M_{cold} at $H = 3000Oe$ was calculated from linear interpolation.

[f] Ferromagnetic to antiferromagnetic transition at T_c.

[g] Calculated based on interpolation using limited isothermal magnetization data for polycrystalline Er.

[h] $\eta_{rel} = 3.4\%$ if using the isothermal magnetization data from Gama *et.al* (1988) [GF88].

4.3 Brillouin efficiency

Here we follow the results of a rigorous thermodynamic analysis of efficiency for an ideal TMG by Brillouin in 1949 [BI48]. A more detailed derivation of all the equations used in this section can be found in the Appendix (see section 4.6); however, the eventual result of this seminal work revealed a maximum of 55% relative efficiency for any material. Here, we make use of a portion of these derived thermodynamic relations and apply the same Stirling cycle dynamics under a set of assumptions that will be covered next. First, the relative permeability of the material is assumed to take the form shown in equation (4.19).

$$\mu = \mu_o + A(\theta - T)^n \tag{4.19}$$

Where $\mu_o = 4\pi\text{x}10^{-7} N/A$ is the permeability of free space, A is a non-zero and positive constant, θ represents the Curie temperature and n an exponential constant. A hypothetical plot of relative permeability is given in Figure 4.4, from which the slope constant A may be extracted; in our case, we compute the slope from measured data collected on a superconducting quantum interference detecting (SQUID) magnetometer for bulk Gd. Next, an assumption on both the temperature, and applied field profiles, requires a sinusoid of the form shown in equation (4.20).

$$T = T_a + b\sin(\omega t) \tag{4.20}$$

Where T_a represents the average temperature, b the temperature amplitude of oscillation and ω the frequency. The range of temperatures, $T_1 = T_{hot}$ and $T_2 = T_{cold}$ respectively, are bound by the relations given in equation (4.21).

$$\begin{aligned} T_1 &= T_a + b < \theta \\ T_2 &= T_a - b \\ \Delta T &= 2b \end{aligned} \tag{4.21}$$

The cycle $T - H$ profile may also be represented in the time domain as illustrated in Figure 4.5 and in the frequency domain as a parametric function shown in Figure 4.6. We specifically choose the profile of T and H to match the MTMG model profile requirement, *i.e.* illustrated in Figure 4.5, of a two isothermal and two constant field processes in a Stirling cycle. In this case, the applied field profile leads the temperature profile by a quarter period phase. From this study, we summarize the efficiency as given in equation (4.22).

$$\eta_{abs} = \frac{T_1 - T_2}{T_1 + \frac{2\bar{c}}{AH_a}(T_1 - T_2)} \tag{4.22}$$

Where $\bar{c}$ represents the average volume specific heat, as defined in equation (4.4). We apply this equation using our chosen properties for Gd as an example.

For example, assume a MTMG cycle consisting of two isothermal and two constant field processes with Gd as a working body. The operating temperatures are between 290 and 295 K. The applied field is between 0 and 230 kA/m. The material properties for Gd are given as $A = 0.10H/(m \cdot K)$ and $\bar{c} = 2.4x106J/(m^3 \cdot K)$. We can may then compute the predicted efficiency using equation (4.22) as

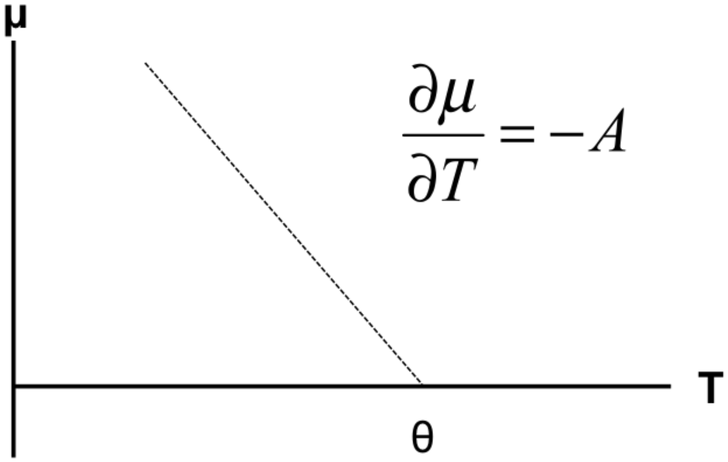

Figure 4.4: A hypothetical description of relative permeability as a function of temperature, from which the slope A may be calculated for efficiency considerations.

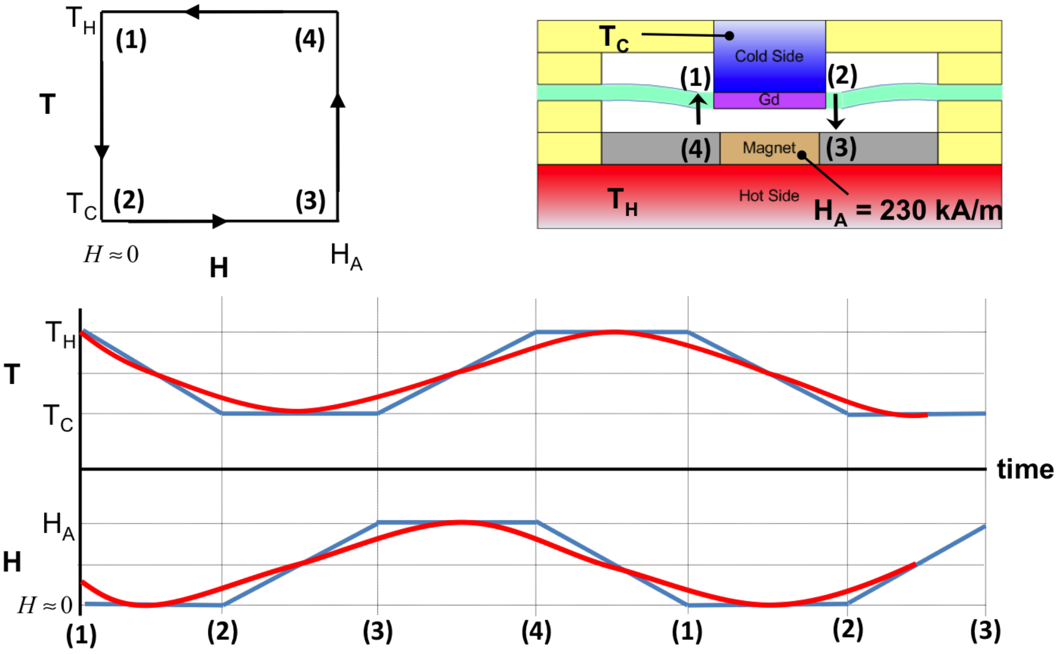

Figure 4.5: Idealized Stirling cycle (top-left) for a multiferroic thermomagnetic generator (top-right), where the ideal (blue) and model (red) temperature and applied field profiles are plotted in the time domain (bottom).

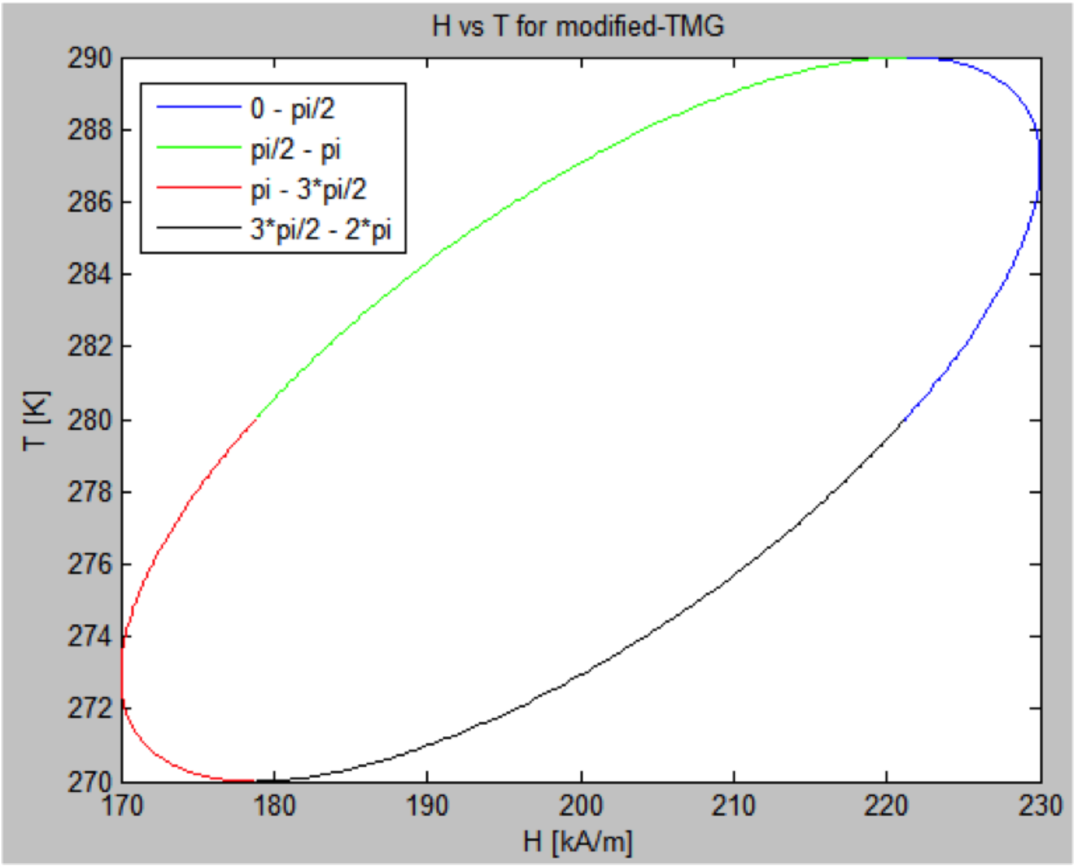

Figure 4.6: Parametric model of a multiferroic thermomagnetic generator cycle, where the temperature and applied field profiles are plotted as a function of frequency.

$\eta_{abs} = 0.13\%$, the Carnot efficiency as $\eta_{Carnot} = 1.69\%$ and the relative efficiency as $\eta_{rel} = 7.7\%$. We then made similar calculations to determine efficiency values for a survey of pure ferromagnetic elements, which are reported in Table 4.3.

Mat.	T_{hot} $[K]$	T_{cold} $[K]$	A $[H/(m \cdot K)]$	c $[J/(m^3 \cdot K)]$	H $[kA/m]$	η_{Car} $[\%]$	η_{abs} $[\%]$	η_{rel} $[\%]$
Gd	293	288	1.28E-07	2.41E+06	230	1.69	0.13	7.7
Ni	632	627	3.09E-07	6.00E+06	238	0.79	0.12	15.67
Fe	1044	1039	3.62E-07	8.51E+06	238	0.48	0.10	20.11
Dy	94	89	4.84E-07	2.89E+06	240	5.32	0.41	7.68
Ho	25	20	7.61E-07	5.86E+05	477	20	8.49	42.46

Table 4.3: Results of the Brillouin approach for evaluating efficiency, assuming the temperature and applied field profiles given in Figures 4.5 and 4.6, applied to several magnetic materials and using the same material references as in Table 4.2.

4.4 Magnetic Single Domain Considerations

We now focus on improving efficiency based on the previous model analyses of a MTMG. First, consider the plot shown in Figure 4.1 and consider the well-established observation from bulk ferromagnetic materials that they tend to have zero remanent magnetization under a zero-applied field. This phenomenon is hypothesized to be due to the presence of magnetic domains [Wei07], which are schematically shown on the left-side of Figure 4.7. On the right-side of this figure, we note that a scaled down ferromagnetic body that behaves like a magnetic single domain (SD) should exhibit a remanent magnetization, even at zero applied field. We hypothesize that this remanent magnetization may potentially improve the efficiency of a MTMG when using the method of Solomon [SHC10] [HSW11b] [HSW11b] and shown schematically in Figure 4.8. For example, we use the Brillouin function (see section 2.3.1) to estimate the reduced remanent magnetization of SD Gd at $T = 287K$ as $M/M_o = 0.225$. This remanence would increase the bounded area to such an extent that the new efficiency values would be $\eta_{rel} = 33.1\%$ using the Solomon method for evaluating efficiency. This result quantitatively supports the qualitative argument of improved efficiency when including remanent magnetization for SD ferromagnetic working materials.

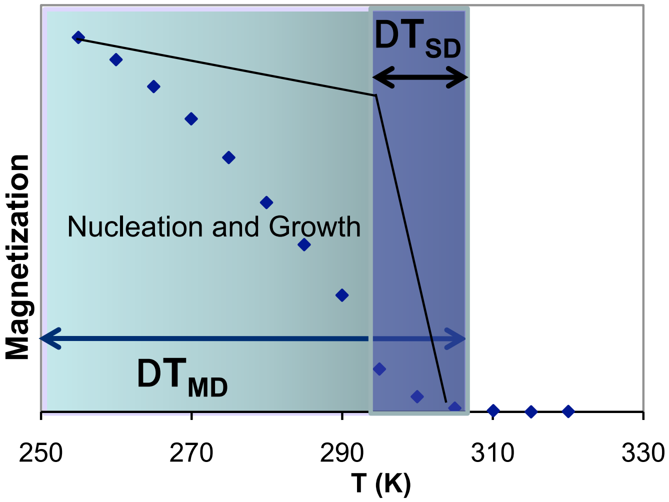

Figure 4.7: A schematic hypothesis of magnetic transition behavior for multi-domain vs. single-domain of gadolinium (right).

We may further hypothesize that the thermal energy required to induce a second-order transformation in a multi-domain (MD) material, may actually be less than that for SD materials representing small permanent magnets. We justify this hypothesis by considering the energy of a domain wall as a barrier that doesn't exist, by definition, in the energy state of a SD. As a consequence, this energy barrier must be overcome in order to induce the second-order phase transformation in a MD material. By eliminating domain walls (*i.e.* energy barriers) the amount of energy required to undergo the phase transformation will decrease and the amount of stored magnetization will increase (*i.e.* due to the absence of competing domain structures). In other words, a bulk sample of a ferromagnet contains many domains and these domains may be responsible for interrupting the point at which magnetic energy is completely balanced by thermal agitation, *i.e.* a gradual, as opposed to sharp, second-order phase transition. A consequence of this hypothesis is that a single-domain ferromagnet will reduce its overall magnetic moment with

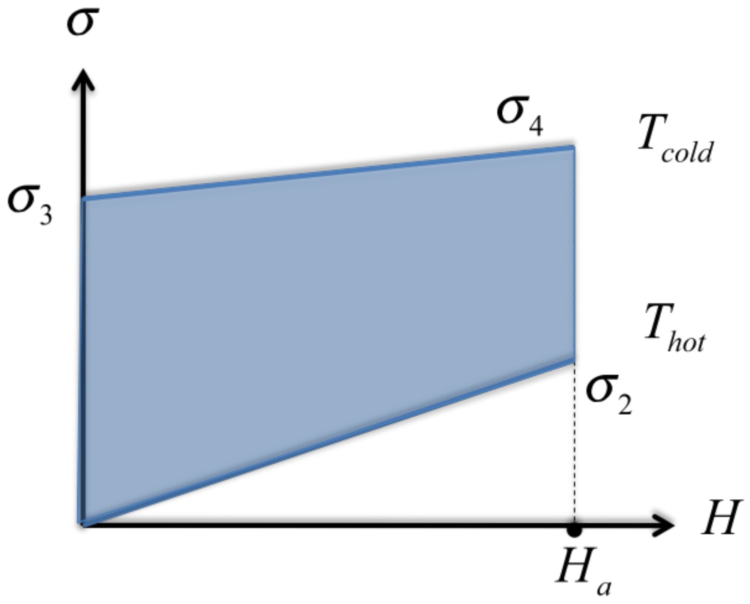

Figure 4.8: The remanent magnetization of a working body can substantially improve efficiency, which depends on the bounded-area of a power-cycle. The bounded are of a single-domain is hypothesized to be substantially larger than that produced by a multi-domain material [SHC10] [HSW11b][HSW11b]. Note that $\sigma = \rho M$ represents the mass specific magnetization.

less applied thermal energy when compared to its multi-domain bulk counterpart; thereby increasing the potential for thermomagnetic energy conversion coupling behavior between these competing geometries.

Thus, we set out to analytically predict the magnetic behavior as a function of applied field and temperature for a SD to further support this hypothesis, *i.e.* even before attempting to prove the concept. This endeavor has yet to yield satisfactory results, probably due to limitations in our adopted theory of ferromagnetism, which fails in the vicinity of the Curie point (*i.e.* recall from section 2.3.1 that no complete theory of ferromagnetic transition as yet exists). This task also proved difficult for current micromagnetics simulation methods, which are based on the Lifshitz-Landau-Gilbert (LLG) equation. For example, the central assumption for a solution to the LLG equation, *i.e.* for a finite-element mesh, requires the temperature to be far below the Curie point in order to ensure a stable saturation magnetization vector. This may be the likely reason why Gd has yet to be modeled as an LLG problem close to room-temperature. However, a modified version of the LLG equation that takes temperature into account, which is based on the Lifshitz-Landau-Bloch (LLB) equation, may be able to model the M-H-T behavior of a single-domain; however, this model requires more computational resources as the temperature range approaches the Curie point [FCF11] [FFB07]. This is explained by considering that the susceptibility diverges near the Curie point, while the magnetic moment behavior becomes unstable. This combination requires a finer and finer mesh in order to spatially resolve the transition phenomena. In addition, any micromagnetics model requires a priori knowledge of the Curie temperature, as well as the complete M-H-T characterization in order to "tune" the magnetic precession behavior. This last point challenged one of the core assumptions thus far, which is a constant Curie temperature for any one material. We break away from this assumption in the next chapter.

4.5 Summary

The thermodynamic efficiency of a MTMG was established in two ways: (1) using the method of Solomon and (2) using the method of Brillouin. First, the method of Solomon was modified to account for the energies due to the mechanical spring and permanent magnet. The resulting analysis compared well with the estimated efficiency from the original MTMG and as such, was applied to a survey of pure elements for further comparison. This method also verified that of the pure elements in this survey, Gd represents the best choice for room-temperature applications and that single crystal Gd would operate around 20% relative efficiency, which outperforms the poly-crystal form by a factor of about two. The traditional $3d$ ferromagnetic materials, with Curie temperatures approaching molten states, showed relative efficiency values of about half that of Gd in polycrystal form, *i.e.* on the order of 1%. On the other hand, the rare-earth elements, with mostly cryogenic Curie temperatures, showed relative efficiency values closer to 50% The second design constraint considers the observation that a larger applied field will translate into a larger net work output, which results in efficiency values approaching their theoretical maximum of around 50%. Lastly, the method of Brillouin was applied to a MTMG as a more rigorous estimate of expected thermodynamic efficiency. This method was also applied to a survey of materials and in each case the predicted efficiency was larger when compared to the method of Brilloiuin. This discrepancy can be attributed to a linear approximation in the method of Solomon, which provides a more conservative estimate of thermodynamic efficiency. The conservative model from Solomon was then reanalyzed to predict the change in efficiency when considering single-domain magnetic materials, which tend to align magnetic energy along a preferred direction in the absence of an applied field. The resulting analysis predicts efficiencies on the order of 30% relative to Carnot, which is a lower-bound estimate that represents about a three-fold improvement over conventional bulk materials.

4.6 Appendix

The derivation of Brillouin efficiency [BI48] begins with the definition of the 1^{st} law of thermodynamics applied to a cycle, given in equation (4.23).

$$\oint dU = \oint \delta Q - \oint \delta W = 0 \tag{4.23}$$

Assuming reversibility, the differential of heat absorbed is given by Maxwell's relations, where T, B are independent variables, and is defined in equation (4.24)

$$dQ = \left(\frac{\partial Q}{\partial T}\right)_B dT + \left(\frac{\partial Q}{\partial B}\right)_T dB = c(T, B)dT + f dB \tag{4.24}$$

Where c is the heat capacity at constant induction, and f is the heat of magnetization, with each term in this equation carrying units of energy density J/m^3. The magnetic work done by the system is given in equation (4.25).

$$-\delta W = HdB \tag{4.25}$$

This work is negative since the system loses energy in order to produce work. The 1^{st} law of thermodynamics, *i.e.* equation (4.23), applied to a process results in the relation given in equation (4.26).

$$dU = \delta Q - \delta W = [c\,(T, B)\,dT + fdB] - [HdB] \tag{4.26a}$$

$$dU = c\,(T, B)\,dT + (f + H)\,dB \tag{4.26b}$$

Where U represents internal energy, and assuming thermodynamic reversibility, this state variable is an exact differential, such that we may apply Maxwell's relations as shown in equation (4.27).

$$dU = \left(\frac{\partial U}{\partial T}\right)_B dT + \left(\frac{\partial U}{\partial B}\right)_T dB \tag{4.27}$$

We now equate equations (4.26), and (4.27) to yield the relations given in equation (4.28).

$$\left(\frac{\partial U}{\partial T}\right)_B = c(T, B) \tag{4.28a}$$

$$\left(\frac{\partial U}{\partial B}\right)_T = f + H \tag{4.28b}$$

Also, the second partial derivatives of U must equate, which is a relation given in equation (4.29).

$$\frac{\partial}{\partial B}\left(\left(\frac{\partial U}{\partial T}\right)_B\right)_T = \frac{\partial}{\partial T}\left(\left(\frac{\partial U}{\partial B}\right)_T\right)_B \tag{4.29}$$

Substituting the equations (4.28) into equation (4.29), will yield the relation between c and B as given in equation (4.30).

$$\frac{\partial}{\partial B}(c(T, B))_T = \frac{\partial}{\partial T}(f + H)_B \tag{4.30a}$$

$$\frac{\partial}{\partial B}(c(T, B))_T = \frac{\partial}{\partial T}(f)_B + \frac{\partial}{\partial T}(H)_B \tag{4.30b}$$

We now define entropy as given in equation (4.31).

$$dS = \frac{\delta Q}{T} = \frac{c(T,B)}{T}dT + \frac{f}{T}dB \tag{4.31}$$

Entropy is also a state variable with an exact differential, from which Maxwell's relations apply, as given in equation (4.32).

$$dS = \left(\frac{\partial S}{\partial T}\right)_B dT + \left(\frac{\partial S}{\partial B}\right)_T dB \tag{4.32}$$

Setting equations (4.31) and (4.32) equal to each other, will yield the expression given in equation (4.33).

$$\left(\frac{\partial S}{\partial T}\right)_B = \frac{c(T,B)}{T} \tag{4.33a}$$

$$\left(\frac{\partial S}{\partial B}\right)_T = \frac{f}{T} \tag{4.33b}$$

The second partial derivative terms of S must equate, which is a relation given in equation (4.34).

$$\frac{\partial}{\partial B}\left(\left(\frac{\partial S}{\partial T}\right)_B\right)_T = \frac{\partial}{\partial T}\left(\left(\frac{\partial S}{\partial B}\right)_T\right)_B \tag{4.34}$$

Substituting equation (4.33) into equation (4.34) will yield the result given in equation (4.35).

$$\frac{\partial}{\partial B}\left(\frac{c(T,B)}{T}\right)_T = \frac{\partial}{\partial T}\left(\frac{f}{T}\right)_B \tag{4.35}$$

Applying the chain rule to simplify equation (4.35) will yield the relations given in equation (4.36).

$$\frac{1}{T}\frac{\partial}{\partial T}(c(T,B))_T = f\frac{\partial}{\partial T}\left(T^{-1}\right)_B + T^{-1}\frac{\partial}{\partial T}(f)_B \tag{4.36a}$$

$$\frac{1}{T}\frac{\partial}{\partial T}(c(T,B))_T = \frac{-f}{T^2} + \frac{1}{T}\frac{\partial}{\partial T}(f)_B \tag{4.36b}$$

Multiply both sides of equation (4.36) by T to yield equation (4.37).

$$\frac{\partial}{\partial T}(c(T,B))_T = \frac{-f}{T} + \frac{\partial}{\partial T}(f)_B \tag{4.37}$$

Combining equations (4.30) and (4.37) will yield a relation for f as given in equation (4.38).

$$\frac{\partial}{\partial T}(f)_B + \frac{\partial}{\partial T}(H)_B = \frac{-f}{T} + \frac{\partial}{\partial T}(f)_B \tag{4.38a}$$

$$f = -T\frac{\partial}{\partial T}(H)_B \tag{4.38b}$$

Back substitute equation (4.38) into either equation (4.30) or (4.37) to get the form of $c(T,B)$. If we choose to substitute into equation (4.37), then $c(T,B)$ will take the form given in equation (4.39).

$$\frac{\partial}{\partial T}(c(T,B))_T = \frac{-1}{T}\left(-T\frac{\partial}{\partial T}(H)_B\right) + \frac{\partial}{\partial T}\left(-T\frac{\partial}{\partial T}(H)_B\right)_B \tag{4.39a}$$

$$\frac{\partial}{\partial T}(c(T,B))_T = \frac{\partial}{\partial T}(H)_B + \left\{-T\frac{\partial}{\partial T}\left(\frac{\partial}{\partial T}(H)_B\right)_B + \frac{\partial}{\partial T}(H)_B \cdot \frac{\partial}{\partial T}(-T)\right\} \tag{4.39b}$$

$$\frac{\partial}{\partial T}(c(T,B))_T = \frac{\partial}{\partial T}(H)_B - T\frac{\partial^2}{\partial T^2}(H)_B - \frac{\partial}{\partial T}(H)_B \tag{4.39c}$$

$$\frac{\partial}{\partial T}(c(T,B))_T = -T\frac{\partial^2}{\partial T^2}(H)_B \tag{4.39d}$$

Integrating both sides of equation (4.39) with respect to B will yield equation (4.40).

$$\int_0^B \frac{\partial}{\partial T}(c(T,B))_T dB' = \int -T\frac{\partial^2}{\partial T^2}(H)_B dB \tag{4.40}$$

Assuming a linear relation for relative permeability, as given in equation (4.41), then equations (4.26), (4.31), and (4.40) will yield the relations given in equations (4.42)-(4.44).

$$H\left(T,B\right) = \frac{1}{\mu\left(T\right)}B \tag{4.41}$$

$$U\left(T,B\right)=U\left(T,0\right)+\frac{1}{2}B^2\left(\frac{1}{\mu}-T\frac{\partial\frac{1}{\mu}}{\partial T}\right) \tag{4.42}$$

$$S\left(T,B\right)=S\left(T,0\right)-\frac{1}{2}B^2\frac{\partial\frac{1}{\mu}}{\partial T} \tag{4.43}$$

$$c\left(T,B\right)=c\left(T,0\right)-\frac{1}{2}B^2T\frac{\partial^2\frac{1}{\mu}}{\partial T^2} \tag{4.44}$$

Where the heat capacity for zero induction is given in equation (4.45).

$$c\left(T,0\right)=\frac{\partial U\left(T,0\right)}{\partial T}=T\frac{\partial S\left(T,0\right)}{\partial T} \tag{4.45}$$

Equation (4.24) may then also be evaluated as given in equation (4.46).

$$dQ=c\left(T,B\right)dT-T\left[\frac{\partial\frac{1}{\mu}}{\partial T}\right]_B BdB \tag{4.46}$$

If $dT=0$, then equation (4.46) yields the amount of heat given to the system due to dB, *i.e.* the magnetocaloric effect. We now redo the analysis with T, and H as the independent variables, such that $B(T,H)=\mu(T)H$, to produce a similar set of equations, given as equations (4.47)-(4.49).

$$U\left(T,H\right)=U\left(T,0\right)+\frac{1}{2}H^2\left(\mu+T\frac{\partial\mu}{\partial T}\right) \tag{4.47}$$

$$c\left(T,H\right)=c\left(T,0\right)+\frac{1}{2}H^2T\frac{\partial^2\mu}{\partial T^2} \tag{4.48}$$

$$dQ=c\left(T,H\right)dT+T\frac{\partial\mu}{\partial T}HdH \tag{4.49}$$

For paramagnetic substances, *i.e.* $T>\theta$, the Curie-Weiss law is given as equation (4.50).

$$\mu=\mu_0+\frac{C}{T-\theta} \tag{4.50}$$

Equation (4.50) may be simplified if the permeability of free space is neglected, which yields the relations given in equations (4.51)-(4.52).

$$\frac{\partial \frac{1}{\mu}}{\partial T} = \frac{1}{C} \tag{4.51}$$

$$\frac{\partial^2 \frac{1}{\mu}}{\partial T^2} = 0 \tag{4.52}$$

Equations (4.51)-(4.52) may then be substituted into equations (4.48)-(4.49) to yield equations (4.53)-(4.54).

$$dQ = c(T,B)dT - \frac{T}{C}BdB = c(T,H)dT - \frac{CT}{(T-\theta)^2}HdH \tag{4.53}$$

$$c(T,B) = c(T,0) \tag{4.54a}$$

$$c(T,H) = c(T,0) + H^2 T \frac{C}{(T-\theta)^3} \tag{4.54b}$$

Considering an adiabatic process, *i.e.* $dQ = 0$, and equations (4.48)-(4.49), will yield the relation given in equation (4.55).

$$\left[c\left(T,0\right) + \frac{1}{2}H^2 T \frac{\partial^2 \mu}{\partial T^2}\right] dT + T\frac{\partial \mu}{\partial T} HdH = 0 \tag{4.55}$$

The relative permeability will be assumed to take the form given in equation (4.56).

$$\begin{cases} \mu = \mu_o + A(\theta - T)^n \\ \quad \frac{\partial \mu}{\partial T} = -A \\ \quad \frac{\partial^2 \mu}{\partial T^2} = 0 \end{cases} \tag{4.56}$$

Where A is a positive constant, n is an exponent (here taken as $n = 1$), and $T \leq \theta$. This form of μ allows equations (4.48), and (4.55) to simplify as given in equation (4.57).

$$c(T,H) = c(T,0) = c_o \tag{4.57a}$$

$$c(T,H)dT = ATHdH \tag{4.57b}$$

Where c_o is assumed to be a constant, such that equation (4.57) may be integrated, with the result expressed as equation (4.58).

$$c_o \log \frac{T}{T_o} = \frac{1}{2} A H^2 \tag{4.58}$$

Where T_o represents the temperature for which $H = 0$. Solving for T in equation (4.58) will yield equation (4.59).

$$T = T_o e^{\left(\frac{A}{2c_o} H^2\right)} \tag{4.59}$$

The absolute efficiency may now be defined as given in equation (4.60).

$$\eta_{abs} = \frac{W}{Q_1} = \frac{Q_1 - |Q_2|}{Q_1} = 1 - \frac{Q_2}{Q_1} \tag{4.60}$$

Where W is the work output per cycle, Q_1, and Q_2 represent the net heat input, and heat output respectively, per cycle. The value of heat Q may be computed using equation (4.49), such that an isothermal process will yield the result given in equation (4.61).

$$Q = \int\limits_{H}^{H'} dQ = T \frac{\partial \mu}{\partial T} \int\limits_{H}^{H'} H dH = \frac{1}{2} T \frac{\partial \mu}{\partial T} \left(H'^2 - H^2 \right) \tag{4.61}$$

Applying equation (4.56) to this result will simplify into equation (4.62).

$$Q = -\frac{1}{2} A T \left(H'^2 - H^2 \right) \tag{4.62}$$

This result may be applied to the condition of an adiabatic process, such that equation (4.58) may be further simplified into the result given in equation (4.63).

$$c_o \log \frac{T}{T_o} = \frac{1}{2} A H_1^2 = \frac{1}{2} A \left(H_1'^2 - H_2'^2 \right) \tag{4.63}$$

Such that $H_1^2 - H_1'^2 = -H_2'^2$, which simplifies equation (4.56) as given in equation (4.64).

$$Q_i = -\frac{1}{2} A T_i H'^2 \tag{4.64}$$

Where the subscript i takes on the value of 1 for the hot-state, and the value 2 for the cold-state. Applying equation (4.64) to equation (4.60) will yield the definition of Carnot efficiency, which is given as equation (4.65).

$$\eta_{Carnot} = 1 - \frac{T_2}{T_1} \tag{4.65}$$

For a Stirling cycle, the thermal energy terms due to changes in heat capacity are included, which is given in equation (4.66).

$$Q_1 = c(T, H)(T_1 - T_2) + \frac{1}{2} A T_1 H'^2 \tag{4.66a}$$

$$Q_2 = c(T, 0)(T_1 - T_2) + \frac{1}{2} A T_2 H'^2 \tag{4.66b}$$

Applying this result, with equations (4.57), and (4.60) will yield efficiency as given in equation (4.67).

$$\eta_{abs} = 1 - \frac{c_o(T_1 - T_2) + \frac{1}{2} A T_1 H'^2}{c_o(T_1 - T_2) + \frac{1}{2} A T_2 H'^2} \tag{4.67}$$

If c_o is assumed to be large, then equation (4.67) may be simplified to produce the result given in equation (4.68), which represents the efficiency of a TMG operating as a Stirling cycle.

$$\eta_{abs} = \frac{T_1 - T_2}{T_1 + \frac{2c_o}{AH'^2}(T_1 - T_2)} \tag{4.68}$$

CHAPTER 5

Size Effects on Efficiency

5.1 Introduction

In this chapter, we build on the efficiency equations developed in section 4.2 by accounting for size-effects in order to predict MTMG efficiency at the nano and atomic scales. Specifically, we focus on comparing the magnetization as a function of temperature between nickel nano and atomic structures and reported values of bulk nickel. Furthermore, the parameter of interest for this investigation is the Curie point, which is the temperature for which the magnetic energy of a ferromagnetic material is perfectly balanced by thermal energy (see section 4.2). Experiments measuring the Curie point of nickel have shown its reduction for nano-grained samples when compared to its bulk counterpart. For example, if the structure is reduced to nanoscale dimension, such as a Nickel nanowire with a 30 nm diameter, the Curie temperature is comparatively reduced by 51 K [CXG07] [FCF11] [SSC00]. In 2004, Sun *et.al.* reported nickel Curie temperatures much lower than its bulk value, *e.g.* values around 300 K, for structures with features less than 10 nm [SZL04]. The analysis of nickel nanostructure will use this result, *i.e.* $T_c \approx 300K$, for a comparison with bulk nickel.

This chapter will show how the trend of a decreasing transition temperature, *i.e.* with a corresponding decrease in size for the same material, affects calculations of thermomagnetic energy conversion efficiency. In particular, three existing models from literature will be combined to predict this change in efficiency, they are: (1) Hsu-Sandoval's model of MTMG thermodynamic efficiency [HSW11a], (2) Kittel's model of ferromagnetic transition [KS65] and (3) Sun's model of a suppressed Curie point [SZL04]. The resulting combined model is then applied to several atomic and nano films to predict a trend in efficiency as a function of decreasing size [SSC14]. Finally, the combined model may then also be used to predict the efficiency of a hypothetical composite-volume containing multiple and separated atomic scale films of similar or distinct thicknesses.

5.2 Background

5.2.1 Model 1 - Thermodynamic Efficiency

The first model considers the thermodynamic efficiency of a MTMG, shown in Figure 1.1 (a) [UCL07], which was reviewed in section 2.3.3 and defined in section 4.2. From this efficiency analysis, we note here that the relation for absolute efficiency is approximated as being proportional to the ratio of the change in magnetization to the change in temperature, *i.e.* of the working body over the span of one cycle, and for constant applied field, as shown in equation (5.1).

$$\eta_{abs} \propto \frac{\Delta M}{\Delta T} \tag{5.1}$$

We also note from section 4.2 that the Carnot engine efficiency may be summarized by the relation given in equation (5.2).

$$\eta_{rel} \propto \frac{\Delta M}{\Delta T}\frac{T_{hot}}{\Delta T} \tag{5.2}$$

These metrics will subsequently be used to compute both the absolute and relative efficiency values of atomic scale systems operating at different temperatures by comparing to the bulk case. Moreover, we may estimate $\Delta M/\Delta T$ by examining the slope of the curve describing the magnetic transition behavior of a ferromagnet as a function of temperature and zero applied field.

5.2.2 Model 2 - Ferromagnetic Transition

This atomic model describes the magnetic behavior of a ferromagnet as it transitions from a ferromagnetic state into a paramagnetic state with increasing temperature, which also remains general enough to apply to any ferromagnetic system. To this end, we apply an exactly solvable statistical mechanics model of a many-spin system introduced by Kittel in 1965 [KS65]. This model serves the purpose of analytically describing the observed phenomenon of the decrease in a system's magnetic order with increasing temperature. One of the main assumptions is that neighboring spins are equally coupled via a Heisenberg Hamiltonian exchange interaction energy. Furthermore, the geometric arrangement of the atomic system does not play a role in the model analysis since the spins are assumed to behave independent of each other. The magnetic order of the spin-system begins as perfect (*i.e.* normalized to unity by the total number of spins) at absolute-zero temperature and tends to complete disorder at the Curie transition point as shown in Figure 5.1(a). This model also requires a minimum of $N = 20,000$ spins (*i.e.* statistical data points) in order to predict a reasonable drop in magnetic ordering (*i.e.* about ten percent order at its Curie point) of a general magnetic spin-system. The derivation of this model can be found in the original paper and here we apply key results from that derivation to describe the ferromagnetic transition of various systems with differing Curie points. The governing equation that predicts the degree of order in the magnetic system is given in equation (5.3).

$$\langle \eta \rangle = 1 - \left(\frac{2}{NZ} \right) \sum\nolimits_p p G_p e^{-\lambda_p \beta} \tag{5.3}$$

Where η represents the magnetic order of the system, which is bounded between 0 and 1 as a dimensionless fraction of the complete magnetic saturation, N the number of spins, Z the partition function, p the number of reversed spins, G_p and λ_p represent the degeneracy and eigenvalue of the system at the p-th eigenstate, respectively, β the reciprocal of the thermodynamic temperature, *i.e.* $\beta = k_B T$, and the sum runs over p-values ranging between $0 \leq p \leq N/2$.

The definition of Curie temperature prescribes the condition of balance between thermal and magnetic energy and is given as equation (5.4).

$$k_B T_C = \frac{1}{2} N J \tag{5.4}$$

Where J represents the Heisenberg exchange interaction energy and k_B is Boltzmann's constant. We now also define a dimensionless parameter, α, as defined in equation (5.5), which represents the ratio of magnetic energy to thermal energy.

$$\alpha \equiv N\beta J = \frac{NJ}{k_B T} \tag{5.5}$$

We note from the condition of equation (5.4), that $\alpha = 2$ at the Curie point. The minimum number of spins must be $N \geq 20,000$ for the model to be valid, with increasing accuracy as $N \to \infty$. We apply this model to the specific case of bulk nickel to show the transition as a function of absolute temperature. We must choose an empirically measured value for the Curie point to apply this model. In this case, we choose to apply the Curie point for bulk nickel, see Table 5.1, as $T_c = 630K$ [CG71]. The resulting curve of order as a function of temperature, shown in Figure 5.1 (b), reveals the expected trend of a decrease in magnetic order as thermal energy increases; all the way to about 10% of full saturation at the chosen Curie point.

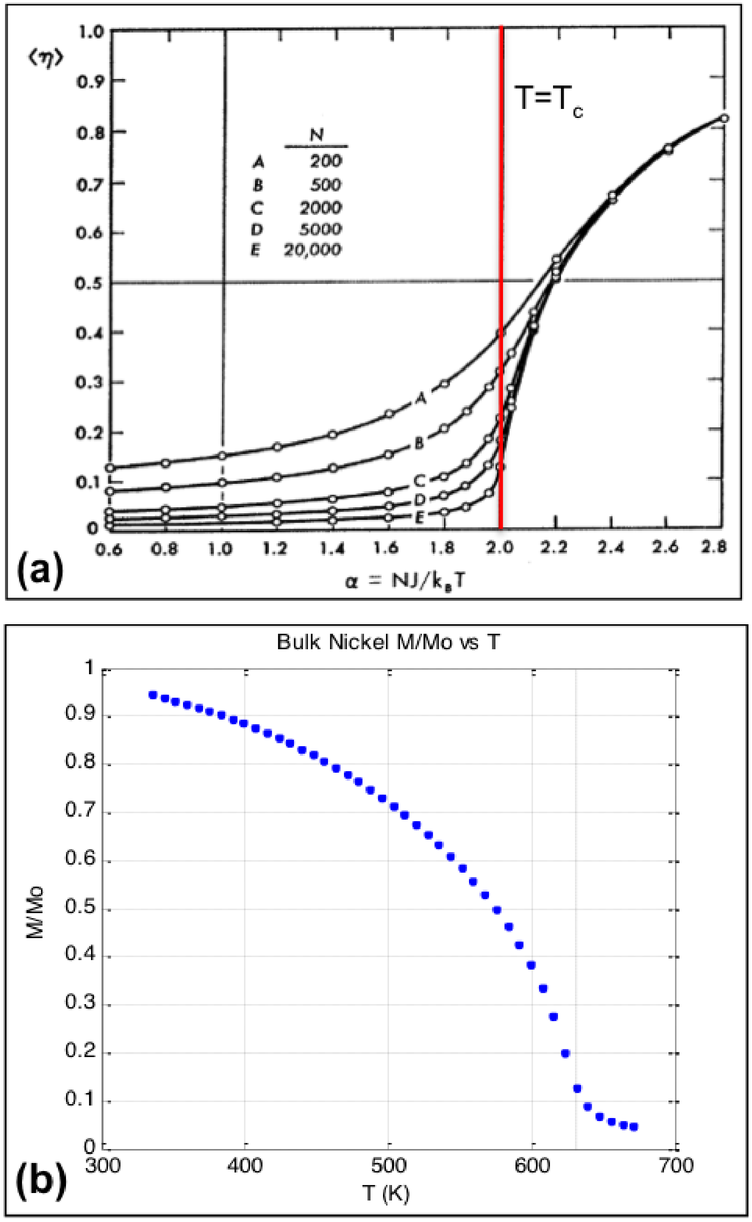

Figure 5.1: A statistical mechanics model of ferromagnetic transition for a many-spin system [KS65]; (a) dimensionless representation for both order and thermomagnetic energy balance, for various number of atomic spins (Image borrowed from Kittel [KS65]) and (b) semi-dimensional analysis of this model applied to $N = 20,000$ bulk nickel spins using values from Table 5.1, i.e. the equivalent of Curve E from (a).

Input	Value
Applied Field	$H_a = 3kOe$
Specific Heat	$\bar{c} = 32.5J/(mol \cdot K)$
Operating Temperatures	$T_{cold} = 625K$; $\Delta T = 5K$
Bulk Curie Temperature	$T_c = 630K$
Maximum Magnetization	$M_{max} = 76emu/cm^3$
Bulk Exchange-Energy[a]	8.698x10^{-18}erg
Atomic Diameter	$d_o = 0.248nm$

Table 5.1: Input parameters for bulk nickel as working body of a MTMG, taken from [HSW11a].

[a] Approximate exchange-energy for a sample of $N = 20,000$ spins from bulk state.

5.2.3 Model 3 - BOLS Correlation

The third, and last of the existing models, hypothesizes that the atomic coordination number, CN, or the number of nearest neighbor atoms, z plays a crucial role in determining the observed percent suppression when compared to the bulk case, which has a full CN, *i.e.* $z_b = 12$. In the case of imperfect CN, *i.e.* $z < 12$, the surface-to-volume ratio is close to unity and surface features will dominate the physics of the solid. The bond energy between neighboring atoms of an extended solid may become drastically different when compared to solids with CN imperfection. This phenomenon may be explained by the Bond-Order-Length-Strength (BOLS) correlation, first derived by Sun *et.al.* [SZL04] and applies to very flat, or very curved, geometries. For example, the Curie point tends to absolute-zero temperature for the case of an isolated atom, *i.e.* $z = 0$. A summary of definitions for this BOLS correlation is given as a set in equation (5.6).

$$\begin{cases} c_i = 2/\left\{1+\exp\left[\left(12-z_i\right)/\left(8z_i\right)\right]\right\} \\ E_i/E_b = c_i^{-1} \\ E_{coh,i}/E_{coh,b} = z_{ib}c_i^{-1} \end{cases} \tag{5.6}$$

In equation (5.6), c_i represents the *BOLS* correlation coefficient of the i-th atomic layer, E the cohesive energy per atomic bond, such that E_{coh} represents the overall atomic cohesion energy. The subscript i represents an index that counts layers starting from the outermost layer and ending at the center a given geometric arrangement, *i.e.* as in the space containing atoms with the same CN value per layer as z_i, which can either be multilayered or not. The extended solid has a subscript b for bulk, or does not have a subscript at all. The variable z_{ib} represents the ratio of CN imperfection in the i-th layer to the bulk CN, *i.e.* $z_{ib} = z_i/z_b$. We chose to define the geometry of any sized plate by its radial thickness, denoted as R and defined in equation (5.7), which takes into account the *BOLS* correlation for the first three atomic layers of a nanosolid only.

$$R = R_i = \left(K + \frac{1}{2} - \sum_{i\leq 3}\left(1-c_i\right)\right) d_o \tag{5.7}$$

This radial line commences at the center of an atom belonging to the central atomic layer of the plate, *i.e.* assuming infinite in-plane dimensions, and extends to the boundary surface-layer. The number of atoms lined along this radial line is defined as $K = R/d_o$ and refers to the size of the solid. This K parameter may then also represent the number of atomic film-layers starting from the outermost-layer and ending at the central layer, while the opposite side remains symmetric. These definitions of geometry allow the calculation of the surface-to-volume ratio, γ_i, by comparing the thickness of the i-th surface layer to the overall thickness R. The overall surface-to-volume ratio, γ_{sum} is the ratio of the sum of the $i \leq 3$ surface layer thicknesses to the overall thickness R. In Figure 5.2 the computed values of both γ and γ_{sum} are plotted against size K.

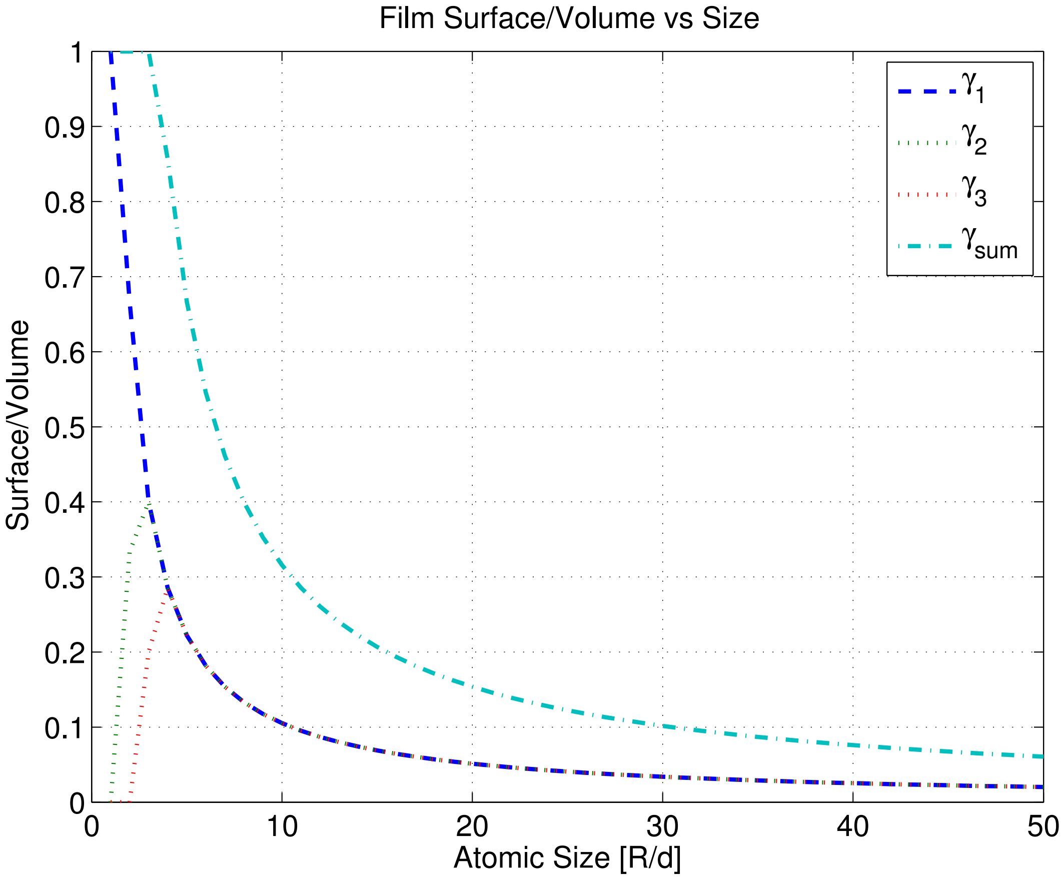

Figure 5.2: Surface-to-volume ratio, γ, of the first three individual layers and their sum, as a function of atomic plate thickness.

The relation given in equation 5.8 describes the T_c suppression of an atomic film, with thickness R, as a fraction of the empirical bulk T_c value, *i.e* when $R \to \infty$.

$$\frac{\Delta T_{C(R)}}{\Delta T_{C(\infty)}} = \frac{E_{coh,i}}{E_{coh(\infty)}} = \sum_{i \le 3} \gamma_i \left(z_{ib} c_i^{-1} - 1 \right) \tag{5.8}$$

The corresponding decrease in cohesive energy with decreasing thickness may be thought of as the reason why the Curie temperature decreases in the same proportion, as shown in equation (5.8). This is due to the general definition of the Curie point from equation (5.4), where the thermal vibration energy of the solid balances with the magnetic exchange energy of the spins. This method has been experimentally verified [HKM94] to accurately predict the Curie point suppression as a function of nickel plate size K, as shown in Figure 5.3 (a), which implies that this suppression appears mostly for atomic layers on the order of a monolayer. We follow an example calculation for the case of a nickel monolayer (ML), *i.e* $K = 1$, which may then be used to calculate other distinct K values; with the results shown in Table 5.2.

K	z	c	R [nm]	γ_{sum}	$T_c[K]$
1	4	0.876	0.248	1	240.2
2	6	0.938	0.496	1	272.3
3	12	1	0.744	1	356.9
4	12	1	0.992	0.875	435.2
5	12	1	1.240	0.667	478.7

Table 5.2: Analytical T_c value, for various nickel atomic plate K atomic thicknesses, z number of nearest neighbors, BOLS correlation parameter c, with corresponding radial thickness R and surface-to-volume ratio γ.

We present the the case of $K = 1$ as an example, which represents a ML of nickel spins with $z = z_1 = 4$ nearest neighbors since $i = 1$ only. This value is first applied to equation (5.6) to compute the BOLS correlation coefficient as $c = c_1 = 0.876$. We then apply this information to equation (5.7) and calculate the radial thickness as $R = R_1 = 0.248nm$, or the expected size of a nickel atom, given as d_o in Table 5.1. We note that $\gamma = 1$ since the single surface-layer also represents the entire volume. Finally, we apply equation(5.8) using the values tallied so far, to yield a $T_c = 240.2K$ prediction for the Curie point of a nickel ML. The computed values for this example make up the the first row of Table 5.2. The next case, *i.e* $K = 2$, makes use of the $K = 1$ values for its $i = 1$ layer and although the values for its $i = 2$ layer will change, they may be calculated in a similar fashion as in the example case. One caveat being the sum terms in

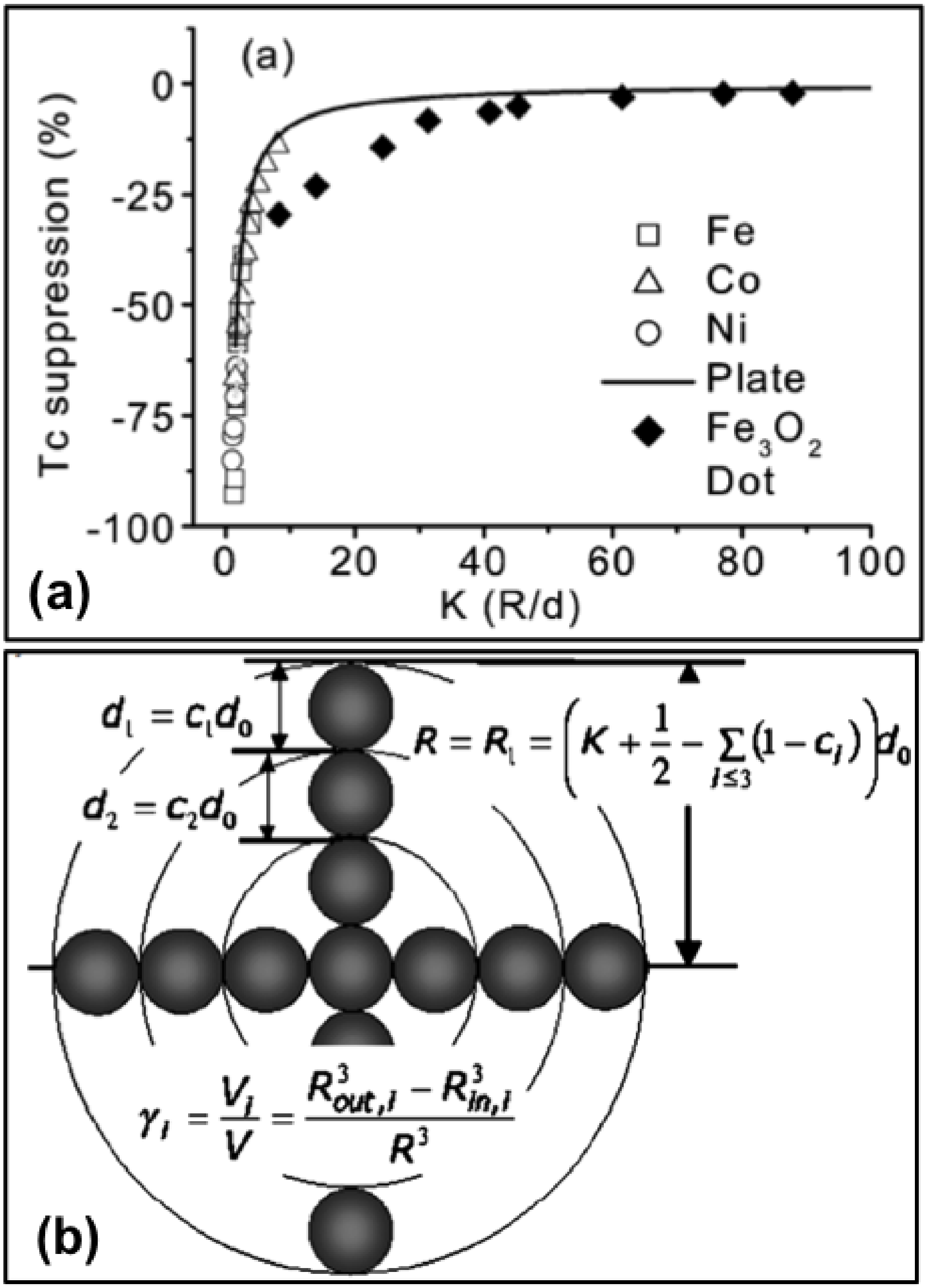

Figure 5.3: BOLS correlation applied to ferromagnetic nanosolids (Image borrowed from Sun *et. al.* (2004) [SZL04]); (a) a comparison to experimental values for a nickel plate [HKM94], (b) schematic layout for a $K = 4$ atomic arrangement showing expressions for parameters summarized later in Table 5.2.

equations (5.7)-(5.8), for which none were needed in the example case and another caveat being the calculation of γ. The illustration given in Figure 5.3(b) assumes a spherical geometry, hence the annotated definition of γ, though here we assume a film geometry, which for our case $\gamma = (R_{out,i} - R_{in,i})/R$, since each layer has the same in-plane dimensions. These calculations were carried out up to $K = 5$ in Table 5.2, where we observe that after the first three atomic layers, only the overall surface-to-volume ratio plays a role in Curie point suppression. In other words, any geometry other than these three cases will tend to asymptotically approach the bulk T_c as $K \rightarrow \infty$. In particular, we point out that of the five cases analyzed, the case $K = 2$ represents a geometry where the Curie temperature is closest to room-temperature at $T_{c(K=5)} = 272K$.

5.3 Combined Model

The previous three models will now be combined to form criteria for comparing the efficiency values of a nickel-based TMG, at various length scales. In section 5.2.3, we observed that the length scale required to appreciably change the bulk ferromagnetic Curie temperature of nickel is on the order of 10 nm. We used the BOLS correlation to predict the Curie temperature based solely on size, which yielded values as small as $T_c = 240K$ for a single nickel monolayer. We may then apply the ferromagnetic transition model to reflect the difference in magnetic behavior, *i.e* as a function of temperature starting from perfect order and complete saturation at absolute zero and ending at the Curie point, of this ML when compared to the conventional bulk state. Lastly, we adhere to equation (5.1)-(5.2) when comparing both the absolute and relative efficiency values of different systems. In particular, we evaluate the slope of the $M - T$ curve through the Curie point for each system.

We first apply the combined model's criteria to the bulk state of nickel by calculating the $\Delta M/\Delta T$ value from its corresponding $M - T$ curve (for $H = 0$), see Figure 5.1 (b). This value then serves as a basis for comparing other systems containing nickel with different atomic thicknesses. For bulk nickel acting as the working body of a MTMG, the parameters in Table 5.1 are used to compute relative efficiency as reported by Hsu-Sandoval [HSW11a] and reproduced here as the first row in Table 5.3. The subsequent values for relative efficiency in Table 5.3 represent those reported here by this combined model. All of these calculated values make use of the definitions found in Section 5.2 to establish the comparison among working bodies of dramatically different size and scale, along with their respective transition behaviors. Notice that the relative efficiency remains dependent on the absolute efficiency and thereby also proportional to the ratio of change in magnetization to the change in temperature of a given MTMG cycle, except that the operating temperatures are taken into account. This method may be considered conservative since an applied field would increase the magnetization of a ferromagnetic working body; nonetheless, if we keep the applied field and other parameters constant, then we can make a fair comparison for different nickel systems with unique transition slopes, like those shown in Figure 5.5 from section 5.4.

We start by computing the slope of the $M - T$ plot within range of the Curie point. In the case shown in Figure 5.1 (b), we apply a linear regression to compute the representative slope. We choose T_{hot} to be the Curie point and run a linear regression analysis to compute the slope for a $\Delta T = 5K$ temperature range. The resulting slope for the bulk scale, $\Delta M/\Delta T = 9.45 \times 10^{-3} emu/\left(cm^3 K\right)$, represents a key parameter for further comparison to systems of nickel with distinctly different geometries. For example, recall the ML case from section 5.2.3 having a $T_c = 240K$, we then apply Kittel's model to compute the ferromagnetic transition curve, thereby allowing the the slope to be calculated by linear regression fit, to arrive at a value of $\Delta M/\Delta T = 22.7 \times 10^{-3} emu/\left(cm^3 K\right)$. We compare this slope to that from bulk and observe a factor 2.4 difference. We further compute the relative efficiency by taking into account the operating temperatures as $\eta_{rel} = 3.1\%$. The efficiency values for other systems of nickel can be similarly calculated.

5.4 Results & Discussion

The uniquely combined model represents the collective features and assumptions of all three previous models. In section 5.3, we applied the combined model to the bulk case and established a $\Delta M/\Delta T = 9.45 \times 10^{-3} emu/\left(cm^3 K\right)$ value as a basis for comparison. We apply the combined models to various atomic plate geometries, *i.e.* up to $K = 5$, in order to produce the efficiency plots shown in Figure 5.4, which is also summarized in Table 5.3 for further comparison with the bulk case. From Figure 5.4 (a), we observe a trend of increasing slope as the size of the system decreases from bulk film to atomic ML. These results indicate that a decreasing size tends to increase the absolute efficiency, with the largest value is predicted for a nickel ML system with $\eta_{abs} = 0.0645\%$. Although this absolute efficiency for a ML is a factor of 2.4 larger than the bulk case, we may only compare relative efficiency values of the respective systems. As such, we compute the corresponding relative efficiency for five small-scale, *i.e.* for $1 < K < 5$. We note from Figure 5.4 (b) and Table 5.3, that all of the relative efficiency values being considered in this investigation are comparably equivalent. This unexpected result may be explained by recalling that the relative efficiency is proportional to the hot-side temperature as well as the slope. Here we take the hot-side temperature to be its corresponding Curie point. Thus, the relatively smaller hot-side temperature of the atomic case will outweigh the benefit of an increased absolute efficiency, *i.e.* a larger $\Delta M/\Delta T$ value.

The combined model may be further extended to analyze a multilayered system, *i.e.* a composite-volume, with the resulting analysis shown in Figure 5.5

Scale $[K]$	$\lvert\Delta M/\Delta T\rvert$ $[emu/cm^3 \cdot K]$	η_{abs} [%]	η_{rel} [%]
Bulk (K_∞)	0.0094	0.0269	3.38
Micro ($K > 5000$)	0.0094	0.0269	3.38
Nano ($K = 5$)	0.0124	0.0354	3.39
Atomic ($K = 4$)	0.0137	0.0391	3.40
Atomic ($K = 3$)	0.0164	0.0465	3.32
Atomic ($K = 2$)	0.0205	0.0583	3.18
Atomic ($K = 1$)	0.0227	0.0645	3.10

Table 5.3: Efficiency values for various nickel-based TMG on size K; the $|\Delta M/\Delta T|$ represents a measure of efficiency (see section 5.3: The first row corresponds to the method of Hsu-Sandoval *et. al.* [HSW11a] for the bulk nickel case (K_∞). The subsequent rows represent predictions of efficiency using the combined model for various K values, where $K > 5000$ represents the microscale

(b). A multilayered structure offers the possibility of scaling-up the size of this working body, while retaining the $M - T$ behavior. This raises the question of how this type of working body might theoretically behave if different size films are layered together as a composite structure, for example, a K_1 layer separated by a spacer and a K_2 layer. This example case is shown as a blue curve in Figure 5.5 (b). If the layering of different sized atomic films is possible, then the theoretical behavior of such a structure may then be predicted by this combined model. The reason behind this concept is to "tune" the Curie temperature, so that the operating temperatures may be designed, *e.g.* to broaden the operating temperature range. The efficiency analysis of this plot is similar to the case of a single layer, where we look at the slope of the curves near their transition point. We observe from the combined model that the magnetization of the layered structures tend to gradually reduce to near-zero with increasing temperature and thus have a smaller slope when compared to the single layer cases. This implies a tendency to decrease absolute efficiency for a multilayered system as compared to the stand-alone bulk case. Furthermore, the relative efficiency would tend to decrease with a decreasing hot-side temperature, *i.e.* just as in the case of the single layer analysis. Therefore, we conclude that the overall relative efficiency of a multilayered composite MTMG would decrease as compared to its bulk counterpart, such that a different application may be developed for the exotic features shown in Figure 5.5 (b); such as a thermal sensor, or as a thermal switch [BLJ09].

The drop in magnetization for a nickel atomic system near room-temperatures may be useful as a thermal sensor. For such an application, we would choose a multilayered nickel working body in order to design the operating temperature range. We forgo the sensor design here and comment that the plausibility of a multilayered structure itself should be established first before designing the sensor. On the other hand, the atomic-sized working body may still serve as an efficient generator if a large enough applied magnetic field in the cycle, just as in the bulk case [HSW11a] [Sol88].

We may reconsider the assumptions that yield equations (5.1) and (5.2), if a sufficiently large magnetic field, *i.e.* $H > 50kOe$, acts on the working body during the cold-side process. In this design, the contour integral in the numerator may not be approximated as $H_a \Delta M$ and the combined model may not be applied as given here. Such is also the case if remanent magnetization were to be included (see section 4.4) since this too breaks the proportionality assumption. Also, the combined model assumes the same material properties as in the bulk, which is an assumption that becomes weaker as the scale decreases. For example, the heat capacity of ultra thin nickel films decreases with decreasing size [LPR08]. This means that the input heat is smaller relative to its bulk value; thereby increasing the absolute efficiency by an amount not accounted for in the combined model. Such a discrepancies make this combined model even more conservative than what was already assumed. Therefore, the combined model represents a lower-bound estimate of efficiency for small both atomic and nano scaled versions of the original MTMG design.

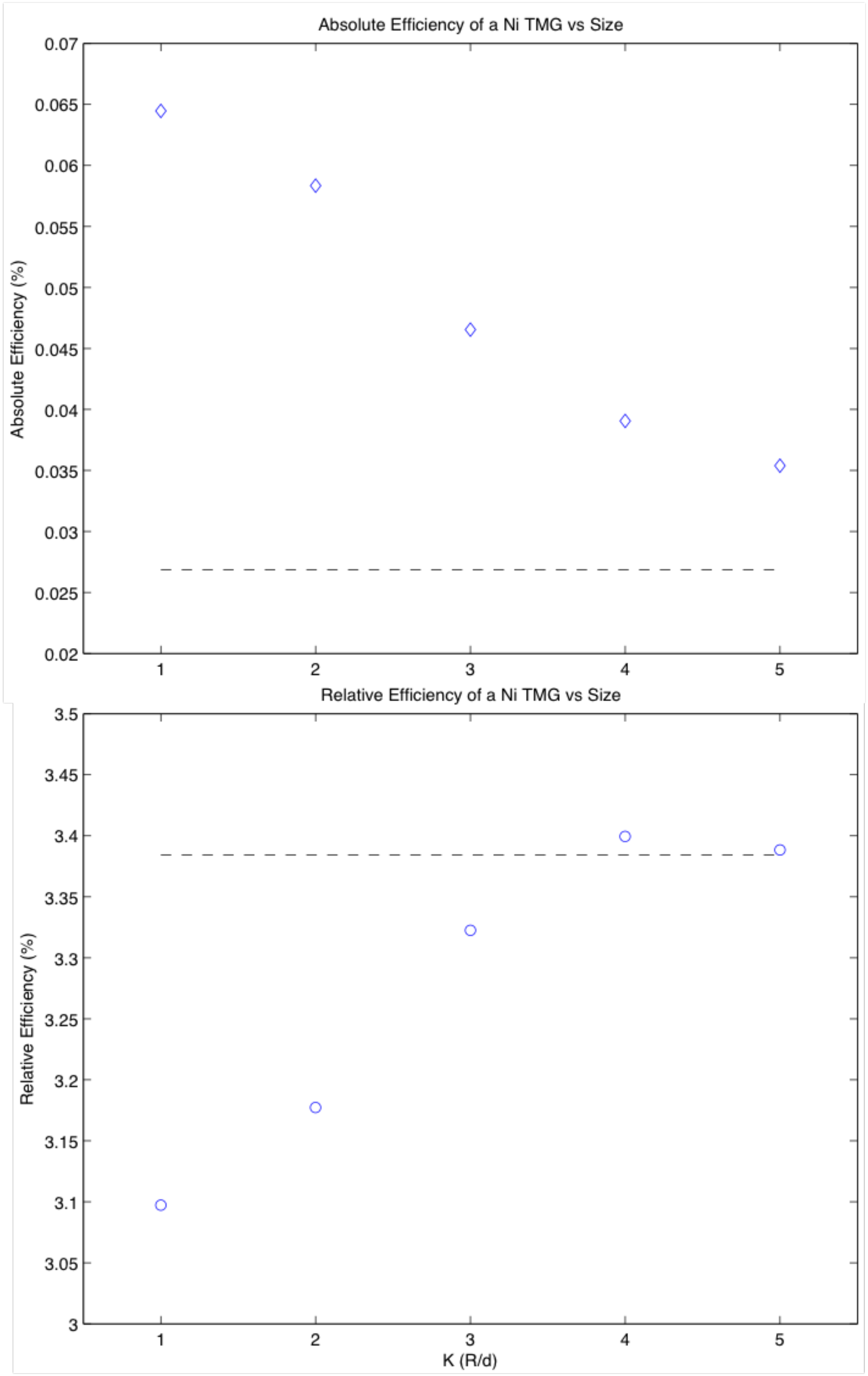

Figure 5.4: Calculation of efficiency for nickel atomic layers of size K and summarized in Table 5.3, where the bulk (dashed line) is provided for reference; (top) absolute efficiency, (bottom) relative efficiency.

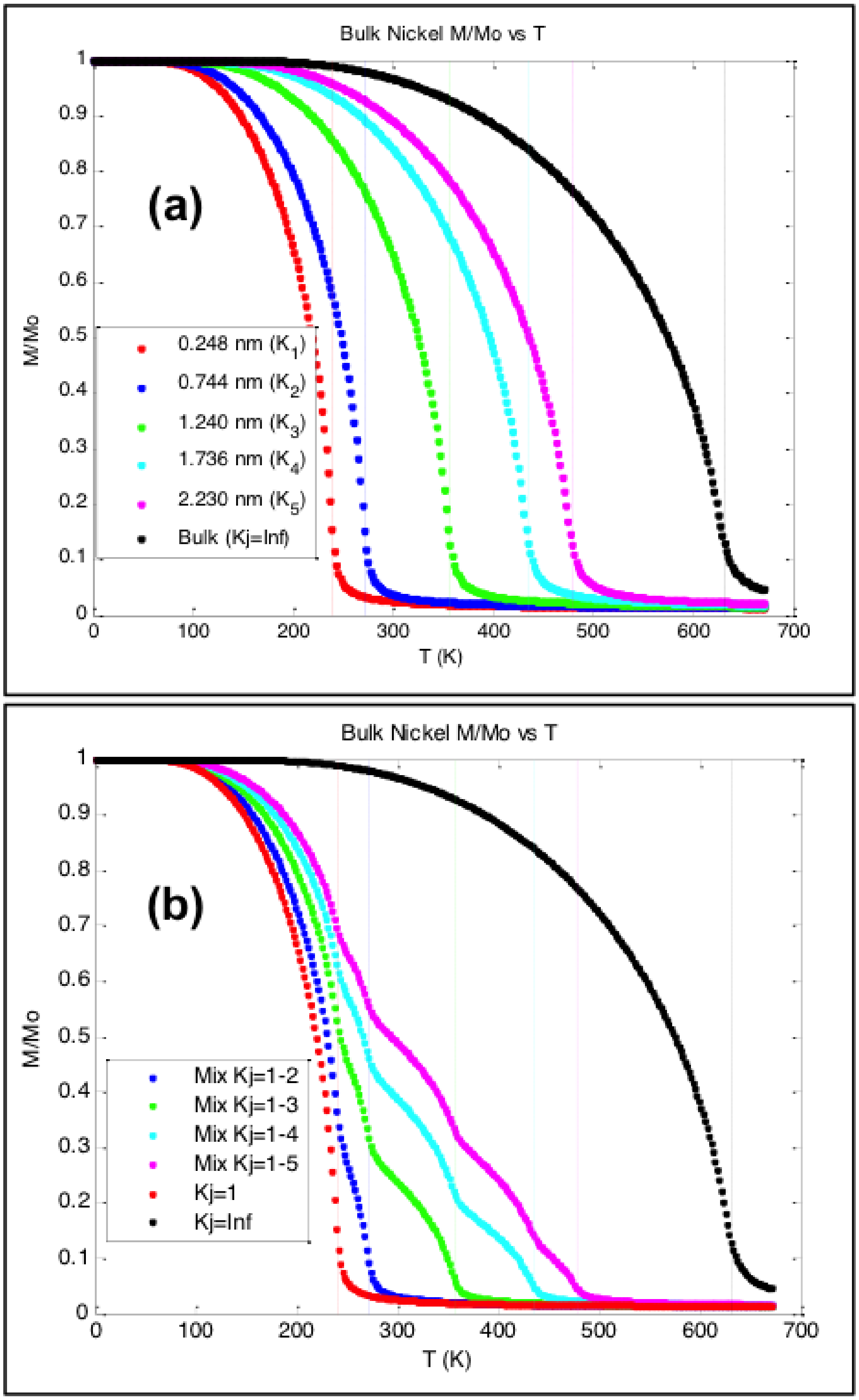

Figure 5.5: Combined model showing the ferromagnetic transition for various systems of nickel, with varying film thicknesses, according to their respective Curie point; (a) single-layer system, (b) multi-layered system.

5.5 Summary

The thermodynamic efficiency of an atomic scaled MTMG was analyzed by a method combining the following three existing models: (1) Hsu-Sandoval's model of MTMG efficiency, (2) Kittel's model of ferromagnetic transition and (3) Sun's model of Curie point suppression. The first model establishes the definitions of thermodynamic efficiency as they relate to a MTMG. The second model analytically describes the transition behavior of a ferromagnetic system. The third, and last, model establishes an experimentally verified relation between size and the Curie point of a ferromagnetic nanosolid. The resulting combined model, which also caries over all of the assumptions from the previous models, was then applied to various atomic film thicknesses of nickel in order to correlate thermodynamic efficiency relative to bulk scale.

This analysis revealed that efficiency begins to deviate from bulk material at around thicknesses of 10 *nm* or less and that operating temperatures drop to around room-temperature. At this length scale and smaller, the absolute efficiency tends to increase while the relative efficiency tends to remain around the bulk value. The combined models was also used to analyze a potential volume-averaged composite made of multiple, and distinct, atomic nickel layers. This composite might be better suited for application as a switch, or thermal sensor, rather than as an energy-harvester since the ferromagnetic transition behavior is predicted to be much broader as compared to the bulk transition. Nevertheless, this method for evaluating efficiency at atomic scales does not account for possible remanent magnetization, or for the possible decrease in heat capacity and as such, represents a lower-bound estimate. Therefore, the combined model analysis suggests that the thermodynamic efficiency of atomic scale films should be about the same as, though possibly greater than, what can be expected in the bulk case. This result may also allow room-temperature applications for a nickel-based MTMG.

CHAPTER 6

Other Considerations

6.1 Introduction

In this chapter, we explore the issue of structural defects in current methods for manufacturing nickel nanostructures. This structural imperfection is hypothesized to produce a gradual ferromagnetic transition. We explore ways to quantify this spread of the transition point, before considering a nanoMTMG design.

6.2 Transition Temperature Distribution

The MFT predicted magnetic behavior of spins seems to break-down near the transition temperature (see section 2.3.1). The "critical indices" model for magnetism near the Curie point predicts a drop-off in magnetic properties as exponential functions of temperature. This model, can be generalized to various other systems with a similar transition via a random process and requires experimental measurements to corroborate its predictions. Such a generalized and mathematical theory insufficiently accounts for the particular physics of interest involved in this investigation, which is the observation of a diffuse magnetic transition in an array of non-interacting SD nano-structures. The experimental observation of a diffuse transition for bulk ferromagnetic materials, as opposed to a sharp transition predicted by Weiss' MFT, may also apply at the atomic and nano scales; though for different reasons, as will be explored in this section. Thus, a modified MFT model is introduced that aims to account for the observed gradual ferromagnetic transition of nanostructures.

We begin with a volume-average model, which may be useful in describing the diffuse behavior of an array of SD nano structures spins near their transition temperature. In particular, a distribution function may be assumed to model the various Curie transition temperatures exhibited by a given material and this function itself may be a function of temperature. Experiments on bulk nickel show that two distinct transition temperatures exist [CG11], the so-called ferromagnetic and paramagnetic transition points, which negates the MFT prediction of a single transition temperature. Therefore, we begin this investigation by assuming two different Curie temperatures, *i.e.* θ_f, and θ_p associated with the ferromagnetic and paramagnetic phases, before extending this model to an array of SD structures.

To build the volume-averaged distribution function, we begin by assuming a unit volume of magnetic material. Next, we assume some unknown volume fraction, ν_f, of this material may be characterized by a known transition temperature, θ_f. This volume fraction remains unknown in the bulk state since it cannot be directly observed under the surface of the material, nor can it currently be measured directly; hence, its very existence currently remains a hypothesis. The rest of the material, $1 - \nu_f$, is assumed to be long-range magnetic "noise," and characterized by the larger transition temperature, θ_p. Thus, the volume-averaged Curie temperature may take the form shown in equation (6.1).

$$\bar{\theta} = \upsilon_f \theta_f + (1 - \upsilon_f)\,\theta_p \tag{6.1}$$

The physical interpretation of equation (6.1) may best be represented as a probability density function (PDF), namely a Gaussian distribution shown in equation (6.2), and plotted in Figure 6.1.

$$PDF = \frac{e^{\left(-\frac{(\theta-\bar{\theta})^2}{2\sigma^2}\right)}}{\sqrt{2\pi}\sigma} \tag{6.2}$$

In this equation, σ represents the variance, or shape of the curve and is related to the volume fraction, which represents the area under the curve. Therefore, the actual shape of this curve is unknown; and the shape shown in Figure 6.1, which implies a volume fraction of exactly half, may not represent reality. Since this averaged transition temperature depends on the unknown volume-fraction of ordered spins and that of spin-clusters, the usefulness of equation (6.2) appears limited. The hypothesis of this report is therefore dependent on the validity of equation (6.1), which seems to require experimental support that does not currently exist. Nevertheless, we may be able to extend this model to an array of non-interacting SD structures. First, we assuming that each structure in the array may only be characterized by either a θ_f or θ_p transition temperature. This assumption implies defective structures are present in the array; otherwise, they would all be characterized by the exact same transition temperature. Also, an array of SD structures will most likely be characterized by many more transition temperatures In reality, the number of distinct transition temperatures in the array will most likely be much larger than two and as many as the number of structures in the array. Moreover, the validity of this model, as applied to an array of SD structures, may be testable if ferromagnetic transition data from two distinctly designed nano-structures can be produced.

One experimental setup that may verify the modified MFT model appears to be a superposition of two distinct nano-structured geometries. Moreover, each of the two unique geometries must be individually tested, which represent two control experiments, for further comparison of their superposition. One nickel nanostructure, with its limited magnetic degrees of freedom (*i.e.* minimal locations for spins to cluster and form long-range order) is hypothesized to have a narrower Curie temperature distribution as compared to its bulk counterpart (*i.e.* less variance), as well as compared to an array of similar sized structures. From this viewpoint, the nanostructure itself represents a single cluster of short-range spins, as shown in the ideal case shown in Figure 6.1. This hypothetical case represents the best case-scenario and is not currently testable until magnetometers with a sufficiently

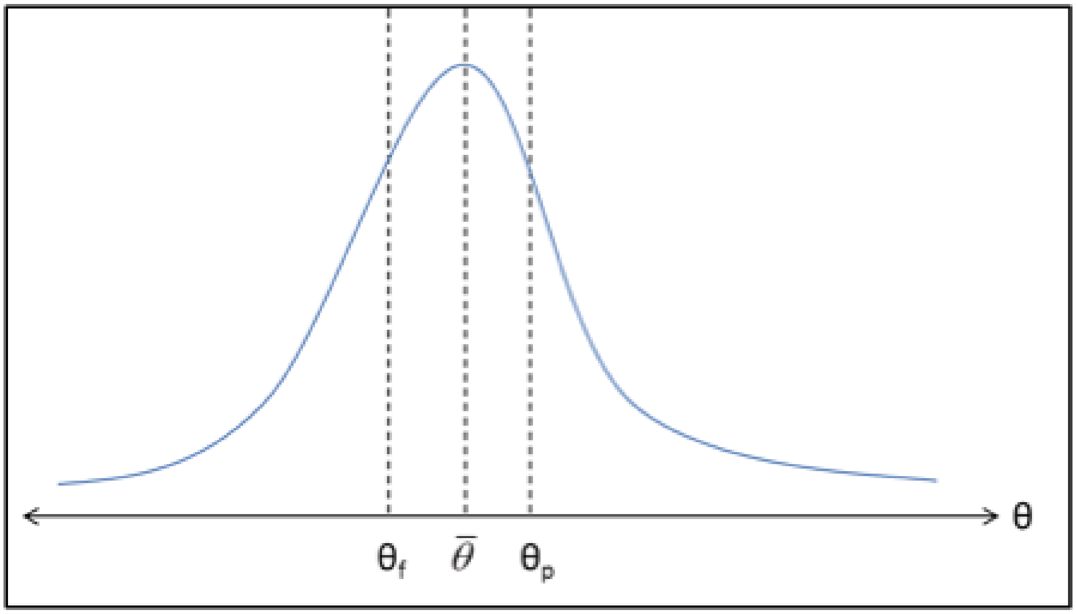

Figure 6.1: Schematic shape of Curie temperature distribution for bulk material (not to scale).

small resolution are developed. Instead, current techniques require a large number of non-interacting nano-structures (*i.e.* 10^7 for a magnetometer with a minimum resolution of about $10^{-}7$) in order to measure an average magnetic response.

Current manufacturing techniques do not produce a large array of SD structures without defect; and as such, variability in the distribution of spin sites will exist, which may cause a spread of transition temperatures, as shown by schematic comparison in Figure 6.2. This variability might therefore directly affect the systematic magnetic behavior near the transition point, *i.e.* a broadening of the Curie temperature distribution that draws parallels to magnetic "noise" observed in the bulk state. Although the case of magnetic ordering in the bulk state may be more complicated than is being considered here, the validity of the hypothesis could lend support to the volume-average model given in equation (6.1) for an array of atomic scale structures. Furthermore, a narrower distribution of transition points will favor thermomagnetic energy conversion applications due to a relatively larger $\Delta M/\Delta T$ (see section 5.3).

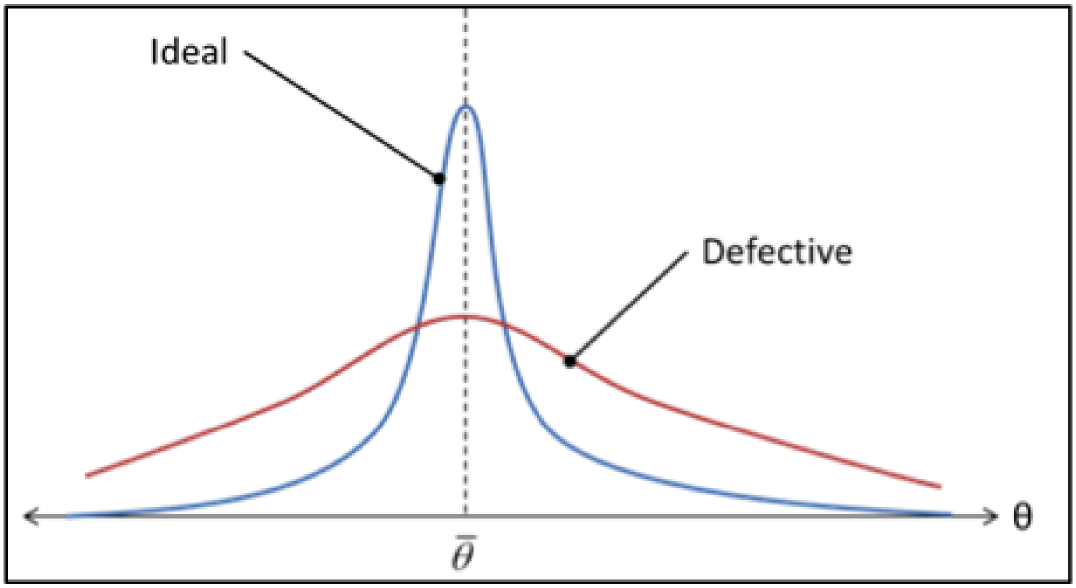

Figure 6.2: Schematic distribution of transition temperatures for ideal vs. defective nanostructures (not to scale).

The hypothesis of this investigation can be restated in a unique way; namely, that a narrow distribution of transition temperatures represents a favorable way to increase the thermomagnetic energy conversion potential of Nickel in nanostructured form. This investigation depends on the conformity of nanostructures resulting from currently available manufacturing processes. In both of these scenarios, defects are hypothesized to effectively broaden the distribution of transition temperatures, as shown in Figure 6.3. We consider both a high and a low conformity of manufactured nano-structures, as well as their hypothesized effect on magnetic transition. The defects in highly conforming structures is hypothesized to exhibit a distribution in transition temperatures like that shown in Figure 6.3 (a) since the majority of individual structures most likely behave in much the same way as the average structure. On the other hand, a low conforming array is hypothesized to broaden the distribution of transition temperatures, as shown in Figure 6.3 (b), since the average structure may only be representative of a minority of individual structures. In either case, surface-effects dominate the physical behavior of each nano-structure.

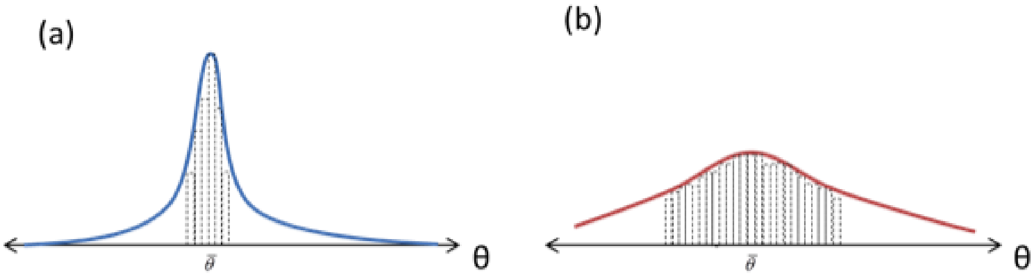

Figure 6.3: Schematic transition temperature distribution for highly conforming nanostructures (a) and for low conforming nanostructures (b).

If we consider the geometric variability of a random surface defect and its corresponding cohesive energy, on a nano-structure, then we may interpret the gradual ferromagnetic transition as a volume-averaged phenomenon. This seems to be analogous to the magnetic transition of a multilayered composite from section 5.3, Figure 5.5(b); however, a distinction being that in this case the competing volumes, *i.e.* between the defective region and the designed region, are hypothesized to interact within the same structure, *i.e.* no spacer between regions. Moreover, if this is the case, then the distribution of transition temperatures might then be exacerbated by an aggregate of individually "smeared" nano-structures. In such a scenario, the distribution of transition temperatures for an array of SD structures is hypothesized to tend towards the volume-dominant region, as illustrated in Figure 6.4. In one extreme, the defective area is negligible in comparison to the overall volume and in the other extreme, the defective area dominates the transition behavior. Any case in between would most likely be considered as a low-conforming array of nano-structures. Such distributions are only hypothesized, such that the effects of defects may only currently be qualitatively considered; though the ferromagnetic transition seems to be gradual in any of these cases. The usefulness of this analysis will remain limited unless manufacturing techniques reach tolerances that are on the order of an atomic diameter and unless magnetometers resolve magnetic moments of atomic clusters.

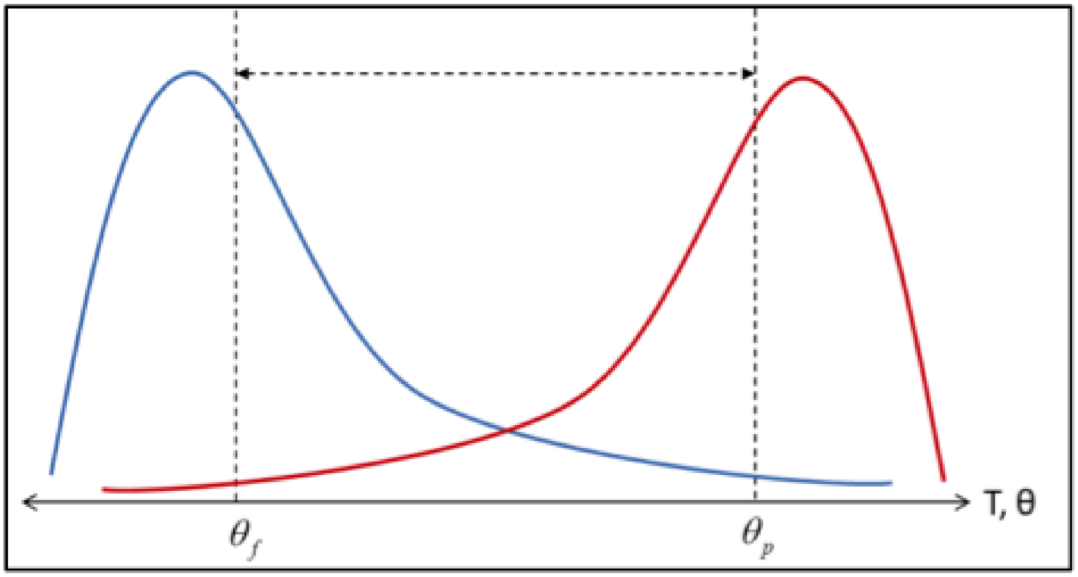

Figure 6.4: Hypothetical extreme cases showing possible behavior of transition temperature distribution; $T \approx \theta_f$ (blue), $T \approx \theta_p$ (red).

6.3 Design of a NanoMTMG

We consider the MEMS design shown in Figure 6.5 as a proof-of-concept for a nanoMTMG. In this design, a ferroelectric membrane, which is sitting on top of a silicon substrate, surrounds a dimple where the magnetic working body can translate in the vertical direction. This system should be impedance mismatched if we assume intermittent operation, such as in local plasmonic heating for thermally-assited magnetic recording devices [CPI09] [KGM08] [RBB06] [SC10]. These devices are expected to be prevalent in the future due to the increasing demand for data storage. We model a plasmonic pulse that applies a large heat flux to a local area of $50 \times 50 nm$, for 20 ns, in order to increase the temperature of a highly coercive bit, *e.g.* FePt, to a temperature above its Curie temperature, *i.e.* around 650 K for FePt. This blast wouldn't occur regularly, and only when a bit needs to be rewritten. Therefore, we design the nanoMTMG to harvest a maximum amount of energy per exposure to a plasmonic heat blast. In other words, a larger magnetic force compared to the spring force, such that when the plasmonic blast effectively turns off the hard ferromagnetic bit material, the nanoMTMG can allow a piezo membrane to be released and find equilibrium at its natural frequency. Such energy production may then be stored by a local capacitor for storage when its needed. This capacitor, as well as the whole nanoMTMG system, would have to be sealed off from its environment inside a vacuum to avoid unwanted side-effects from the excess heat. A lubricant is used at the tip of the transducer and recording bit medium in order to control the amount of heat being transmitted to the bit material, and may be tuned for the proof-of-concept in order to understand any further design complications.

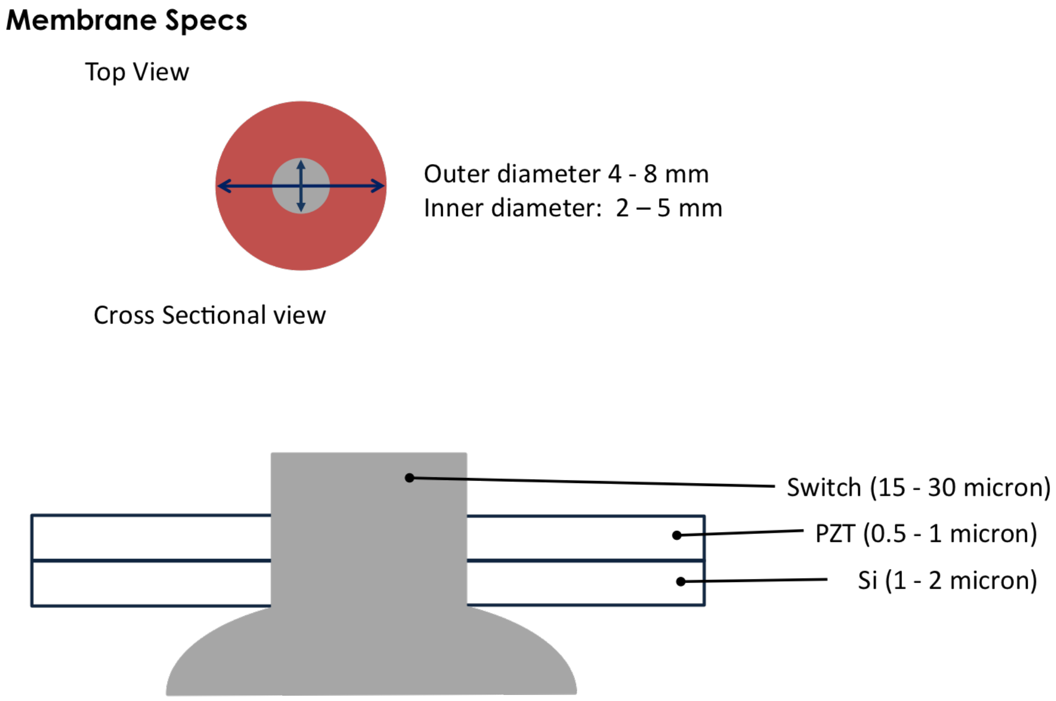

Figure 6.5: Micro-scale design to prove the concept of a nanoMTMG.

6.4 Summary

The characterization of nanoscale ferromagnetic transition behavior represents a current engineering challenge, which is partially due to the following facts: (1) current manufacturing techniques produce defects, and (2) current commercially available magnetometers cannot resolve the small magnetic moments of individual nanosolids. First, defects resulting from current manufacturing techniques seem to be unavoidable, and as such, any magnetic characterization of an array made up of identically designed structures will yield average measurements that may likely not be representative of the intended individual design. The magnetic characterization of one nano structure is not currently possible due to the second issue, which demands that many identical structures have to be fabricated in order to produce a large enough signal for modern day magnetometers to resolve. Thus, a statistical analysis of an array, or set of arrays, of single-domain structures is introduced with the intent of resolving an issue that is relevant to MTMG design; mainly, that a distribution of transition temperatures may possibly exist to undermine thermodynamic efficiency. These issues would need to be resolved before considering a nanoMTMG design, which may potentially be useful as an energy-harvester for a thermally-assisted magnetic recording device, *i.e.* as a secondary device for recycling energy. Nevertheless, a proof-of-concept for a nanoMTMG device is offered that makes use of MEMS fabrication techniques, and a thin film working body, for future design size scaling.

CHAPTER 7

Conclusion

A unique multiferroic thermomagnetic generator (MTMG) was investigated for possible performance improvements. Particular emphasis was placed on modeling MTMG thermodynamic efficiency due to the following reasons: (1) the efficiency of the original design by Ujihara *et.al.* had yet to be established, (2) we predict that nanoscale magnetic phenomena may increase efficiency and (3) atomic scale size effects on efficiency had yet to be considered. In this investigation, we established the thermodynamic relative efficiency of the original design as 0.5 % of Carnot using a model based on the method of Solomon. This efficiency model was then reanalyzed to include the remanent magnetization observed in nanoscale single-domains, which predicts an increase in efficiency to around 30% of Carnot. This model was then modified to include the effects of size at the atomic scale, which predicts that relative efficiency should be at least equivalent to, if not better than, bulk values. Here, we review details about this model at each stage of its development.

The original MTMG design by Ujihara *et.al.* was shown to be a type of thermomagnetic generator (TMG) since it can generate electricity by means of a magnetic material interactaction with a thermal gradient. The multiferroic component of this device represents a departure from conventional TMGs, *i.e.* which have no spring mechanism. As such, we developed a model of efficiency by modifying the method of Solomon for determining TMG thermodynamic efficiency to account for this mechanism. In our model, the energy associated with the spring mechanism was shown to cancel out due to the zero net displacement of the working body over a complete cycle. This model was then used to calculate the MTMG thermodynamic relative efficiency as 0.5% of Carnot. The original design reported a maximum power density of 3.6 mW/cm^2, which we used to estimate its thermodynamic relative efficiency as 0.2 % of Carnot. The agreement between these two calculations confirmed that we had established the thermodynamic efficiency of this unique MTMG. Furthermore, our model of MTMG thermodynamic efficiency allowed us to consider ways to improve upon these low efficiency values.

The thermodynamic efficiency of a MTMG was shown to depend on the following design constraints: (1) the type of material used as a working body, (2) the maximum applied field and (3) the remanent magnetization of the working body. First, the material response to an applied field at a given temperature will affect both the net work output, as well as the heat input requirement. As such, a survey of pure element materials were selected as working bodies in a MTMG for analysis and subsequent comparison. This survey confirmed Gd as the ideal working body for room temperature applications, which was shown to theoretically operate around 20% relative efficiency in single-crystal form. The second design constraint considers a large applied field, which results in efficiency values approaching their theoretical maximum of around 50%. However, we chose to limit the applied field to that generated by a permanent magnet since larger applied fields would require energy to be input into the system, *i.e.* in the form of powering a superconducting electromagnetic coil subsystem for example. Lastly, a material with remanent magnetization was shown to increase the available magnetic energy for producing work, thereby increasing the efficiency values to an order of magnitude of 30% relative to Carnot for a redesigned MTMG system. Moreover, a working body that can recover remanent magnetization, *i.e.* at zero applied field, after being cycled through its Curie point seems to only be possible at very small size scales.

Ferromagnetic structures that confine magnetization to an anisotropic direction have been observed for characteristic lengths at the nanoscale and smaller. Such nanostructures are predicted to retain this remanent magnetization, even after being thermally cycled about its Curie point and also in the absence of an applied field. This type of nanoscale working body could then take advantage of the extra magnetic energy, over a given MTMG cycle, to possibly outperform its bulk counterpart and thereby approach upper-bound efficiency values. However, defects resulting from current manufacturing techniques may not allow perfect nano structures to be fabricated, such that these ideas may not be verified, or discarded, until future fabrication and measurement technologies are made available. Thus, we next investigated MTMG thermodynamic efficiency at the nano and atomic scale.

A model was developed to correlate the effects of size on MTMG thermodynamic efficiency. This model combined three existing models to predict efficiency as a proportion of the bulk value. The results indicate that the relative efficiency of a nano scaled MTMG should operate at least as efficient as in the bulk scale, although closer to room-temperatures. This model was also shown to be a lower-bound estimate of efficiency since it did not take into account remanent magnetization, nor other material properties that would otherwise increase efficiency values. This result allows us to recommend the pursuit of realizing MTMG technology at smaller scales than what has already been achieved, *i.e.* at least at the nanoscale, with the prospect of efficiency values approaching their thermodynamic upper-bound. As such, a prototype MEMS design was offered to prove the concept of a nanoMTMG design; even though solutions to the engineering challenges posed by the prototype are presently unknown. Therefore, we conclude that more investigations are required in order to verify that nanoscale phenomena may allow TMG technology to approach the maximum efficiency allowed by thermodynamics.

References

[ACF13] C S Alves, F C Colman, G L Foleiss, G T F Vieira, and W Szpak. "Numerical simulation and design of a thermomagnetic motor." *Applied Thermal Engineering*, **61**:616–622, 2013.

[ACF14] C S Alves, F C Colman, G L Foleiss, W Szpak, T F Vieira, and A C Bento. "Simulation of solar Curie wheel using NiFe alloy and Gd." *International Journal of Refrigeration*, **37**:215–222, 2014.

[ACL06] David Avnir, Thibaud Coradin, Ovadia Lev, and Jacques Livage. "Recent bio-applications of sol–gel materials." *Journal of Materials Chemistry*, **16**:1013–1030, 2006.

[ACN72] N Angelescu, G Costache, and G Nenciu. "Molecular Field Theory and Phase Transitions in Partially Finite Spin Systems." *physica status solidi (b)*, **51**:205–214, 1972.

[AOG12] Y Apertet, H Ouerdane, C Goupil, and Ph Lecoeur. "Irreversibilities and efficiency at maximum power of heat engines: The illustrative case of a thermoelectric generator." *Physical Review E*, **85**:31116, 2012.

[AR10] R Amatya and R J Ram. "Solar thermoelectric generator for micropower applications." *Journal of electronic materials*, **39**:1735–1740, 2010.

[AS07] S R Anton and H A Sodano. "A review of power harvesting using piezoelectric materials (20032006)." *Smart Materials and Structures*, **16**:R1–R21, 2007.

[ASH08] Ashly Ainley, Jonathan Salfity, David Herman, Josh Hosking, Samuel M. Sandoval, and Gregory P. Carman. "Gadolinium thermal energy harvester." In *Engineering 87*, Henry Samueli School of Engineering and Applied Sciences, University of California at Los Angeles, 2008.

[Aut07] Anonymous Author. "Energy conversion in microsystems: is there a role for micro/nanofluidics?" *Lab on a Chip*, **7**(10):1234–1237, 2007.

[BB81] S M Benford and G V Brown. "T-S diagram for gadolinium near the Curie temperature." *Journal of Applied Physics*, **52**:2110–2112, 1981.

[BBR97] Mohamed El Hachemi Benbouzid, Rachid Beguenane, Gilbert Reyne, and Gerard Meunier. "Finite element modeling of Terfenol-D magneto-mechanical coupling: application to a direct micro-stepping rotary motor." In *Electric Machines and Drives Conference Record, 1997. IEEE International*, pp. WC2/6.1–WC2/6.3. IEEE, 1997.

[BCH13] M Buzzi, R V Chopdekar, J L Hockel, A Bur, T Wu, N Pilet, P Warnicke, G P Carman, L J Heyderman, and F Nolting. "Single domain spin manipulation by electric fields in strain coupled artificial multiferroic nanostructures." *Physical review letters*, **111**:27204, 2013.

[Bej88] Adrian Bejan. *Advanced engineering thermodynamics.* John Wiley & Sons, 1988.

[BI48] L Brillouin and H P Iskenderian. "Thermomagnetic generator." *Electrical Communication*, 1948.

[BJC09] Katherine E. Bulgrin, Y. Sungtaek Ju, Greg P. Carman, and Adrienne S. Lavine. "A Coupled Thermal and Mechanical Model of a Thermal Energy Harvesting Device." In *Volume 6: Emerging Technologies: Alternative Energy Systems; Energy Systems: Analysis, Thermodynamics and Sustainability*, pp. 327–335. ASME, January 2009.

[BLJ09] Katherine E Bulgrin, Adrienne S Lavine, and Y Sungtaek Ju. "Magnetomechanical thermal diode with tunable switching temperatures." In *Proceedings of PowerMEMS 2009*, 2009.

[Boz93] Richard M Bozorth. "Ferromagnetism." *Ferromagnetism, by Richard M. Bozorth, pp. 992. ISBN 0-7803-1032-2. Wiley-VCH, August 1993.*, **1**, 1993.

[BP79] W Bendick and W Pepperhoff. "Thermally excited states in cobalt and cobalt alloys." *Journal of Physics F: Metal Physics*, **9**:2185, 1979.

[Bro77] G V Brown. "Magnetic Stirling cycles - New applications for magnetic-materials." *Ieee Transactions on Magnetics*, **13**:1146–1148, 1977.

[BWH11] Alexandre Bur, Tao Wu, Joshua Hockel, Chin-Jui Hsu, Hyungsuk K D Kim, Tien-Kan Chung, Kin Wong, Kang L Wang, and Gregory P Carman. "Strain-induced magnetization change in patterned ferromagnetic nickel nanostructures." *Journal of Applied Physics*, **109**:123903, 2011.

[BYC05] Majid Bahrami, M Michael Yovanovich, and J Richard Culham. "Thermal contact resistance at low contact pressure: Effect of elastic deformation." *International Journal of Heat and Mass Transfer*, **48**:3284–3293, 2005.

[Car11] Sandro Carrara. "Introduction to nano-biosensing." In *Nano-Bio-Sensing*, pp. 1–21. Springer, 2011.

[CBK11] Yunus A Cengel, Michael A Boles, and Mehmet Kanoglu. *Thermodynamics: an engineering approach*, volume 5. McGraw-Hill New York, 2011.

[CBS09] Gilhwan Cha, Katie Bulgrin, Samuel M Sandoval, Gavin Chang, Carl Schulenberg, Sungtaek Ju, and Gregory P Carman. “Thermoelectric energy harvesting by thermal-magnetic switching of ferromagnetic material.” In *SPIE Smart Structures/NDE 2009*, San Diego, CA, 2009.

[CC78] Sōshin Chikazumi and Stanley H Charap. *Physics of magnetism.* RE Krieger Publishing Company Malabar, FL, 1978.

[CCB07] G P Carman, G Chang, and G Bush. “Modeling Multiferroic Materials.” *University of California Los Angeles Office Of Contracts And Grants Administration*, 2007.

[CCC14] Chin-Chung Chen, Tien-Kan Chung, Chi-Cheng Cheng, and Chia-Yuan Tseng. “A novel miniature thermomagnetic energy harvester.” In *SPIE Smart Structures and Materials+ Nondestructive Evaluation and Health Monitoring*, pp. 90570X–90570X–6. International Society for Optics and Photonics, 2014.

[CDD03] G Chen, M S Dresselhaus, G Dresselhaus, J P Fleurial, and T Caillat. “Recent developments in thermoelectric materials.” *International Materials Reviews*, **48**:45–66, 2003.

[CG71] J Crangle and G M Goodman. “The magnetization of pure iron and nickel.” *Proceedings of the Royal Society of London. A. Mathematical and Physical Sciences*, **321**:477–491, 1971.

[CG11] Bernard Dennis Cullity and Chad D Graham. *Introduction to magnetic materials.* Wiley-IEEE Press, 2011.

[CKC09] T K Chung, S Keller, and G P Carman. “Electric-field-induced reversible magnetic single-domain evolution in a magnetoelectric thin film.” *Applied Physics Letters*, **94**:132501, 2009.

[CMY69] M G Cooper, B B Mikic, and M M Yovanovich. “Thermal contact conductance.” *International Journal of heat and mass transfer*, **12**:279–300, 1969.

[Coq77] Bernard Coqblin. “Electronic Structure of Rare-Earth Metals and Alloys–the Magnetic Heavy Rare-Earths.” *Academic Press Inc., New York and London. 1977, 656 p*, 1977.

[CPI09] W A Challener, Chubing Peng, A V Itagi, D Karns, Wei Peng, Yingguo Peng, XiaoMin Yang, Xiaobin Zhu, N J Gokemeijer, and Y-T Hsia. “Heat-assisted magnetic recording by a near-field transducer with efficient optical energy transfer.” *Nature Photonics*, **3**:220–224, 2009.

[CST13] Tien-Kan Chung, Ujjwalu Shukla, Chia-Yuan Tseng, Chin-Chung Chen, and Chieh-Min Wang. "A magnetic/piezoelectric-based thermal energy harvester." In *SPIE Smart Structures and Materials+ Nondestructive Evaluation and Health Monitoring*, pp. 86880M–86880M–7. International Society for Optics and Photonics, 2013.

[CTC12] Tien-Kan Chung, Chia-Yuan Tseng, Chin-Chung Chen, and Chieh-Min Wang. "Design, fabrication, and testing of a thermal/mechanical/magnetic hybrid energy micro-harvester." In *ASME 2012 Conference on Smart Materials, Adaptive Structures and Intelligent Systems*, pp. 249–254. American Society of Mechanical Engineers, 2012.

[CXG07] L F Cao, D Xie, M X Guo, H S Park, and T Fujita. "Size and shape effects on Curie temperature of ferromagnetic nanoparticles." *Transactions of Nonferrous Metals Society of China*, **17**:1451–1455, 2007.

[CZ01] G Chen and T Zeng. "Nonequilibrium Phonon and Electron Transport in Heterostructures and Superlattices." *Microscale Thermophysical Engineering*, **5**:71–88, 2001.

[Dar67] M I Darby. "Tables of the Brillouin function and of the related function for the spontaneous magnetization." *British Journal of Applied Physics*, **18**:1415, 1967.

[DGI87] Gabriel J De Salvo, Robert W Gorman, and Mark C Imgrund. *ANSYS: Engineering Analysis System. User's Manual.* Swanson Analysis Systems, Incorporated, 1987.

[DSF06] Veronica Kane Dickson, Jocelyn A Silvester, Ian M Fearnley, Andrew G W Leslie, and John E Walker. "On the structure of the stator of the mitochondrial ATP synthase." *The EMBO journal*, **25**:2911–2918, 2006.

[DTP98] S. Yu. Dan'kov, A. M. Tishin, V. K. Pecharsky, and K. A. Gschneidner. "Magnetic phase transitions and the magnetothermal properties of gadolinium." *Phys. Rev. B*, **57**:3478–3490, Feb 1998.

[DWZ14] Licheng Deng, Zhiyu Wen, and Xingqiang Zhao. "Modeling and simulation of MEMS-based PZT beam array vibration energy harvester for high voltage output." *International Journal of Applied Electromagnetics and Mechanics*, 2014.

[DZB04] Manuel Diez, Boris Zimmermann, Michael Börsch, Marcelle König, Enno Schweinberger, Stefan Steigmiller, Rolf Reuter, Suren Felekyan, Volodymyr Kudryavtsev, and Claus A M Seidel. “Proton-powered subunit rotation in single membrane-bound F0F1-ATP synthase.” *Nature structural & molecular biology*, **11**:135–141, 2004.

[ELA10] N Espinosa, M Lazard, L Aixala, and H Scherrer. “Modeling a thermoelectric generator applied to diesel automotive heat recovery.” *Journal of Electronic materials*, **39**:1446–1455, 2010.

[Ell59] J F Elliott. “Thermomagnetic Generator.” *Journal of Applied Physics*, **30**:1774–1777, 1959.

[ELS54] J. F. Elliott, S. Legvold, and F. H. Spedding. “Some Magnetic Properties of Dy Metal.” *Phys. Rev.*, **94**:1143–1145, Jun 1954.

[ELS55] J. F. Elliott, S. Legvold, and F. H. Spedding. “Magnetic Properties of Erbium Metal.” *Phys. Rev.*, **100**:1595–1596, Dec 1955.

[FBS14] L D R Ferreira, C V X Bessa, I da Silva, and S Gama. “A heat transfer study aiming optimization of magnetic heat exchangers of thermomagnetic motors.” *International Journal of Refrigeration*, **37**:209–214, 2014.

[FCF11] Hans Fangohr, Dmitri S Chernyshenko, Matteo Franchin, Thomas Fischbacher, and Guido Meier. “Joule heating in nanowires.” *Physical Review B*, **84**:54437, 2011.

[FDF11] L Francioso, C De Pascali, I Farella, C Martucci, P Cretì, P Siciliano, and A Perrone. “Flexible thermoelectric generator for ambient assisted living wearable biometric sensors.” *Journal of Power Sources*, **196**:3239–3243, 2011.

[FFB07] Thomas Fischbacher, Matteo Franchin, Giuliano Bordignon, and Hans Fangohr. “A systematic approach to multiphysics extensions of finite-element-based micromagnetic simulations: Nmag.” *Magnetics, IEEE Transactions on*, **43**:2896–2898, 2007.

[FFP10] Jin Fang, Hugo Frederich, and Laurent Pilon. “Harvesting nanoscale thermal radiation using pyroelectric materials.” *Journal of Heat Transfer*, **132**:92701, 2010.

[FST11] Don B Fox, Daniel Sutter, and Jefferson W Tester. “The thermal spectrum of low-temperature energy use in the United States.” *Energy & Environmental Science*, **4**:3731–3740, 2011.

[FVT13] V Franzitta, Alessia Viola, and Marco Trapanese. “Design and Test of a Thermomagnetic Motor Using a Gadolinium Rotor.” *Applied Mechanics and Materials*, **432**:324–329, 2013.

[Gan06] Chen Gang. "Nanoscale heat transfer and nanostructured thermoelectrics." *IEEE Transactions on Components and Packaging Technologies*, **29**:238–246, 2006.

[GF88] Sergio Gama and Mário E. Fóglio. "Magnetization of erbium in the ordered and paramagnetic phases." *Phys. Rev. B*, **37**:2123–2132, Feb 1988.

[GLS61] R. W. Green, S. Legvold, and F. H. Spedding. "Magnetization and Electrical Resistivity of Erbium Single Crystals." *Phys. Rev.*, **122**:827–830, May 1961.

[Gor91] J M Gordon. "Generalized power versus efficiency characteristics of heat engines: The thermoelectric generator as an instructive illustration." *American Journal of Physics*, **59**:551, 1991.

[GSL09] Daniel Guyomar, Gael Sebald, Elie Lefeuvre, and Akram Khodayari. "Toward heat energy harvesting using pyroelectric material." *Journal of intelligent material systems and structures*, **20**:265–271, 2009.

[GSP09] Daniel Guyomar, Gaël Sebald, Sébastien Pruvost, Mickaël Lallart, Akram Khodayari, and Claude Richard. "Energy harvesting from ambient vibrations and heat." *Journal of Intelligent Material Systems and Structures*, **20**:609–624, 2009.

[GSS54] M Griffel, RE Skochdopole, and FH Spedding. "The heat capacity of gadolinium from 15 to 355 K." *Physical Review*, **93**:657–661, 1954.

[HBK13] Thomas E Hammel, Russell Bennett, Steve Keyser, Robert Sievers, William Otting, and Leo Gard. "Multi-Mission Radioisotope Thermoelectric Generator (MMRTG) Performance Data and Application to Life Modeling." In *11th International Energy Conversion Engineering Conference*, 2013.

[He12] Hong He. *"A Magnetomechanical Thermal Energy Harvester With A Reversible Liquid Interface."*. Master's thesis, University of California, Los Angeles, 2012.

[Hei28] Werner Heisenberg. "Zur theorie des ferromagnetismus." *Zeitschrift für Physik*, **49**:619–636, 1928.

[Her06] J P Heremans. "Thermoelectric and thermomagnetic transport in PbTe with nanoscale structures." In J Yang, T P Hogan, R Funahashi, and G S Nolas, editors, *Materials and Technologies for Direct Thermal-to-Electric Energy Conversion. Symposium*, pp. 149–160, Heremans, J.P. Dept. of Mech. Eng., Ohio State Univ., Columbus, OH, USA, 2006. Materials Research Society.

[HKM94] F Huang, M T Kief, G J Mankey, and R F Willis. "Magnetism in the few-monolayers limit: A surface magneto-optic Kerr-effect study of the magnetic behavior of ultrathin films of Co, Ni, and Co-Ni alloys on Cu(100) and Cu(111)." *Physical Review B*, **49**:3962–3971, 1994.

[HLB11] Scott R Hunter, Nickolay V Lavrik, Thirumalesh Bannuru, Salwa Mostafa, Slo Rajic, and Panos G Datskos. "Development of MEMS based pyroelectric thermal energy harvesters." In *SPIE Defense, Security, and Sensing*, pp. 80350V–80350V–12. International Society for Optics and Photonics, 2011.

[HLS63] D. E. Hegland, S. Legvold, and F. H. Spedding. "Magnetization and Electrical Resistivity of Terbium Single Crystals." *Phys. Rev.*, **131**:158–162, Jul 1963.

[HSW11a] Chin-Jui Hsu, S M Sandoval, K P Wetzlar, and G P Carman. "Thermomagnetic conversion efficiencies for ferromagnetic materials." *Journal of Applied Physics*, **110**:123923 (7 pp.), 2011.

[HSW11b] Chin-Jui Hsu, Samuel M Sandoval, Kyle P Wetzlar, and Gregory P Carman. "Energy conversion efficiency analysis using thermomagnetic properties of ferromagnetic materials." In *56th Annual Conference on Magnetism and Magnetic Materials (MMM)*, Scottdale, Arizona, 2011.

[HTS00] T C Harman, P J Taylor, D L Spears, and M P Walsh. "Thermoelectric quantum-dot superlattices with high ZT." *Journal of Electronic Materials*, **29**:L1–L2, 2000.

[HTW02] T C Harman, P J Taylor, M P Walsh, and B E LaForge. "Quantum dot superlattice thermoelectric materials and devices." *Science*, **297**:2229–2232, 2002.

[HWC13] Cheng-Ting Hsu, Cheng-Chou Won, Hsu-Shen Chu, and Jenn-Dong Hwang. "A case study of thermoelectric generator application on rotary cement furnace." In *Microsystems, Packaging, Assembly and Circuits Technology Conference (IMPACT), 2013 8th International*, pp. 78–81. IEEE, 2013.

[HWT05] T C Harman, M P Walsh, and G W Turner. "Nanostructured thermoelectric materials." *Journal of electronic materials*, **34**:L19–L22, 2005.

[Iof57] A F Ioffe. *Semiconductor thermoelements, and Thermoelectric cooling.* Infosearch, ltd., 1957.

[JCS85] K. D. Jayasuriya, S. J. Campbell, and A. M. Stewart. "Magnetic transitions in dysprosium: A specific-heat study." *Phys. Rev. B*, **31**:6032–6046, May 1985.

[JGG66] FJ Jelinek, BC Gerstein, M Griffel, RE Skochdopole, and FH Spedding. "Re-evaluation of some thermodynamic properties of gadolinium metal." *Physical Review*, **149**(2):489, 1966.

[JHF01] Weiping Jiang, Joe Hermolin, and Robert H Fillingame. "The preferred stoichiometry of c subunits in the rotary motor sector of Escherichia coli ATP synthase is 10." *Proceedings of the National Academy of Sciences*, **98**:4966–4971, 2001.

[Jil98] D Jiles. *Introduction to magnetism and magnetic materials.* CRC, 1998.

[JP13] Keyur B Joshi and Shashank Priya. "Multi-physics model of a thermo-magnetic energy harvester." *Smart Materials and Structures*, **22**:55005, 2013.

[JSC84] KD Jayasuriya, AM Stewart, SJ Campbell, and ESR Gopal. "The critical specific heat of terbium." *Journal of Physics F: Metal Physics*, **14**(7):1725, 1984.

[Ju05] Y Sungtaek Ju. "Phonon heat transport in silicon nanostructures." *Applied Physics Letters*, **87**:153106, 2005.

[Ju08] Y Sungtaek Ju. "Impact of interface resistance on pulsed thermoelectric cooling." *Journal of Heat Transfer*, **130**:14502, 2008.

[KGH67] Leo P Kadanoff, Wolfgang Götze, David Hamblen, Robert Hecht, E A S Lewis, V V_ Palciauskas, Martin Rayl, J Swift, David Aspnes, and Joseph Kane. "Static phenomena near critical points: theory and experiment." *Reviews of Modern Physics*, **39**:395, 1967.

[KGM08] Mark H Kryder, Edward C Gage, Terry W McDaniel, William A Challener, Robert E Rottmayer, Ganping Ju, Yiao-Tee Hsia, and M Fatih Erden. "Heat assisted magnetic recording." *Proceedings of the IEEE*, **96**:1810–1835, 2008.

[KK09] H R Khataee and A R Khataee. "Advances in F0F1-ATP synthase biological protein nanomotor: from mechanisms and strategies to potential applications." *Nano*, **4**:55–67, 2009.

[KM84a] L D Kirol and J I Mills. "Numerical-analysis of thermomagnetic generators." *Journal of Applied Physics*, **56**:824–828, 1984.

[KM84b] L D Kirol and J I Mills. "Thermomagnetic generator." *19th Intersociety Energy Conversion Engineering Conference (Cat. No. 84CH2101-4)—19th Intersociety Energy Conversion Engineering Conference (Cat. No. 84CH2101-4)*, pp. 1361–8 vol.3—4 vol. 2417 (+137 index), 1984.

[KM86] Charles Kittel and Paul McEuen. *Introduction to solid state physics*, volume 8. Wiley New York, 1986.

[KNP11] Razmig Kandilian, Ashcon Navid, and Laurent Pilon. "The pyroelectric energy harvesting capabilities of PMN–PT near the morphotropic phase boundary." *Smart Materials and Structures*, **20**:55020, 2011.

[KPS09] Akram Khodayari, Sebastien Pruvost, Gael Sebald, Daniel Guyomar, and Saber Mohammadi. "Nonlinear pyroelectric energy harvesting from relaxor single crystals." *Ultrasonics, Ferroelectrics and Frequency Control, IEEE Transactions on*, **56**:693–699, 2009.

[KS65] C Kittel and H Shore. "Development of a phase transition for a rigorously solvable many-body system." *Physical Review*, **138**:A1165–A1169, 1965.

[KTH11] M A Karri, E F Thacher, and B T Helenbrook. "Exhaust energy conversion by thermoelectric generator: two case studies." *Energy Conversion and Management*, **52**:1596–1611, 2011.

[KYN00] Kazuhiko Kinosita, Ryohei Yasuda, Hiroyuki Noji, and Kengo Adachi. "A rotary molecular motor that can work at near 100% efficiency." *Philosophical Transactions of the Royal Society of London. Series B: Biological Sciences*, **355**:473–489, 2000.

[LBF13] W Q Liu, Adrien Badel, Fabien Formosa, Y P Wu, and Amen Agbossou. "Wideband energy harvesting using a combination of an optimized synchronous electric charge extraction circuit and a bistable harvester." *Smart Materials and Structures*, **22**:125038, 2013.

[LCZ10] Peng Li, Lanlan Cai, Pengcheng Zhai, Xinfeng Tang, Qingjie Zhang, and M Niino. "Design of a concentration solar thermoelectric generator." *Journal of electronic materials*, **39**:1522–1530, 2010.

[Lee12] Felix Lee. *"Experimental and Analytical Studies on Pyroelectric Waste Heat Energy Conversion."*. Master's thesis, University of California, Los Angeles, 2012.

[LGM12] Felix Y Lee, Sam Goljahi, Ian M McKinley, Christopher S Lynch, and Laurent Pilon. "Pyroelectric waste heat energy harvesting using relaxor ferroelectric 8/65/35 PLZT and the Olsen cycle." *Smart Materials and Structures*, **21**:25021, 2012.

[LJL13] Felix Y Lee, Hwan Ryul Jo, Christopher S Lynch, and Laurent Pilon. "Pyroelectric energy conversion using PLZT ceramics and the ferroelectric–ergodic relaxor phase transition." *Smart Materials and Structures*, **22**:25038, 2013.

[LPH13] Devashish Lingam, Ankit R Parikh, Jiacheng Huang, Ankur Jain, and Majid Minary-Jolandan. "Nano/microscale pyroelectric energy harvesting: challenges and opportunities." *International Journal of Smart and Nano Materials*, pp. 1–17, 2013.

[LPR08] Aitor F. Lopeandía, F. Pi, and J. Rodríguez-Viejo. "Nanocalorimetric analysis of the ferromagnetic transition in ultrathin films of nickel." *Applied Physics Letters*, **92**(12):122503, 2008.

[LSL05] Tzy-Jiun M Luo, Ricky Soong, Esther Lan, Bruce Dunn, and Carlo Montemagno. "Photo-induced proton gradients and ATP biosynthesis produced by vesicles encapsulated in a silica matrix." *Nature materials*, **4**:220–224, 2005.

[Lut02] V S Lutsyak. "Theoretical analysis of thermoelectric figure of merit of longitudinal thermomagnetic generator and cooler." *Journal of Thermoelectricity*, pp. 9–17, 2002.

[LW11] Adolfo Lozano III and Michael E Webber. "Thermodynamic Analysis of a Novel Thermoelectric Generator in the Built Environment." In *9th Annual International Energy Conversion Engineering Conference*, 2011.

[Max81] James Clerk Maxwell. *A treatise on electricity and magnetism*, volume 1. Clarendon press, 1881.

[Mik74] B B Mikić. "Thermal contact conductance; theoretical considerations." *International Journal of Heat and Mass Transfer*, **17**:205–214, 1974.

[MP13] Ian M McKinley and Laurent Pilon. "Phase transitions and thermal expansion in pyroelectric energy conversion." *Appl. Phys. Lett*, **102**:23906, 2013.

[MS51] H P Myers and W Sucksmith. "The spontaneous magnetization of cobalt." *Proceedings of the Royal Society of London. Series A. Mathematical and Physical Sciences*, **207**:427–446, 1951.

[MXL11] Poorna Mane, Jingsi Xie, Kam K Leang, and Karla Mossi. "Cyclic energy harvesting from pyroelectric materials." *Ultrasonics, Ferroelectrics and Frequency Control, IEEE Transactions on*, **58**:10–17, 2011.

[MYM04] Fernando H Milanez, Michael M Yovanovich, and Marcia B H Mantelli. "Thermal contact conductance at low contact pressures." *Journal of Thermophysics and Heat Transfer*, **18**:37–44, 2004.

[NBA08] Robert K Nakamoto, Joanne A Baylis Scanlon, and Marwan K Al-Shawi. "The rotary mechanism of the ATP synthase." *Archives of biochemistry and biophysics*, **476**:43–50, 2008.

[NNP10] Hiep Nguyen, Ashcon Navid, and Laurent Pilon. "Pyroelectric energy converter using co-polymer P (VDF-TrFE) and Olsen cycle for waste heat energy harvesting." *Applied Thermal Engineering*, **30**:2127–2137, 2010.

[NVB10] Ashcon Navid, Damien Vanderpool, Abubakarr Bah, and Laurent Pilon. "Towards optimization of a pyroelectric energy converter for harvesting waste heat." *International Journal of Heat and Mass Transfer*, **53**:4060–4070, 2010.

[ODD07] A Ortiz, D Dalessandro, Q Dong, S Biswas, and D Longo. "Energy Harvester Power Management for Wireless Sensor Networks." In *American Society of Naval Engineers*, 2007.

[Oh99] Robert C O'handley. "Modern magnetic materials: principles and applications." *Modern Magnetic Materials: Principles and Applications, by Robert C. O'Handley, pp. 768. ISBN 0-471-15566-7. Wiley-VCH, November 1999.*, **1**, 1999.

[OW99] George Oster and Hongyun Wang. "ATP synthase: two motors, two fuels." *Structure*, **7**:R67–R72, 1999.

[OY01] T Ohoyama and N Yamada. "1.5. 4.6 Co and Ni alloys and compounds." In *Alloys and Compounds of d-Elements with Main Group Elements. Part 2*, pp. 54–55. Springer, 2001.

[Pet10] R B Peterson. "Size limits for regenerative heat engines." *http://dx.doi.org/10.1080/108939598200033*, 2010.

[PR99] Oliver Pänke and Bernd Rumberg. "Kinetic modeling of rotary CF_0F_1-ATP synthase: storage of elastic energy during energy transduction." *Biochimica et Biophysica Acta (BBA)-Bioenergetics*, **1412**:118–128, 1999.

[PS04] L K Pan and Chang Q Sun. "Coordination imperfection enhanced electron-phonon interaction." *Journal of applied physics*, **95**:3819–3821, 2004.

[PT14] Akshay Potnuru and Yonas Tadesse. "Characterization of Pyroelectric Materials for Energy Harvesting from Human Body." *Integrated Ferroelectrics*, **150**:23–50, 2014.

[RBB06] Robert E Rottmayer, Sharat Batra, Dorothea Buechel, William A Challener, Julius Hohlfeld, Yukiko Kubota, Lei Li, Bin Lu, Christophe Mihalcea, and Keith Mountfield. "Heat-assisted magnetic recording." *Magnetics, IEEE Transactions on*, **42**:2417–2421, 2006.

[RCW06] E K Reilly, E Carleton, and P K Wright. "Thin film piezoelectric energy scavenging systems for long term medical monitoring." *Wearable and Implantable Body Sensor Networks*, 2006.

[RHK11] S K T Ravindran, T Huesgen, M Kroener, and P Woias. "A self-sustaining micro thermomechanic-pyroelectric generator." *Applied Physics Letters*, **99**:104102, 2011.

[RLS58] B. L. Rhodes, S. Legvold, and F. H. Spedding. "Magnetic Properties of Holmium and Thulium Metals." *Phys. Rev.*, **109**:1547–1550, Mar 1958.

[Ros67] R. E. Rosensweig. "Theory of an improved thermomagnetic generator." *Proceedings of the Institution of Electrical Engineers-London*, **114**:405–&, 1967.

[SBS13] Yintao Song, Kanwal Preet Bhatti, Vijay Srivastava, C Leighton, and Richard D James. "Thermodynamics of energy conversion via first order phase transformation in low hysteresis magnetic materials." *Energy & Environmental Science*, **6**:1315–1327, 2013.

[SC89] AM Stewart and SJ Collocott. "The specific heat of samarium and holmium in the range 2-32 K." *Journal of Physics: Condensed Matter*, **1**(4):677, 1989.

[SC10] Dror Sarid and William Challener. *Modern introduction to surface plasmons: theory, Mathematica modeling, and applications.* Cambridge University Press, 2010.

[SC14] Samuel M Sandoval and Gregory P Carman. "Thermomagnetic energy conversion efficiency near the transition point for nickel atomic layers." In *58th Annual Conference on Magnetism and Magnetic Materials*, Denver, Colorado, 2014.

[SCJ06] S K Shrestha, G Conibeer, C W Jiang, and D Konig. "Possible Approaches to High Efficiency Thermoelectric Devices." In *Optoelectronic and Microelectronic Materials and Devices, 2006 Conference*, pp. 28–31, 2006.

[SGA09] Gael Sebald, Daniel Guyomar, and Amen Agbossou. "On thermoelectric and pyroelectric energy harvesting." *Smart Materials and Structures*, **18**:125006, 2009.

[SGS04] RE Skochdopole, Maurice Griffel, and FH Spedding. “Heat Capacity of Erbium from 15 to 320 ° K.” *The Journal of Chemical Physics*, **23**(12):2258–2263, 2004.

[SH99] R C Smith and C L Hom. “Domain wall theory for ferroelectric hysteresis.” *Journal of Intelligent Material Systems and Structures*, **10**:195–213, 1999.

[Sha74] L. W. Shacklette. “Specific heat and resistivity of iron near its Curie point.” *Phys. Rev. B*, **9**:3789–3792, May 1974.

[SHC10] Samuel M Sandoval, Chin-Jui Hsu, and Gregory P Carman. “An Efficiency Analysis of a Novel Thermal Energy Harvesting Device.” In *SPIE Smart Structures/NDE 2010*, San Diego, CA, 2010.

[SIP04] H A Sodano, D J Inman, and G Park. “A review of power harvesting from vibration using piezoelectric materials.” *Shock and Vibration Digest*, **36**:197–206, 2004.

[SLG08] Gael Sebald, Elie Lefeuvre, and Daniel Guyomar. “Pyroelectric energy conversion: optimization principles.” *Ultrasonics, Ferroelectrics and Frequency Control, IEEE Transactions on*, **55**:538–551, 2008.

[SLS62] D. L. Strandburg, S. Legvold, and F. H. Spedding. “Electrical and Magnetic Properties of Holmium Single Crystals.” *Phys. Rev.*, **127**:2046–2051, Sep 1962.

[SLW99] D Stock, A G W Leslie, and J E Walker. “Molecular architecture of the rotary motor in ATP synthase.” *Science*, **286**:1700, 1999.

[SM09] Khalid M Saqr and Mohd N Musa. “Optimization of Fin Geometry of An Exhaust Heat Exchanger For Automotive Thermoelectric Generators.” *International Journal of Applied Engineering Research*, **4**, 2009.

[SNW02] Alan E Senior, Sashi Nadanaciva, and Joachim Weber. “The molecular mechanism of ATP synthesis by F_1F_0-ATP synthase.” *Biochimica et Biophysica Acta (BBA)-Bioenergetics*, **1553**:188–211, 2002.

[SO95] T J Seebeck and A Oettingen. *Magnetische polarisation der metalle und erze durch temperatur-differenz.* W. Engelmann, 1895.

[Sol88] D Solomon. “Improving The Performance of a Thermomagnetic Generator by Cycling The Magnetic-field.” *Journal of Applied Physics*, **63**:915–921, 1988.

[Sol91] D Solomon. “Design of a thermomagnetic generator.” *Energy Conversion and Management*, **31**:157–173, 1991.

[SSC00] L Sun, P C Searson, and C L Chien. "Finite-size effects in nickel nanowire arrays." *Physical Review B*, **61**:R6463–R6466, 2000.

[SSC14] Samuel M Sandoval, Abdon Sepulveda, and Gregory P Carman. "On the thermomagnetic conversion efficiency of variously sized nickel films: From bulk to atomic scale." In writing, 2014.

[Sta59] H E Stauss. "Efficiency of thermomagnetic generator." *Journal of Applied Physics*, **30**:1622–1623, 1959.

[Sta87] H Eugene Stanley. "Introduction to phase transitions and critical phenomena." *Introduction to Phase Transitions and Critical Phenomena, by H Eugene Stanley, pp. 336. Foreword by H Eugene Stanley. Oxford University Press, Jul 1987. ISBN-10: 0195053168. ISBN-13: 9780195053166*, **1**, 1987.

[SZL04] Chang Q Sun, W H Zhong, S Li, B K Tay, H L Bai, and E Y Jiang. "Coordination imperfection suppressed phase stability of ferromagnetic, ferroelectric, and superconductive nanosolids." *The Journal of Physical Chemistry B*, **108**:1080–1084, 2004.

[Tel47] M Telkes. "The Efficiency of Thermoelectric Generators. I." *Journal of Applied Physics*, **18**:1116, 1947.

[Tes89] Nikola Tesla. "Thermo Magnetic Motor: US 396121 A.", January 1889.

[TLS58] W. C. Thoburn, S. Legvold, and F. H. Spedding. "Magnetic Properties of Terbium Metal." *Phys. Rev.*, **112**:56–58, Oct 1958.

[Tra10] Marco Trapanese. "DQ axis theory of thermomagnetic Curie motor." In *Electrical Machines (ICEM), 2010 XIX International Conference on*, pp. 1–4. IEEE, 2010.

[Tra11] Marco Trapanese. "A dq axis theory of the magnetic, thermal, and mechanical properties of Curie motor." *Journal of Applied Physics*, **109**:07E706, 2011.

[UCL07] M Ujihara, G P Carman, and D G Lee. "Thermal energy harvesting device using ferromagnetic materials." *Applied Physics Letters*, **91**:93508, 2007.

[VCV14] Gaurav Vats, Aditya Chauhan, and Rahul Vaish. "Thermal Energy Harvesting Using Bulk LeadFree Ferroelectric Ceramics." *International Journal of Applied Ceramic Technology*, 2014.

[VKG12a] D Vuarnoz, A Kitanovski, C Gonin, Y Borgeaud, M Delessert, M Meinen, and P W Egolf. “Quantitative feasibility study of magnetocaloric energy conversion utilizing industrial waste heat.” *Applied Energy*, **100**:229–237, 2012.

[VKG12b] D Vuarnoz, A Kitanovski, C Gonin, and P W Egolf. “Thermodynamic and exergy efficiencies of magnetocaloric energy conversion utilising industrial waste heat.” *International Journal of Exergy*, **10**:365–378, 2012.

[Vop12] Melvin M Vopson. “The multicaloric effect in multiferroic materials.” *Solid State Communications*, **152**:2067–2070, 2012.

[Vop13] Melvin M Vopson. “Theory of giant-caloric effects in multiferroic materials.” *Journal of Physics D: Applied Physics*, **46**:345304, 2013.

[VSC01] Rama Venkatasubramanian, Edward Siivola, Thomas Colpitts, and Brooks O’quinn. “Thin-film thermoelectric devices with high room-temperature figures of merit.” *Nature*, **413**:597–602, 2001.

[WBF13] Yipeng Wu, Adrien Badel, Fabien Formosa, Weiqun Liu, and Amen E Agbossou. “Piezoelectric vibration energy harvesting by optimized synchronous electric charge extraction.” *Journal of Intelligent Material Systems and Structures*, **24**:1445–1458, 2013.

[WBH11] Tao Wu, Alexandre Bur, Joshua L Hockel, Kin Wong, Tien-Kan Chung, and Gregory P Carman. “Electrical and mechanical manipulation of ferromagnetic properties in polycrystalline nickel thin film.” *Magnetics Letters, IEEE*, **2**:6000104, 2011.

[Wei07] Pierre Weiss. “L’hypothèse du champ moléculaire et la propriété ferromagnétique.” *J. Phys. Theor. Appl.*, **6**:661–690, 1907.

[WHC12] Chien-Chang Wang, Chen-I Hung, and Wei-Hsin Chen. “Design of heat sink for improving the performance of thermoelectric generator using two-stage optimization.” *Energy*, **39**:236–245, 2012.

[WO98] Hongyun Wang and George Oster. “Energy transduction in the F1 motor of ATP synthase.” *Nature*, **396**:279–282, 1998.

[Woh80] Erich P Wohlfarth. *Ferromagnetic materials: a handbook on the properties of magnetically ordered substances*, volume 2. Elsevier, 1980.

[WSX11] Hongyan Wang, Xiaobiao Shan, Tao Xie, and Muwen Fang. “Analyses of impedance matching for piezoelectric energy harvester with a resistive circuit.” In *Electronic and Mechanical Engineering and Information Technology (EMEIT), 2011 International Conference on*, volume 4, pp. 1679–1683. IEEE, 2011.

[Xie09] Jingsi Xie. *"Experimental and numerical investigation on pyroelectric energy scavenging."*. Master's thesis, Virginia Commonwealth University, 2009.

[XYL12] Jinsheng Xiao, Tianqi Yang, Peng Li, Pengcheng Zhai, and Qingjie Zhang. "Thermal design and management for performance optimization of solar thermoelectric generator." *Applied Energy*, **93**:33–38, 2012.

[YC04] R Yang and G Chen. "Recent developments in nanostructured thermoelectric materials and devices." In *Thermal and Thermomechanical Phenomena in Electronic Systems, 2004. ITHERM '04. The Ninth Intersociety Conference*, volume 2, 2004.

[YMH01] M Yoshida, E Muneyuki, and T Hisabori. "ATP synthase-a marvellous rotary engine of the cell." *Nature Reviews Molecular Cell Biology*, **2**:669–677, 2001.

[ZC01] T Zeng and G Chen. "Phonon heat conduction in thin films: impacts of thermal boundary resistance and internal heat generation." *Journal of Heat Transfer*, **123**:340, 2001.